NORTHWESTERN UNIVERSITY

Science-Based Design of High-Performance Bubblegum

A DISSERTATION

SUBMITTED TO THE GRADUATE SCHOOL

IN PARTIAL FULFILLMENT OF THE REQUIREMENTS

for the degree

DOCTOR OF PHILOSOPHY

Field of Materials Science & Engineering

By

Leslie D. Morgret

EVANSTON, ILLINOIS

December 2008

ABSTRACT

Science-Based Design of High-Performance Bubblegum

Leslie D. Morgret

A multicomponent bimodal poly(vinyl acetate) (PVAc) polymer composite has been scientifically designed to increase biaxial plastic flow stabilization for the achievement of large biaxial deformations. For this, a systems-based approach was used for the computational materials design of a high performance bubblegum whose mean *in-vivo* bubble diameter exceeds that of its predecessor by 50% and is capable of inflation to diameters up to ∼11 inches. Furthermore, the designed bubblegum has bubble diameters comparable or greater than those of more complex, empirically developed, commercial bubblegums.

The relatively simpler bubblegum contains a bimodal PVAc molecular weight distribution (MWD) which imparts optimal biaxial flow stabilization through the use of a parametrically designed molecular weight ratio (MWR) and high molecular weight (HMW) fraction. The HMW portion of the PVAc gum base strain hardens during plastic deformation for the stabilization of uniform biaxial plastic flow.

A parametric thickness reduction model was developed from a literature survey of PE film blowing technology for the design of PVAc MWR and HMW fraction in bimodal PVAc gum

base. A secondary model describing the effects of gum base composition on gum viscosity was developed for the constraint of bimodal PVAc bubblegum designs to acceptable chew viscosities. These models were combined in the computational systems design of bubblegum prototypes.

In-vivo gum performance was characterized and mechanistically correlated to constitutive uniaxial exponential strain hardening behavior in gum base. A model was developed which indicates a transition from unstable to stable biaxial plastic flow at a uniaxial strain hardening parameter ($k = \frac{1}{\sigma}\frac{d\sigma}{d\varepsilon}$) of ~1.5 and indicating an onset of fracture mediated plastic flow at k-values above ~4.5. More directly, stabilizing exponential biaxial flow behavior was demonstrated using a semi-in vitro biaxial inflation technique.

Conceptual alternative molecular architectures were also investigated for the potential development of novel gum base systems. In this work, characterization was performed on two block copolymers with potential for enhanced biaxial strain hardening. Both systems demonstrated potential but were found to ultimately be insufficient for use as gum base additives for biaxial flow stabilization.

Approved by

Professor Gregory B. Olson

Department of Materials Science and Engineering

Northwestern University, Evanston, IL, 60208, USA

Acknowledgements

Bertrand Russell (1872-1970) once said, "Science may set limits to knowledge, but should not set limits to imagination." Personally, I feel that imagination opens science to new realms of possibilities, possibilities that are only shackled by the scientist's inability to dream. It is with unbounded imagination that I explore this life I am now living and therefore must thank those who gave it to me, Carol Duran and Larry Morgret. I thank you both for providing me with love, support, and encouragement in all aspects of my life. I truly feel like this journey could not have been completed without the both of you. I would also like to thank my step parents, Eddie Duran and Donnetta Morgret, for looking after me as your own. You have both brought happiness to my parents lives beyond that which could have been wished for.

To my brothers, Michael Morgret, Michael Duran, Eric and Troy Lewin. I thank you for keeping me grounded and never allowing me to lose sight of the importance of family. I have learned a great deal from each of you, although I fear I rarely tell you. Specifically, I would like to thank Michael for your companionship. I know we have not been the closest brothers but you have always been there for me when needed. Finally, to my step brothers, I thank you for welcoming me into your lives and look forward to coming even closer in the time to come.

To my fiancee, Courtney Holmes Lanier. If I had the ability to make a woman that I would call my wife forever, I could not have done a better job. You are my best friend, my confidante, my love. Thank you for agreeing to share this life with me. I look forward to the adventure that our life together promises to be and everything that goes with it. Mmmmwwwwaaaaaahhhhh!

To my friends, you know who you are. You have given me strength, clarity, and resolve to overcome many different obstacles in my life. For that, I thank you greatly. I also thank you for bringing me into your lives and teaching me about inspiration, sacrifice, humility, and unconditional love. My hope is that I have taught you a fraction of what you have taught me.

To my advisor, Gregory Olson. I envy your ability to look at the world not as it is but as it could be. I think your effort to make technology that, as per your words, will "change the world" is inspirational and feel like you have taken materials design to an artform much-like Jazz which you so often liken it to. I feel priviledged to have come to consider you as not just my advisor but also as my friend. Under your guidance, I have developed into "scieneer" that I am today, thank you for everything.

To my committee members, Kenneth Shull, Wesley Burghardt, and Xiaohu Xia. I thank you for your advice and assistance with this project. I know that this project never could have succeeded without your efforts and in many instances your lab space. You have all greatly affected my career and I hope that I can maintain the same high level of scientific excellence in my career as you have throughout yours.

To previous advisors, Alan Weimer and Jeffrey Hinkley. I thank you for starting me on this journey. I know that without your guidance I would never have been motivated to attend graduate school. You both showed me that research was both highly challenging and highly rewarding. I thank you both for your advice and mentorship.

To Olson group members past and present. Thank you for helping take the research edge off. It was always a pleasure stealing a few moments each week learning from or about each of you. I hope that each of you learned as much from myself as I did from you. I thank you for

sharing your backgrounds with me and wish you to know that I will carry these lessons with me the rest of my life.

To the research laboratories who have supported this work. I *literally* could not have completed this thesis without you. Specifically, I would like to thank Mark Seniw for his help and friendship. I learned almost as much in the lab as I did in how to be a kind, caring individual from you. Additionally, I would like to thank David Brass and the Shull group for allowing me to take over your lab space during the months while I was finishing my thesis.

Table of Contents

List of Tables

List of Figures

CHAPTER 1

Introduction

1.1. Motivation

Civilizations have been masticating natural-based resins for over two thousand years [1], and the first commercial chewing gum was a spruce-based gum which was inspired by North American Indians who chewed resins extracted from spruce trees. Natural-based gums, fueled by the introduction of chicle-based Adams New York No. 1 in 1869, dominated the commercial chewing gum market until introduction of synthetic gum base materials after World War II [2]. This time is commonly referred to as the "Age of Polymers" because it was an age of innovation motivated by the need for natural rubber-like synthetic materials. Synthetic polymers were invented rapidly and incorporated into all areas of American life. Their ultimate cost effectiveness, tailorable molecular structures, specific properties (strength, toughness, etc.), and processability (low melt temperatures, moldability, etc.) quickly made them ideal for applications ranging from chewing gum to stockings. However, as with any new material, exciting discoveries came with further study.

For instance, the extensional flow properties of polymers were found to be very unique and key to their utilization in and the development of new industrial processes such as fiber spinning, injection and blow molding, film blowing, and foaming. Fiber spinning and injection molding have primarily uniaxial extensional flows while the others, including polyethylene (PE) film blowing, are dominated by biaxial extensional flows. Polymer extensional flow knowledge was

qualitatively-based until advancements in their mechanistic characterization in the late 1960s - early 1970s [3–5]. New mechanistic characterization helped push the limits of polymer design because they were now sensitive enough to mechanistically understand molecular differences between polymers. Mechanistic polymer studies are still prevalent today because of their importance in polymer material design.

The performance of biaxial flow dominated processes such as PE film blowing has been predicted predominantly by the characterization of uniaxial extensional flow since the late 1970s [6]. Only recently have advancements in biaxial flow characterization allowed for the quantitative extension of qualitative knowledge [7–9], and with these new tools the first uniaxial-to-biaxial comparative data for high-density PE and low-density PE has been published [8].

Uniaxial and biaxial characterization methods will be implemented here for the design and validation of a bubblegum with maximized bubble diameter. Such combined methods provide a fundamental understanding of the mechanistic uniaxial and biaxial flow relationships governing bubble diameter performance, and this fundamental understanding is not only crucial for the design of a superior bubblegum but is also advantageous to the gum industry as a whole with applications to gum and gum base processing, chew performance, and removability.

For the purpose of this work, bubble diameter maximization helps the Wm. Wrigley Jr. Co.'s Hubba Bubba^{TM} product line defend markets where it shows strong leadership and improve in markets in which it is competitive. The key to bubble diameter maximization is the design of optimized biaxial flow stabilization in inflating bubblegum films. Flow stabilization is normally characterized under uniaxial extension, but polymers act differently than most materials, and ultimately polymers require biaxial flow characterization because their uniaxial and biaxial flow behaviors are quantitatively different.

This work emphasizes optimal biaxial flow design while simplifying current commercial bubblegum formulations. In the end, a simple bubblegum composition with optimal performance best positions Wrigley to compete for the $2 billion global bubblegum market [10, 11]. A simplified formulation has many cost reduction advantages including a decrease in number of suppliers and related conflicts, less regulatory requirements, less processing time and related worker compensation, and overall production efficiency improvement.

In the end, this work is not solely intended to increase bubble diameter but rather the intention is to use the example to demonstrate a general approach for the purposeful study, and design, of polymer composites such as bubblegum. The science-based materials design of bubblegum is meant as a first step in displaying its benefits and applicability to important industry problems such as gum base simplification, biodegradability, and removability. This approach to the design of new technologies is intended to help streamline new solutions to old problems. Through the use of material property quantification, modeling, and constraint, this approach has the unique ability to be an effective tool for the performance optimization of materials, such as bubblegum, with conflicting performance requirements.

1.2. Design Approach

Owing to the inherent complexity of bubblegum components, processing conditions, and the design criteria for chewable bubblegum, the quantification of their relationships is challenging. Consequently, the processing, structure, properties, and performance can no longer be treated sequentially as is customary in traditional materials science. Instead, a Materials by Design^{TM} approach employing systems engineering is required. Cyril Smith was the first in materials science and engineering to propose this concept, and treated material structures as divided into

a hierarchy of processing, structure, and properties subsystems each being strongly interacting components of the overall system [12]. In the end, overall system performance control is attained by designing the hierarchical interactions between subsystems.

The primary objective of this research was to increase *in-vivo* bubble size, with the specific goal to increase Hubba Bubba^{TM}'s mean inflation diameter by at least 50% via predictive design of biaxial stretch ductility. Additionally, a goal was to match the performance of empirically developed, highly complex, bubblegums such as Hubba Bubba^{TM} Max in a gum as simple as standard Hubba Bubba^{TM} by exploiting predictive mechanistic science principles. A secondary but equally important objective was to constrain designed gums to chew viscosities which are acceptable to the consumer.

Bubblegum was treated as two interconnected systems: the insoluble gum base and the soluble gum additives. Gum base is typically made of synthetic polymers (such as poly(vinyl acetate)), rubber elastomers (such as polyisobutylene), fillers (such as talc), and plasticizers (such as triacetin). Gum additives are typically flavors, colors, and sweeteners which are not promising design components for the increase of bubble size because of their propensity to diminish with increasing chew time. On the other hand, properly formulated gum base remains largely inert during mastication providing a promising design opportunity.

Poly(vinyl acetate) (PVAc) is the microstructural component forming the continuous phase in current gum base. As such, the properties of PVAc are expected to dominate those of the overall composite making it the most designable subsystem for increasing bubble size. Furthermore, preliminary research revealed the role of plastic flow stabilization in inflating gum bubbles, thus identifying the material property of designable significance in the PVAc subsystem.

The materials design of increased plastic flow stabilization in the gum base composite was guided by a review of film blowing technology. In this industry, thermoplastic polymers, are extruded through a die and inflated into a film. The inflation of polyethylene (PE) has been extensively studied, and blown film stability, film thickness homogeneity, and melt processability have been shown to depend on the amount of high molecular weight content [13–25] and/or the presence of long chain branching in the processed melt [14–17, 24–30]. An increase in either of these variables has been shown to increase a polyethylene melt's high molecular weight tail, broaden its molecular weight distribution (MWD), and increase its relaxation time, all of which resulting in a stabilized flow with an upward curving stress vs strain relationship. Accordingly, the materials design implemented in this work involved building a parametric model of the MWD effects in PE and applying it to PVAc, this work's goals were achieved by designing biaxial flow stabilization using a bimodal MWD in the continuous PVAc phase of the gum base matrix.

A "chewability" model was formulated in addition to the parametric model for the stabilization of gum inflation. A two sublattice solution model describing nonideal compositional dependence with Redlich-Kister polynomials was formulated to describe the compositional dependence of the complex viscosity of bubblegum designs. One sublattice was used to study the effects of shifting from a unimodal PVAc MWD to a bimodal PVAc MWD while the other was used to express the effects of triacetin and talc. Triacetin was selected because preliminary study showed it most effective in controlling gum viscosity, while talc was studied because of its potential negative ductility effects. For instance, fillers such as talc have been known to reduce strain hardening by causing unaligning shear flows instead of aligning extensional flows as

in uniaxial and biaxial deformations [31]. However, the effect of fillers on gum base and their resulting gums was found to be a positive one in low strain hardening gums.

1.3. Plan of Study

The goal of this study is to apply a systems-design approach to a bubblegum polymer composite for the purpose of increasing bubble diameter with respect to its commercial control by at least 50% at the mean. This goal is achieved by using quantitative modeling when available, and developing new models as necessary for bubble diameter performance optimization. Chapter 2 outlines relevant background information regarding the systems-design approach and the guidance of plastic flow theory in the conceptual design of a high-performance bubblegum. Appropriate polymer physical properties, like those in the PE film blowing process, and their utilization in this work will also be discussed and correlated with the systems design approach. Chapter 3 discusses the materials and methods studied in this work and provides mathematical derivations for important relationships used in the calculation of constitutive material behavior. Chapters 4 and 5 discuss the parametric MWD and chew viscosity models which were developed for the design of bimodal PVAc gum base prototypes. Chapter 6 primarily focuses on the fundamental characterization of conceptual prototype designs in the form of two block copolymer systems. These systems each have unique microstructural attributes that may, when properly implimented, aid the design of novel gum base prototypes. Chapter 7 discusses the parametric PE and chew model application for the design of bimodal PVAc gum base prototypes. Characterization is presented which shows the achievements of stabilized biaxial flow stability over the control and Hubba Bubba Max bubblegums in correlation with both uniaxial extensional flow and *in-vivo* bubble diameter experimentation. Chapter 8 presents an expansion

of the PE parametric model to a general parametric model with an inclusion of bimodal PVAc gum base prototype data for the prediction of a fourth generation prototype. Finally, Chapters 9 and 10 contain the conclusions and ideas for future exploration, respectively.

CHAPTER 2

Background

2.1. Materials as Systems

2.1.1. Systems-Engineering Overview

In 1972, Gwilym Jenkins gave a thorough review of how the overall systems-engineering approach replaced the prevalent piece-meal approach to the solution of complex problems [32]. He proposed the division of the overall system into a series of interacting subsystems which could be "designed, fitted together, checked and operated" so as to most efficiently achieve the overall objective [32]. A general systems-engineering outline is provided in Figure 2.1. In the systems analysis stage of this process, conflicting objectives are defined while subsystems are identified to achieve those objectives. Upon subsystem identification, systems design uses quantitative models which efficiently compromise between conflicting objectives and optimize the system for implementation. An iterative systems design is utilized when needed while guarding against "sub-optimization" where subsystems are optimized at the expense of the overall system.
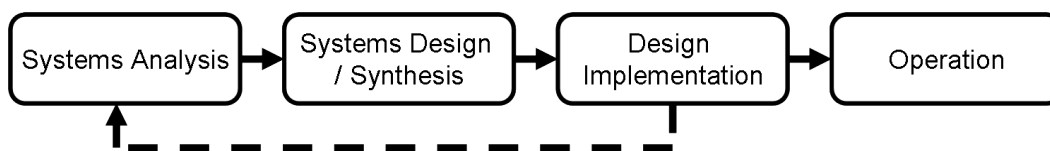
Figure 2.1. The four broad stages of systems-engineering design [32].

In an extrapolation of systems thinking to materials science, Cyril Stanley Smith urged a "need... for the study of real complexity, not idealized simplicity" [12]. Smith recognized materials as complex systems defined by a hierarchy of interacting subsystems. Special emphasis was placed on the interaction of subsystems because these relationships must be both qualitatively and quantitatively understood in an effort to achieve overall material performance optimization. Subsystem design was further expanded by Gregory Olson to include a linearization of the materials science processing, structure, properties, and performance paradigm, represented in Figure 2.2 [33]. Within this approach, Olson recognized that each of these subsystems could be further subdivided into their own hierarchy of interacting subsystems affording further flexibility for complex materials design.

Processing	Structure	Properties	Performance

Figure 2.2. Linear structure of primary materials domains [33].

Traditional "cause and effect" logic suggests that material scientific understanding evolves from left to right in Figure 2.2 (e.g structure controls properties). However, Morris Cohen added a pertinent "goal/means" point of view for the design of materials, regarding structure and properties as having "reciprocity" between both views [34, 35]. This approach allows the materials designer to move from right to left by translating performance goals into quantitative material property objectives. Property objectives are then met by defining the hierarchical interacting subsystems, both microstructural and processing, which help meet the property objectives through a combination of mechanistic and computational design.

The systems framework advantageously spans the extent of a material's life from process development to performance optimization. This approach succeeds where traditional approaches

employing empirical or trial and error do not. Whereas traditional approaches tend to be costly, time consuming, and ineffective at ascribing processing contributions to microstructural material components, the systems approach enhances efficiency by incorporating computational materials design in the development process. Computational description of interacting subsystems decreases cost and development time while increasing predictive scientific understanding. Generated knowledge is in the form of beneficial processing-structure-property subsystem interrelationships which are not recipe specific but instead applicable to the computational design of future materials. Ultimately, an intimate understanding of the key processing relationships which govern microstructural subsystems allow for the targeted optimization of material performance.

Successful application of this approach in metal alloys [33, 36] has employed quantitative structure/property relations to map property objectives to required microstructural parameters such as phase fraction and particle size which are in turn correlated to fundamental thermodynamic parameters accessible through computational thermodynamics. A demonstration of the applicability of this approach in the design of case hardenable multiphase polymers for gear applications has represented the polymer solution thermodynamics using the same Redlich-Kister polynomical approach that has provided suffcent accuracy in metal systems [37, 38]. These achievements provide both the strategic and tactical level foundation for the design approach adopted here.

2.1.2. A Systems Approach to Bubblegum Design

Hubba Bubba^{TM} Seriously Strawberry (HBSS) commercial bubblegum served as the control for this work. As Cyril Stanley Smith suggested for all materials, an "interpenetrating sequence of

structural levels" can be defined which demonstrates the inherent hierarchical system structure of HBSS bubblegum (see Figure 2.3) [12]. The HBSS systems design chart expresses the need for stabilized uniform plastic flow and increased biaxial fracture ductility for the achievement of desired bubble performance. Additionally, flow properties are represented as governed by the poly(vinyl acetate) (PVAc), polyisobutylene (PIB), and sugar components of bubblegum while biaxial fracture ductility is largely governed by dispersed talc ($Mg_3Si_4O_{10}(OH)_2$). A conflict between bubble size and chew viscosity performance objectives is related to PVAc, PIB, and talc which all strongly affect both.
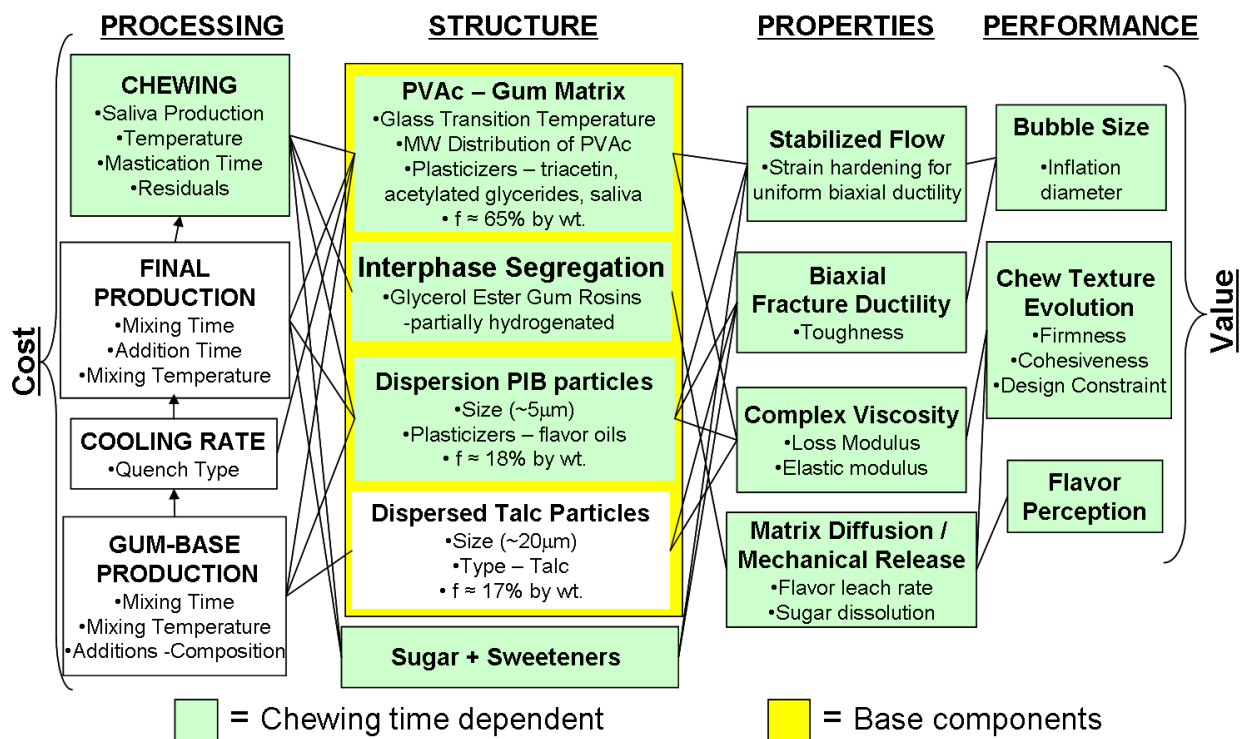
Figure 2.3. Bubblegum System Chart.

Gum is shown to be composed of an insoluble gum base which acts as a carrier to water-soluble additives in Figure 2.3. Realistically, water-soluble additives are of little importance

to the design of enhanced bubblegum because their dissolution is mostly completed during the first 5 minutes of mastication (shown in Chapter 5). After those 5 minutes, gum base is left as the primary masticated material known as the gum "cud", thus focusing the approach to "base" design. For this, PVAc is the primary microstructural component comprising $\sim$65 wt% of the gum base composition, with other components being PIB ($\sim$18 wt%), talc ($\sim$17 wt%), natural gum rosin, triacetin ($Mg_3Si_4O_{10}(OH)_2$), and fatty acids. The amount of natural gum rosin is proportionally subdivided between the PVAc and PIB portions because its role in gum base is as a compatibilizer. Fatty acids and triacetin are added to soften gum base and assumed to associate proportionately between PVAc and PIB as well, while talc was initially thought to only act as hard undeformable equiaxed particles ($\sim$20 μm) whose addition was primarily for cost reduction.

As mentioned previously, the PVAc subsystem was naturally focused on as the greatest microstructural opportunity for the design of a 50% or greater mean diameter and acceptable complex chew viscosity because it is the primary component of HBSS bubblegum base. This focus was supported by completion of an optical microscopy study on iodine stained inflated HBSS films revealed PVAc's existance as the *continuous* phase (Figure 2.4). Talc and PIB are also shown in Figure 2.4 but not expected to effect material properties as much as PVAc. The systems approach taken centered on the microstructural design of the molecular weight distribution (MWD) of the PVAc component of gum base to stabilize and thus impart uniform plastic flow for the achievement of large plastic strains during inflation. Preliminary studies showed a technological gap existing in the industry for the design of PVAc MWD requiring a shift to previously quantified knowledge in the technology of PE film blowing to push the limits of this design.
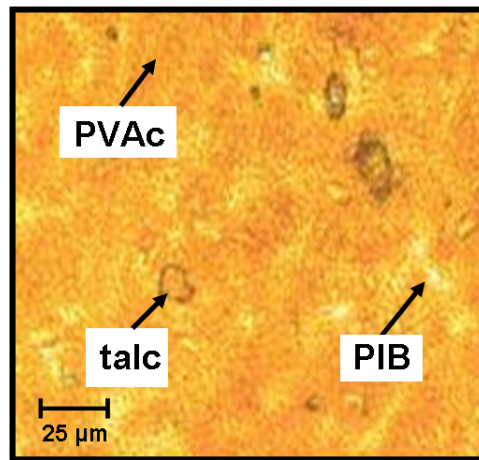
Figure 2.4. Transmission optical micrograph of iodine stained HBSS inflated film. Dark orange regions are iodine stained and PVAc rich, while lighter yellow regions are PIB rich. Talc is also visible.

The PE film blowing industry has extensively studied the effect of MWD on plastic flow stability since the 1970's [6], and thus, PVAc microstructural design for the flow stabilization of inflating bubbles relied largely on a parametric understanding of MWD effects studied in PE film blowing. Molecular weight ratio (MWR) and high molecular weight (HMW) fraction were found to be the primary structural parameters of interest because the literature depicts large flow stabilizing constitutive behaviors on moving from unimodal to bimodal MWDs. The motivation behind using such MWDs for the design of the PVAc microstructural component of bubblegum will be analyzed more extensively later in this chapter.

2.2. Previous Ductility Design Using Controlled Structural Transformations

Dr. Arup Saha's recent development of Blastalloy 160 "TRIP steel" provided the theoretical framework required for the design of stable uniform biaxial fracture ductility in this work [39–41]. Saha controlled stability by dispersing austenite into the martensitic steel matrix

of Blastalloy 160 to induce upward or sigmoidal stress-strain (σ-ε) curvature through the controlled structural transformation of austenite to martensite (similar to that shown in Figure 2.5). This behavior is known as transformation induced plasticity (TRIP). TRIP upward-curving constitutive behaviors are mimicked in this design because they have been known to impart high plastic flow stability by delaying necking and shear localization [42, 43].
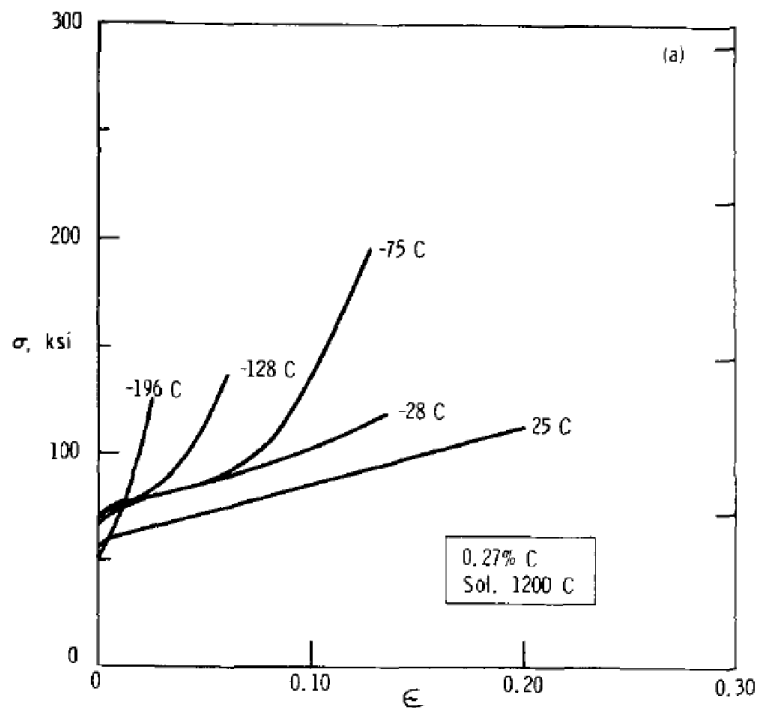
Figure 2.5. Tensile true stress vs true plastic strain behavior of a TRIP steel at varying temperatures [42]. The tests at -128 and -75 °C show the type of exponential strain hardening behavior that will be shown to be of interest to this study.

The design of Blastalloy 160 and high performance bubblegum are analagous in that they both require flow stabilization of a continuous matrix (ferrite vs compatibilized PVAc and PIB) filled with a less deformable dispersion (M_2C carbide *vs* talc particles). Furthermore, both designs require flow stabilization via an underlying structural transformation, where Saha's design

used an austenite to martensite transformation and the design presented here uses an unaligned to aligned molecular architectural transformation. The transformation in PVAc induces entanglement which resist and stabilize plastic flow. Upward curvature of the σ *vs* ε curve, similar to that depicted in Figure 2.5, will be shown to stabilize biaxial plastic flow in PVAc and increase bubble diameter.

2.3. Plastic Flow

2.3.1. Theory

Incipient instabilities cause localized thinning in plastically deforming materials which results in an unstable flow and failure [44]. Strain concentrates in this unstable, non-uniform, localized region because it offers the least resistance to flow. Flow resistance loss is prevented by stabilizing flow through material strain hardening which is defined as an increase of flow resistance with strain. Such stabilized plastic flows increase overall material ductility by restoring deformation to a uniform state. In essence, strain hardening can be thought of as a "self healing" mechanism which counteracts incipient instabilities and increases uniform plastic flow before failure [24, 45].

Constitutive behaviors of standard plastic and strain hardened plastic flow are seen in Figure 2.6. Downward true stress *vs* true strain curvature is characteristic of standard plastic flow (Figure 2.6A). In standard plastic flow an initial unecking instability results in large *localized* plastic strain which results in flow failure. Alternatively, strain hardened flows can have upward true stress *vs* true strain curvature resulting in a sigmoidal $\sigma - \varepsilon$ curve (Figure 2.6B). Such curvature increases flow resistance and increases plastic strain through the prevention of plastic flow localization.
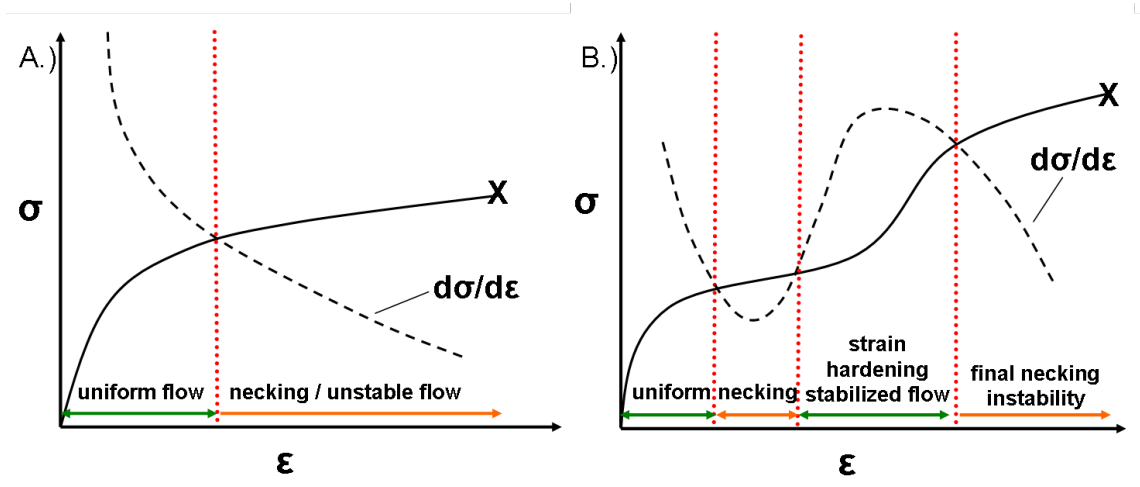
Figure 2.6. A.) Standard plastic flow behavior. B.) Strain hardened plastic flow behavior. Dashed line schematically shows the strain hardening ($\frac{d\sigma}{d\varepsilon}$) of the σ *vs* ε curve.

In general, strain hardened plastic flows are described by Equation 2.1 [44]. Temperature ($\frac{dT}{d\varepsilon}$) and interfacial ($\frac{d\gamma}{d\varepsilon}$) evolution with strain were not expected to contribute much to the strain hardening of PVAc or gum base. Their effects are greater in materials such as metal and soap where heat evolution and surface energy contributions, respectively, are comparatively more apparent. Additionally, strain-rate hardening ($\frac{d\sigma}{d\dot{\varepsilon}}$) is most beneficial (as in the case of glass blowing) in Newtonian viscous flows, which gum is not. Thus, strain hardening ($\frac{d\sigma}{d\varepsilon}$) was identified as the best opportunity for the design of gum base flow stabilization, and in turn, to increase biaxial stretch ductility for optimal bubble performance.

$$\frac{d\sigma}{d\varepsilon} = \frac{d\sigma}{d\varepsilon} + \frac{d\sigma}{d\dot{\varepsilon}}\frac{d\dot{\varepsilon}}{d\varepsilon} + \frac{d\sigma}{dT}\frac{dT}{d\varepsilon} + \frac{d\sigma}{d\gamma}\frac{d\gamma}{d\varepsilon} + \dots \tag{2.1}$$

Referring to an engineering σ *vs* ε curve, tensile deformation is uniform until maximum load (dF=0) at which point localized deformation forms as a neck [46]. This means that the point of maximum load is the *critical* condition for stable plastic fow. For tensile flows, a

stability condition in terms of true σ-ε is derived by differentiating Equation 2.2, the equation for applied tensile force, which results in Equation 2.3.

$$F = \sigma A \tag{2.2}$$

$$dF = \sigma dA + A d\sigma = 0 \tag{2.3}$$

At maximum load, Equation 2.3 can be rearranged to Equation 2.4 noting that $d\varepsilon = \frac{-dA}{A}$.

$$d\sigma/\sigma = -dA/A = d\varepsilon \tag{2.4}$$

When expressed in terms of strain hardening ($\frac{d\sigma}{d\varepsilon}$), the critical condition for stable tensile plastic flow occurs when strain hardening equals the flow stress (σ) (Equation 2.5).

$$\frac{d\sigma}{d\varepsilon} = \sigma \tag{2.5}$$

An ideal strain hardening behavior can be derived by integrating the stability condition of Equation 2.5, resulting in an exponential form of σ-ε (Equation 2.6). The pre-exponential factor (σ_o) is essentially the yield stress of the material while ε is the tensile strain. Ideal strain hardening increases a material's flow resistance at exactly the rate which its flow stress increases, thus minimally hardening to produce stable plastic flow.

$$\sigma = \sigma_o exp(\varepsilon) \tag{2.6}$$

In accordance with the above derivation, stable tensile plastic flows occur as long as $\frac{d\sigma}{d\varepsilon} \geq \sigma$ or $\frac{d\sigma}{d\varepsilon} = k_i\sigma$, where $k_i > 1$ and is known as a strain hardening parameter where i is either U or B for uniaxial or biaxial extensional flows, respectively. However, too much hardening

can be detrimental as it can lead to increased flow resistance to the point where non-stability related failure mechanisms are dominant (e.g. filler fracture mediation, interfacial debonding, etc.). These relations result in a generalized equation for exponential strain hardening given in Equation 2.7. This equation has greater utility in that unstable plastic flows are characterized by k_i values less than 1, ideal stable flows are characterized by k_i equals 1, and more stable flows are characterized by k_i values greater than 1. It should be noted that this type of equation only models the exponential strain hardening region after initial plastic yielding.

$$\sigma = \sigma_o exp\left(k_i \varepsilon\right) \tag{2.7}$$

The general expression for exponential flows has been used to describe strain hardened flows for many different materials including metals, doughs, and filled and unfilled polymers [31, 44, 47–49]. Hosford has generalized the expression in terms of effective stress ($\overline{\sigma}$) and strain ($\overline{\varepsilon}$) for the description of other flows, such as balanced biaxial. In the case of balance biaxial, the ideal exponential is represented by Equation 2.8 when k_B equals 1. This relationship will be used in the discussion of results in later chapters.

$$\overline{\sigma} = \overline{\sigma}_o exp\left(k_i \overline{\varepsilon}\right) \tag{2.8}$$

2.3.2. Thermoplastic Polymer Strain Hardening and Polyethylene Film Blowing

For this design, it is important to understand that strain hardening is inherent in thermoplastic polymers such as PVAc, provided the molecular weight is higher than that critical for entanglement ($M_c \approx 25$ kg/mol for PVAc) [5, 50, 51]. If so, external forces which are imparted on these high molecular weight polymers cause structural alignment during elongation resulting in

entanglement-induced strain hardening. This strain hardening is caused by the forming, break-
ing, and reforming of temporary physical cross-links as described via the de Gennes reptation
theory [52, 53]. De Gennes depicts a polymer wriggling within an imaginary tube of con-
finement caused by physical cross-links with surrounding chains (Figure 2.7). This constraint
results in a spectrum of relaxation times accompanying disentanglement (i.e. C-C backbone
vs side chains, local *vs* overall chain, entangled *vs* disentangled regions, high MW *vs* low MW
regions, etc.) and governs polymer flow [52].
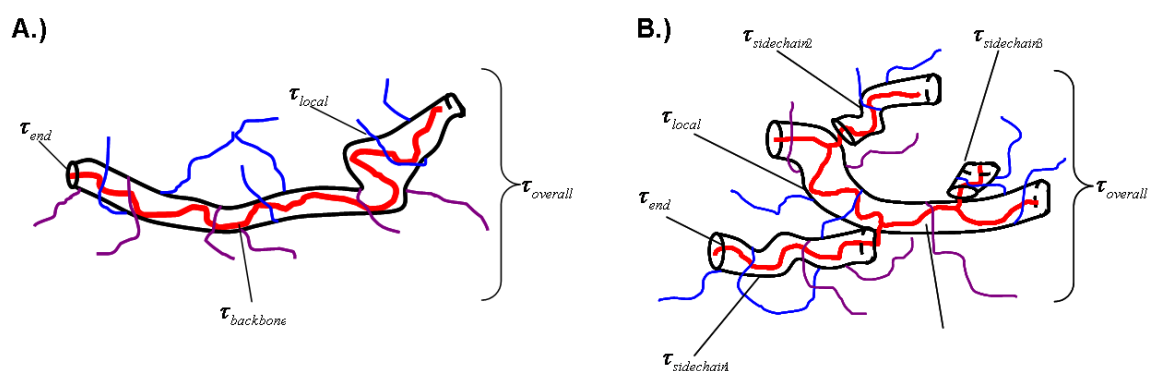
Figure 2.7. A.) Typical relaxations in a linear polymer chain. B.) Typical relax-
ations in a branched polymer chain.

De Gennes' theory is quite successful in predicting many polymer behaviors including the
3.4 power-dependence of zero shear viscosity on molecular weight when $M > M_c$ (Equation
2.9 and 2.10) [54, 55]. Such dependence infers increased reptation / relaxation times with in-
creased molecular weight (Equation 2.9), suggesting a molecular basis for gum strain hardening
induction via the incorporation of higher PVAc molecular weights. Bimodal broadening of the
MWD in this way lengthens the material's overall relaxation time, increases its resistance to,

and stabilizes flow through strain hardening which is the underlying concept of this design.

$$\eta \approx \lambda_{rep} \approx M^3 \tag{2.9}$$

$$\eta_o \approx M \quad M < M_c$$

$$\eta_o \approx M^{3.4} \quad M > M_c \tag{2.10}$$

MWD broadening is accomplished in the PE film blowing industry by spiking a polymer of "distinctively" higher molecular weight into one of lower molecular weight [13–25] or chemically modifying its chain architecture to include long-chain branches (LCB) [14–17, 24–30]. Both methods increase a polymer's high molecular weight component, result in a bimodal MWD, and lengthen its relaxation times. The former method is utilized in this research owing to its comparative ease of implementation.

An example of how a bimodal PE MWD exhibits ideal tensile strain hardening is shown in Figure 2.8. In this case, an unstable unimodal linear low density PE (LLDPE) was compared to a stable long chained branched low density PE (LDPE) with a molecular weight ratio (MWR) of ~20 and a high molecular weight (HMW) fraction of ~30% [6, 20, 27]. The bimodal MWD has an average low molecular weight comparable to the overall molecular weight of the LLDPE resins and therefore acts as a bimodal comparison to the unimodal LLDPE melt. The bimodal MWD is seen to improve the tensile strain hardening of the PE melt toward the ideal exponential. Further discussion of the types of molecular architectures of particular interest to this work is given in Chapter 4.
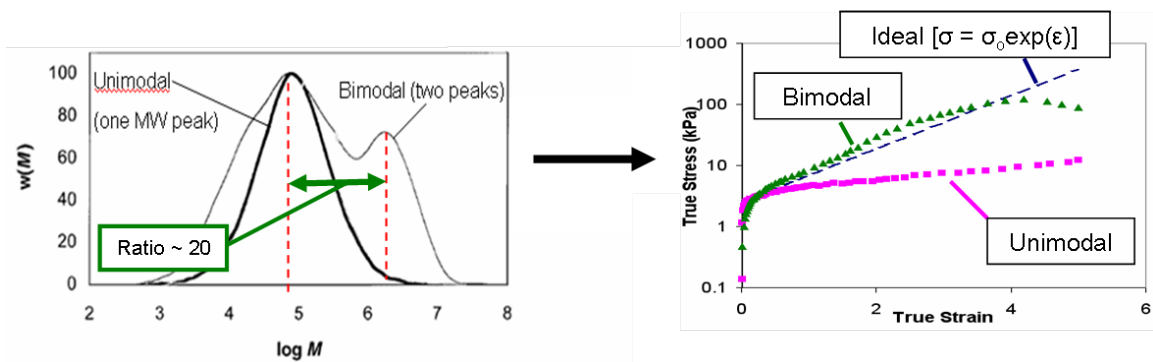
Figure 2.8. Uniaxial extensional flow comparison of a unimodal and bimodal PE MWD (0.05 s^{-1}, 150 °C) [28]. Bimodal MWD is shown approach the ideal exponential for stable plastic flow.

2.4. Uniaxial *vs* Biaxial Extensional Flow

Uniaxial extensional flows have proven to be good predictive indicators for PE melt film blowing performance. However, a less extensive body of evidence exists for the relationship between tensile uniaxial and biaxial flows owing to a lack of comparative data. For instance, uniaxial extensional flows have been observed for many thermoplastic polymers including polybutadiene [17], poly(methyl methacrylate) [19], polystyrene [13, 18, 21], polypropylene (PP) [18, 22, 23, 26, 30, 49] and polyethylene (PE) [14–16, 20, 24, 25, 27–29, 56–58], whereas equibiaxial elongational flows have only been extensively studied for PE, although some work on PP has been completed as well [8, 18, 23, 56, 59]. Interestingly, for those research groups who have studied strain hardening in uniaxial and biaxial flows, the intensity to which they relate seems to vary [8, 17, 18, 56, 60]. Such differences have been credited to a difference in degree of molecular alignment: rather than elongating and aligning in one direction as in uni-axial flows, biaxial flows elongate in two directions allowing less flow resistance and resulting in less strain hardening. It should be noted that some of the differences in agreement about the

relationship of uniaxial and biaxial flows results from the difficulty which accompanies biaxial measurements, more of which will be explained below.

Clarifying this relationship is important in the understanding of many polymer processes (film blowing, blow molding, fiber spinning, etc.). Numerous techniques have been designed for this purpose including lubricated compression, sheet stretching, bubble inflation, and stagnation flow methods [5]. The most commonly used techniques are require rotary clamps or lubricated squeezing flows (LSF) [8, 9, 59]. The reason why so few successful techniques have been developed is because it is extremely difficult to obtain homogeneous equibiaxial flow while reaching a steady stress state and maintaining sample uniformity [5].

Much of the data that has been collected for the characterization of biaxial flow phenomena in PE and PP has used the LSF method. This method is the most popular of its kind and has many advantages including easy force measurability, minimal time consumption, small sample size requirements, and easy implementation for broad temperature ranges [5]. Recently, however, this method has been demonstrated to be very difficult for the achievement of biaxial true strains ($\varepsilon_B^T = \varepsilon_B^H > 1 - 1.5$) without an external lubricant supply [5, 59]. Such difficulty arises because thin lubrication layers and edge stresses increase friction which results in drag flows. Drag flows are undesirable because they increase force measurements and falsely predict biaxial strain hardening if not adequately prevented.

By comparison, Meissner's equibiaxial rotary clamp rheometer is more complex due to its various moving clamps, cutting scissors, leaf springs, and control coordination but more reliable than the LSF method [8]. This rheometer works through the simultaneous action of a series of eight rotary clamps situated around the perimeter of a circular sheet. Its advantages

are that it can achieve homogeneous deformations up to equivalent strains of 3 (Figure 2.9). Its disadvantages are that it is complex and requires larger samples.
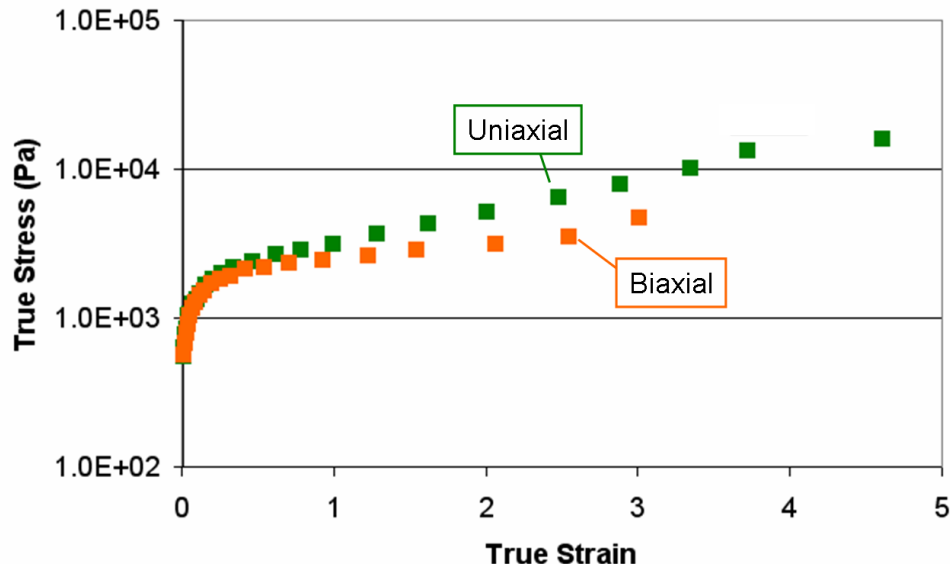
Figure 2.9. Uniaxial *vs* biaxial extensional flow comparison for an HDPE melt (0.1 s^{-1}, 150 °C) [8].

Hachmann and Meissner recently published results from the rotary clamp technique showing twice as much strain hardening for uniaxial vs equibiaxial flow (k_U/k_B=2) of a high density polyethylene (HDPE) melt (Figure 2.9) [8]. This technique's ability to reach biaxial true (Hencky) strains of ($\varepsilon_B^T = \varepsilon_B^H$) of ~3, compared to the LSF technique's ~1, makes it the standard for such measurements. Due to the relative lack of data, no literature models have correlated uniaxial and biaxial strain hardening. As inferred, comparative research like this is needed to fully describe the qualitative and quantitative relationships of uniaxial and biaxial material flows.

2.5. Filler Effects on Composite Flows

In the end, after all stabilization has been perfected and gums have been designed they must be compatible with the use of filler to keep gum base cost reasonable. Thus, understanding filler's effect on base properties is very important. First, increased filler fraction normally increases Young's modulus and yield stress while decreasing fracture strain, but this depends on the matrix and filler properties [61–64]. Filler effects are governed by particle size [65–67], aspect ratio [68, 69], surface chemistry [70–72], and filler modulus [62, 63]. Filler's effect on strain hardening is of particular importance here. Many researchers have observed decreased strain hardening with increasing filler fraction, decreasing filler size, and increasing aspect ratio [31, 68, 69, 73–75]. This is thought to be due to increased localized "shear and biaxial stretching" near or between particles [31]. Better interfacial adhesion prevents these localized flows and favors matrix domination of plastic flow and diminished filler effects. Depending on adhesion, fillers and matrix strain hardening can counter each other during plastic flow.

2.6. Polymer Thermodynamics

Thermodynamic predictions have been used to better assess the effect of triacetin on gum base in an effort to describe gum properties in addition to better understanding quantitative structural transformation assisted flow stabilization. Solubility parameters (δ) have been proven to work well in many areas of fundamental research including solvent selection, polymer miscibility, and filler surface characterization [76]. They were first described by Hildebrand and Scott as a measure of cohesive energy density (CED) in the 1940's [77]. Solubility parameters are calculated from the square root of cohesive energy density (Equation 2.11). Cohesive energy densities are found by measuring the total energy (E) required to vaporize a volume (V) of

pure liquid. In all, solubility parameters are a measure of how strongly molecular structures associate. As seen below, their use has been expanded to the prediction of interaction favorability between molecules of differing molecular structure. This will be explained further below while being used as a modeling aid in understanding the partitioning of bubblegum's components.

$$\delta = \sqrt{CED} = \sqrt{\left(\frac{E}{V}\right)} \qquad (2.11)$$

As an interaction measure, solubility parameters predict the thermodynamic tendency for two materials to mix. Patterson *et al.* demonstrated the use of solubility parameters in this way by calculating the noncombinatorial free energy of mixing (Equation 2.12), where ϕ_1 and ϕ_2 represent the volume fractions of interaction components which are usually a solvent and polymer, respectively [78, 79]. The molecular volume is represented by V_M. Closer solubility parameter values favor mixing by diminishing noncombinatorial entropy. Matching parameters result in noncombinatorial entropy cancellation and ensure thermodynamic mixing from combinatorial entropy.

$$\Delta G_{noncomb}^M = \phi_1 \phi_2 V_M \left(\delta_1 - \delta_2\right)^2 \qquad (2.12)$$

Although Hildebrand and Scott's total solubility parameter (δ) reasonably predicts material thermodynamic interactions for many materials, it often fails for materials with strong polar and permanent dipole forces [76]. Thus, Hansen divided the total solubility parameter into three parts representing dispersion (δ_D), permanent dipole-permanent dipole forces (δ_P), and hydrogen bonding (δ_H) interactions (Equation 2.13) [76]. Others have further divided the total solubility parameter, but Hansen solubility parameters are sufficient for this work.

$$\delta^2 = \delta_D^2 + \delta_P^2 + \delta_H^2 \qquad (2.13)$$

Attempts to calculate solubility parameters from experimentally determined quantities have been made, but most parameters are found by either using structurally well-defined solvents as molecular probes for polymer solubility or synergistic solvent-solvent interactions [76, 80]. Each molecular group's contribution to the molar attraction constants ($F_{D,i}$, $F_{P,i}$, and $E_{H,i}$) are tabulated in Appendix A for parameter estimation (Equations 2.14-2.16) [76, 81].

$$\delta_D = \frac{\sum F_{D,i}}{V_M} \tag{2.14}$$

$$\delta_P = \frac{\sqrt{\sum F_{P,i}^2}}{V_M} \tag{2.15}$$

$$\delta_H = \sqrt{\frac{\sum E_{H,i}}{V_M}} \tag{2.16}$$

The Flory-Huggins expression can be used to predict polymer-polymer and polymer-solvent miscibility (Equation 2.17) [51]. This theory describes an ideal polymer solution resulting from a randomly mixed lattice. The theory accounts for a volume-dependent entropy of mixing (first two terms on the right side of the equation) as well as a volume-independent enthalpy of mixing (last term on right side). The number of polymer subunits is denoted by N_1 and N_2, where a solvent is taken to have a value of one. Volume fractions are denoted by ϕ_1 and ϕ_2 while $\chi_{1,2}$ is the enthalpic molecular interaction parameter. Volume, temperature, and Boltzman's constant are lumped as a normalized version of the free energy of mixing (left side of equation).

The Chi parameter ($\chi_{1,2}$) is of particular significance to this work as it is a measure of a molecule's self-interactions compared to its interactions with another moiety. It is of primary importance when determining polymer-polymer miscibility because the large size of polymer molecules results in small positive, and sometimes negative, entropic free energy contributions,

requiring the entire driving force for mixing to come from the enthalpic contribution governed by $\chi_{1,2}$. A critical chi parameter (χ_c) of $1/2$ is defined which stands for the limiting value above which polymer-polymer miscibility is impossible. This critical value does not pertain to solvent-polymer interactions because solvents are small enough to not be entropically limited.

$$\frac{\Delta f_{mix} V_o}{k_B T} = \frac{\phi_1 ln\phi_1}{N_1} + \frac{\phi_2 ln\phi_2}{N_2} + \chi_{1,2}\phi_1\phi_2 \tag{2.17}$$

Patterson *et al.* showed that $\chi_{1,2}$ could be calculated from Hansen's three solubility parameters using Equations 2.18 and 2.19 [79]. Multiplication of the squared differences of polar and hydrogen bonding character by $1/4$ is an effect of the geometric mean rule. Equation 2.19 accounts for the solvent molar volume (V) and temperature (T) effects. Molar volume can be estimated from group contributions but the presented calculations assumed it equal to the solvent's molecular weight divided by its density. Additionally, the temperature was taken to be that of the mouth (37 °C). Smaller values of $\chi_{1,2}$ are desirable because they favor mixing by promoting combinatorial entropy.

$$A_{1,2} = (\delta_{D2} - \delta_{D1})^2 + \frac{1}{4}\left((\delta_{P2} - \delta_{P1})^2 + (\delta_{H2} - \delta_{H1})^2\right) \tag{2.18}$$

$$\chi_{1,2} = \frac{V A_{1,2}}{RT} \tag{2.19}$$

PVAc-flavor interactions are immediately seen as thermodynamically favorable upon inspection because calculated $\chi_{1,2}$ interaction parameters are small. PIB does not show such favorability suggesting that flavor plasticization is primarily confined to the PVAc phase of the gums being designed. More importantly though, both PVAc and PIB are shown to associate favorably with triacetin, the primary plasticizer of gum base, in Figure 2.10 up to 60 and 43 vol%,

respectively. This implies triacetin plasticizes both the PVAc and PIB phases therefore being the most effective component for controlling chew viscosity constraints modeled in Chapter 5.
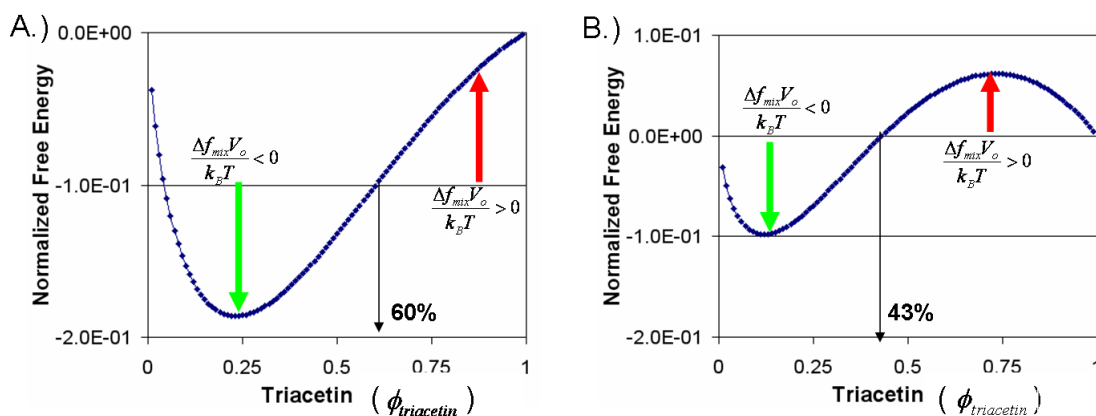
Figure 2.10. Normalized free energy diagrams for triacetin associating with A.) PVAc and B.) PIB. Favorable interactions are characterized by negative free energy values therefore predicting up to a 60 and 43 vol% uptake for PVAc and PIB, respectively.

Evidence exists that suggests water interacts favorably with PIB and PVAc up to 70 wt% and 100 wt%, respectively. This lends theoretical evidence to the notion of saliva (99.8% water) plasticizing gum during mastication. These predictions are largely aided by the fact that water is a much smaller molecule than previously mentioned solvents and thus interacts more easily.

Table 2.1. Thermodynamic Parameter Calculations for Miscibility Prediction

Polymer $\rightarrow$	PVAc		PIB	
Gum Component	$A_{1,2}$	$\chi_{1,2}$	$A_{1,2}$	$\chi_{1,2}$
Vanillin	5.2	0.29	63	3.5
Ethyl Isobutyrate	5.7	0.30	17	0.88
Water	51	0.36	162	1.1
n-Butyl n-Butyrate	6.3	0.40	13	0.83
Benzyl Alcohol	15	0.59	58	2.3
Triacetin	12	0.86	20	1.5
PIB	37	1.0	-	-

The literature suggests PVAc only absorbs water up to 4 wt% (molecular weight not known) suggesting either error in the predictions or a kinetically limited interactions [81].

In Table 2.1, the $\chi_{1,2}$ parameter calculated for PIB mixing with PVAc is significantly above $\chi_c = 0.5$. Flory-Huggins polymer solution theory suggests these two polymers are completely immiscible which is shown in Figure 2.11. This adds additional concerns when trying to make a super bubblegum in that phase interfaces are points of stress concentration which may cause failure. Fortunately, as indicated in Figure 2.4, phases appear well mixed due to decreased phase separation of filled gum base.

$$\frac{\Delta f_{mix} V_o}{k_B T} > 0$$
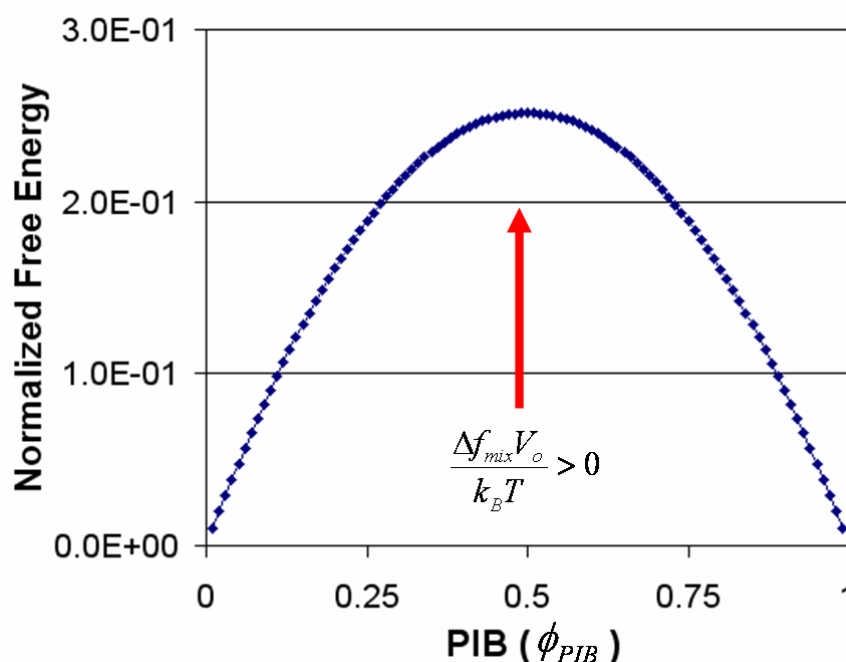
Figure 2.11. Normalized free energy diagram showing immiscibility for PIB mixing into PVAc.

Ultimately, solubility parameters are useful for the assessment of gum base and gum phase relations but do not estimate the interaction kinetics. Therefore, thermodynamically favorable interactions might not be kinetically feasible. Additionally, the further from zero $\chi_{1,2}$ is, the

longer it is expected for diffusion to occur. Thus, kinetics should always be kept in mind when interpreting such theoretical predictions, especially for polymer-polymer interactions where steric structure effects dominate interaction kinetics.

CHAPTER 3

Materials and Methods

3.1. Materials

Neat polymers, bubblegum base, and bubblegum have all been studied in this work. These materials range from simple to complex depending on the amount of processing, number of components, and molecular architectures present (recall Figure 2.3). Neat polymers were studied to conceptually validate the current design approach, validate models, and probe other molecular arhitectures of possible interest for gum applications. Gum base was studied to show that underlying gum base characteristics demonstrated in the neat polymers dominate masticated gum rheological behavior. Finally, bubblegum was characterized for model development and prototype bubble performance.

3.1.1. Neat Polymers

Pre-processed neat materials such as poly(vinyl acetate) (PVAc), polyisobutylene (PIB), and talc ($Mg_3Si_4O_{10}(OH)_2$) have been studied to understand their effect on bubblegum base, non-ideal bubblegum linear viscoelastic mixing, and extensional flow constitutive behaviors. PVAc was supplied by Wacker Polymer Systems GmbH & Co. in the form of Vinnapas^{TM} B1.5sp, Vinnapas^{TM} B17sp, Vinnapas^{TM} B30sp, and Vinnapas^{TM} UW 10fs. Unimodal (as supplied) and bimodal (additional processing) molecular weight distributions were studied to better understand the underlying polymer physics in our high performance bubblegum designs.

Table 3.1. Neat Gum Base Component Characteristics [82]

	Polymer	M_W, kg/mol	T_g^a, °C	Residual Monomer, ppm
Vinnapas® B 1.5 sp	PVAc	10-15	29	<5
Vinnapas® B 17 sp	PVAc	35-45	34	<5
Vinnapas® B 30 sp	PVAc	45-55	35	<5
Vinnapas® UW 10 fs	PVAc	330-430	37	$<1000^b$
Vinnapas® B500/20VL	PVAVL	125-175	-	<5

a.) Measured on Mettler DSC 822e with 10 °C/min heating/cooling rate.
b.) Personal communication with Wacker contact.

Neat styrene-isoprene (SI) block copolymers were also investigated for the conceptual molecular architectural study of their biaxial constitutive behavior. Binary diblock (SI) / triblock (SIS) blends were studied to understand their nonlinear biaxial elastic behavior at large strains. SIS and SI/SIS blends were supplied by Dexco (a joint venture between Dow Chemicals and Exxon-Mobil). Blends are differentiated by their respective diblock weight fractions (ranging from 0 to 54 wt%) with other molecular characteristics given in Table 3.2. Polystyrene content is seen to be held constant while the M_W(SIS) to M_W(SI) ratio is $\sim$2.

3.1.2. Gum Base

Gum base starts as a minority component of gum until mastication dissolves away almost all soluble gum components. At this point, an understanding of the effect of the design of the PVAc component of gum base is important. As mentioned in Chapter 2, gum base is a multicomponent

Table 3.2. Molecular Characteristics of the Four Model SIS/SI Blends [83]

	wt% SI	M_W(SIS), kg/mol	wt% S in SIS	M_W(SI), kg/mol	wt% S in SI
Vector 4100 D	0	154	15.1	-	-
Vector 4113	19	154	15.1	72	15
Vector 4114	42	156	15.1	72	15
DPX 565	54	176	16.1	72	16

multiphase polymer composite made of poly(vinyl acetate) (PVAc), polyisobutylene (PIB), talc ($Mg_3Si_4O_{10}(OH)_2$), triacetin ($C_9H_{14}O_6$), resin, oil-based plasticizers, and antioxidants. These components are sequentially combined during mechanical mixing at temperatures above $100\,^\circ C$ for $\sim$25-90 minutes (depending on mixer). The polymers, talc, and triacetin are added early in the process to allow time for compounding before adding the resin compatibilizer. Finally, oil-based plasticizers are added to further soften the gum base and antioxidants such as butylated hydroxytoluene (BHT) are added to prevent polymer oxidation and chain scission.

Additional processing was required for high performance bubblegum bases designed in this work because they were designed to have a higher ($\sim$10x) PVAc molecular weight than normally used in gum base. For example, prior to mixing Vinnapas® UW 10fs was first swollen and congealed for 3-12 hours at $\sim$100 $^\circ C$ from its pelleted size ($<$1 mm) to a gel using triacetin and/or other plasticizers. This gel was transferred into the mechanical gum base mixer during compounding with no other changes in processing required.

Gum base was studied in shear rheological and uniaxial extensional flow to assess its contributions to bubblegum linear viscoelastic behavior and the effect of PVAc molecular weight distribution on uniaxial strain hardening, respectively. Uniaxial strain hardening was then correlated to *in-vivo* bubble performance for each gum base's resulting gums.

3.1.3. Gum

Gum was processed similarly to gum base. Gum base was preheated at $\sim$70 $^\circ C$ and sequentially mechanically mixed with water-soluble additives such as sweeteners, colors, and flavors at $\sim$50-60 $^\circ C$. Primary components such as sugars and artificial sweeteners were added with the gum base to the mechanical mixer while more volatile components like flavors were added near

the end of processing. Gum was mixed for ∼4-15 minutes (depending on mixer), cut into bubblegum chunks, and sealed in air tight bags for aging. Gum was allowed 1-2 weeks of aging before testing to allow time for sugar crystallization, gum cohesion/homogenization, and flavor diffusion. In industry, this time represents shipping and stocking time and must be afforded at the gum design level because some gums are known to be prone to decohesion and disintegration without proper aging.

Gum was studied in shear rheological and biaxial extensional flow to assess its base's contributions to bubblegum linear viscoelastic and biaxial constitutive behavior, respectively. PVAc molecular architecture effects were further studied with to correlate uniaxial strain hardening, biaxial strain hardening, and *in-vivo* bubble diameter.

3.2. Experimental Methods

3.2.1. Uniaxial Extensional Flow

Extensional flow characterization is very important to this work because strain hardening is not detectable in shear flow but very evident in uniaxial extension [5]. Tensile specimens were prepared using a Mini-Max injection molder. Gum base was heated at 120-140 °C (∼temperature of base mixer) and mixed into a homogeneous viscoelastic fluid. This fluid was plunged into a metal mold (0.5-1.0 cm gauge length) and then quenched in a refrigerator to reduce phase separation and prevent sample inhomogeneity. Samples were refrigerated until use and equilibrated at room temperature for ∼15 minutes before testing.

An electromechanical Syntech machine was employed since neither Meissner- [3] nor Munstedt-type [4] elongational rheometers were available. This machine was programmed to pull on each sample with an exponential crosshead (length) profile so as to apply a constant true strain

rate [5]. Instantaneous uniaxial true stress and strain were calculated using Equations 3.1 and 3.2 the output values from the LaserMike. Equation 3.1 was used assuming sample width to be the same as thickness, which was typically good to less than 10% error. Additionally, gum base was assumed to be incompressible allowing calculation of uniaxial tensile strain via Equation 3.2. From incompressibility, as length increases width decreases twice as much therefore resulting in the factor of 2 in Equation 3.2.

$$\sigma_T = \frac{P}{w(t)^2} \tag{3.1}$$

$$\varepsilon_T = \dot{\varepsilon}_{T,instantaneous} * t = -2 * ln\left(\frac{w(t)}{w_o}\right) \tag{3.2}$$

Samples were pulled at an ideally constant true strain rate of $5.6\text{x}10^{-3}$ s^{-1} (bubble strain rates are $\sim$0.2 - 0.4 s^{-1}). The slope of thirty linear segments increased at 30 second intervals approximating an exponential profile. The machine's maximum crosshead speed of 500 mm/min determined the slope of the final linear segment with the other slopes adjusted accordingly. Maximum measurable tensile equivalent strain is 4.91 with a sample of 0.5 cm gauge length and a 67.8 cm travel distance.

The uniaxial extensional flow set-up and reproducibility are shown in Figures 3.2 and 3.1, respectively. Here, a LaserMike is seen sitting on a platform which can be raised manually to keep the the LaserMike centered on the sample during testing. A digital readout for the instantaneous gauge width is stored and synchronized with the load output. True stress and strain are calculated as previously described.
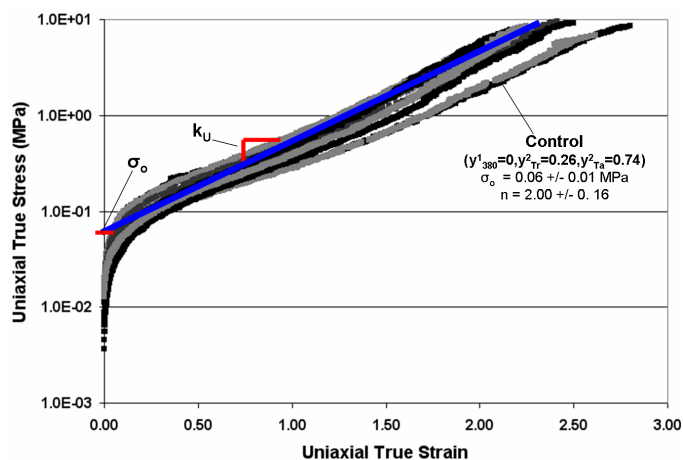
Figure 3.1. Uniaxial extensional testing reproducibility at 0.006 s^{-1} and 22 °C.

3.2.2. Biaxial Extensional Flow

3.2.2.1. Biaxial Testing. A bubble inflation technique for the characterization of adhesive interactions was developed by Flory, Brass, and Shull [84]. This technique was modified with their help to characterize large strain biaxial constitutive flow behavior in a manner similar to other inflation methods seen in the literature [7, 85–93]. This method was used to characterize neat unimodal and bimodal PVAc, SIS/SI block copolymer blends, and bubblegums.

The instrument is composed of a syringe pump (NE-100), a differential pressure transducer (MKS Baratron), a Hitachi CCD camera, and a membrane holder. The syringe pump can inflate membranes up to 1000 mL/h while pressure can be measured up to 0.1 MPa. The membrane holder was different for the neat polymers and gums because of how the differing membranes needed to be secured. Neat polymers were thin enough (1-3 μm) to be secured by adhering them to the surface of a glass cylindrical expansion chamber having a 7 mm inner diameter. Gums ($\sim$0.75 mm) were secured with an outer ring that clamped a gum cud into place around a stainless steel cylindrical expansion chamber having a 15.6 mm outer diameter. Dimensions for
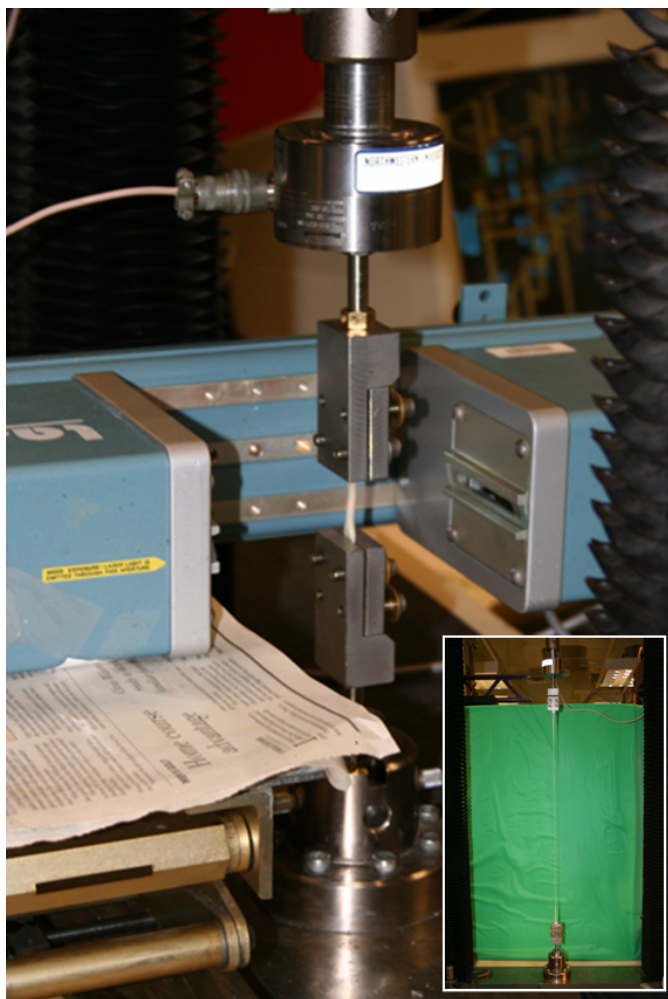
Figure 3.2. Uniaxial extensional testing set-up showing position of LaserMike in relation to deforming sample as well as it sitting atop a mechanically moveable platform for measuring strain in the middle of the test sample.

these holders are given in this manner because of how stress and strain are calculated and will be further explained below. Finally, data was collected using a LabView 7.0 program which records the pressure and image (up to 10/sec) of an inflating membrane simultaneously.

Neat membranes were prepared by spin coating different toluene solutions on a NaCl crystal at 2,000 rpm for 30 seconds. SIS/SI block copolymer blends were made using 10-15 wt% solutions while neat unimodal and bimodal PVAc were made using 15-20 wt% solutions. These

membranes were floated onto water and transferred to the glass cylinder manually. A wet Kimwipe® was used to press the membrane firmly against the glass surface to prevent peeling.

Gum membranes were prepared by finger chewing $7.00 +/- 0.02$ g bubblegum pieces for 10 min in a 37 °C water bath. Cuds were then pressed to a 0.75 mm thickness between two mylar sheets coated with mold release for 5 min at 37 °C. After 5 min, this cud was transferred to be pressed at room temperature for another 5 min. After pressing, cuds were placed in a refrigerator to stiffen so that they could be extracted from the mylar sheets. Cuds were stored in a refrigerator until use at which time 7 inflatable membranes could be cut from each cud.

This membrane inflation technique was used to calculate true biaxial stress and strain from the measurement of inflation pressure (P) and deflection distance (δ) (seen in Figure 3.3). This calculation is performed by first understanding that the undeformed membrane is circular giving it an initial radius of R_m and an initial thickness of h_o. For simplicity, the undeformed membrane area (A_o) and normalized displacement ($\overline{\delta}$) are used to describe membrane deformation (Equation 3.3). Equations 3.4, 3.5, and 3.6 are expressions for deformed area (A_m), deformed volume (V_m), and radius of curvature (R), respectively, assuming that a membrane deforms as a spherical cap.

$$A_o = \pi R_m^2 \quad , \quad \overline{\delta} = \delta/R_m \tag{3.3}$$

$$A_m = A_o \left(\overline{\delta}^2 + 1 \right) \tag{3.4}$$

$$V_m = A_o \delta \left(\frac{\overline{\delta}^2}{6} + \frac{1}{2} \right) \tag{3.5}$$

$$R = \frac{\delta^2 + R_m^2}{2\delta} \tag{3.6}$$

Engineering and true biaxial strain are calculated from the film area increase using Equations
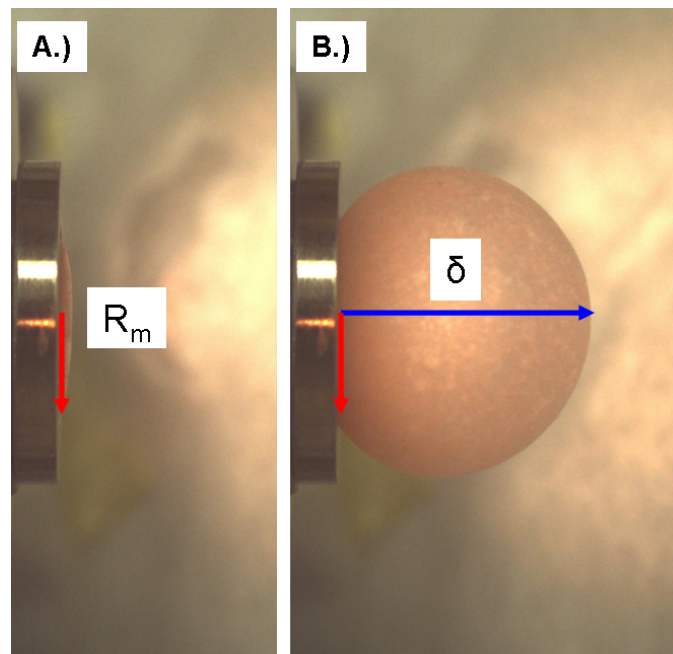
Figure 3.3. Example of membrane inflation.

3.7 and 3.8. True strain is presented because such strains are equivalent in tensile and compressive deformations (with opposite sign), additive, and three normal strain sums to the volume strain [46]. Overall, true strain most accurately describes the strain state but engineering strain and extension (λ) are often utilized for modeling or ease of measurement. Different analyses will be presented which depend on each strain form in Chapter 6.

$$\varepsilon = \frac{A_m}{A_o} - 1 = \overline{\delta}^2 \tag{3.7}$$

$$\varepsilon^T = ln\left(\frac{A_m}{A_o}\right) = ln\left(\overline{\delta}^2 + 1\right) \tag{3.8}$$

Membrane theory states that the true biaxial stress (σ_B^T) in a membrane is related to membrane tension (T) and thickness (h) via Equation 3.9. Tension (T) was calculated using the standard relation for a pressurized spherical vessel seen in Equation 3.10. Instantaneous film thickness

(h) was calculated assuming the membrane was an incompressible, constant-volume uniformly deforming material (Equation 3.11).

$$\sigma_B^T = \frac{T}{h} \tag{3.9}$$

$$P = \frac{2T}{R} = \frac{4\delta T}{\delta^2 + R_m^2} \tag{3.10}$$

$$h = \frac{V_o}{A_m} \quad , \quad where \; V_o = A_o * h_o \tag{3.11}$$

3.2.2.2. Ellipsometry. Neat polymer solutions were spin coated on silicon wafers at the same conditions utilized for membrane preparation (2,000 rpm, 30 seconds). Resulting membranes were analyzed in an ellipsometer with a 65-75 degree light incident angle sweep at 5 degree increments with 100 analyzer cycles per measurement. Light intensity is recorded and membrane thickness is measured by modeling each membrane as a Cauchy material. A Cauchy material allows thickness and refractive indices (n,diffraction index) and (k,absorption) variance until a model fit for light intensity is obtained. Most samples were analyzed for multiple membranes and had thicknesses between 1-3μm.

3.2.3. Shear Rheology

The linear viscoelastic properties of neat poly(vinyl acetate), polyisobutylene, and bubblegum bases were acquired from small strain rheological measurements on a Rheometric Scientific ARES rheometer. Tests were performed in oscillatory shear using a 25 millimeter parallel plate geometry. Neat polymers were compression molded at 120 °C ($\sim$gum base mixer) into discs of 10 - 30 mm diameter and 1 - 2.5 mm thick. Final sample dimensions depended on initial pellet size. Each material was loaded and trimmed to gap distances of 0.5 - 2 millimeters at $\sim$110 °C and equilibrated for 15 minutes at test temperature (37 - 110 °C depending on test). A strain

sweep was applied after temperature equilibration at 10 radians/second for identification of the linear viscoelastic regime. Dynamic measurements from 100 - 0.10 radians/second were performed for the acquisition of the storage modulus (G'), the loss modulus (G"), and consequently complex viscosity $(\eta^*) = \sqrt{(G'/\omega)^2 + (G'/\omega)^2}$.

The linear viscoelastic properties of commercial and experimental bubblegums were acquired from small strain rheological measurements on an Anton-Paar MCR 300 rheometer. Tests were performed in oscillatory shear using a 25 millimeter diameter parallel-plate fixture, a humidity jacket, and a temperature of 37 °C. The humidity jacket and temperature help simulate the mouth environment. Furthermore, the humidity jacket and small gap distance ($\sim$1 millimeter) reduce edge drying effects [5]. Samples were either mouth or finger chewed, hand kneaded in a water bath (at 37 °C), for 10 minutes before loading. Preliminary studies involved mouth chewing for other periods of time to understand chewing's effect on dynamic properties. Temperature equilibration time was $\sim$5 minutes before performing strain (at 10 radians/second) and frequency sweeps on each material. Dyamic measurements from 628 - 0.10 radians/second were performed for the acquisition of the storage modulus (G'), the loss modulus (G"), and consequently complex viscosity (η^*)

3.2.4. Differential Scanning Calorimetry

The glass transition temperature of unimodal and bimodal PVAc molecular weight distributions were measured by differential scanning calorimetry (DSC) using a Mettle-Toledo DSC 822 E. A constant rate of heating and cooling was maintained at 10 °C per minute. Approximately 5-10 milligrams of sample were used for each run and a thermal sweep was performed for the normalization of each sample's thermal history. Glass transitions were determined during

cooling by the midpoint of a line tangent to the transition and its intersection with lines tangent to the initial and final heat capacities [94].

3.2.5. In-vivo Bubble Inflation Testing

In-vivo bubble inflation testing was performed on commerical / laboratory controls and bubblegum prototypes to quantify the effects of molecular architecture on in-vivo bubble diameter. A preliminary study in the Spring of 2006 involved 70 undergraduate freshmen from Northwestern University's Engineering Design and Communication (EDC) course. This study helped develop the procedure and collected a large data set representative of the population for which prototype bubblegums would be designed.

During testing, each bubblegum is coded with a number as part of a double-blind experiment. Participants chew a 7.00 ± 0.02 gram piece of bubblegum for 10 minutes while practicing blowing large bubbles. Bubbles are then inflated in front of a CCD video camera with a ruler in the background in the subsequent 2 min. Participants then wait $\sim$20 minutes before starting to chew the next bubblegum. In this time, participants are given water and/or crackers to help cleanse their pallet and time to relax their jaw. An example bubble diameter measurement is shown in Figure 3.4.

3.2.6. Optical Microscopy

A Nikon OPTIPHOT 2 polarizing optical microscope was used in transmission mode to image the gum phases as presented in Chapter 2. Poly(vinyl acetate) is stained with iodine gas and imaged with this microscope. Micrographs have been collected for measurement of talc particle size and phase distribution.
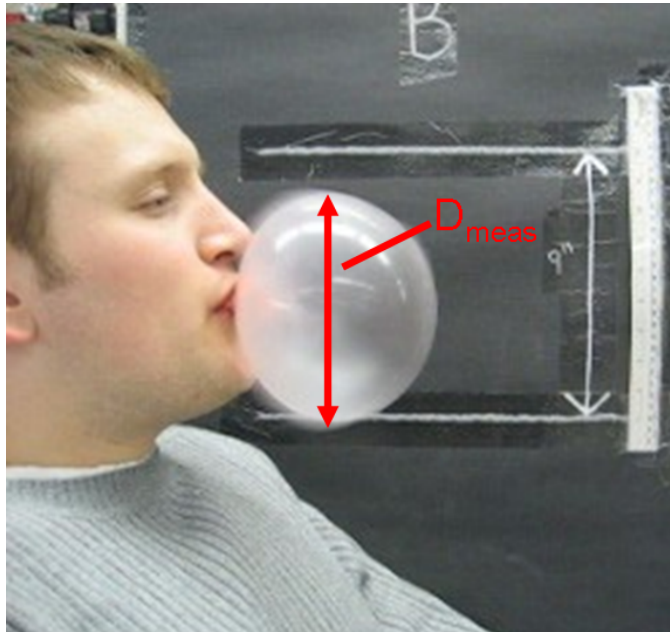
Figure 3.4. Example in-vivo bubble diameter measurement.

CHAPTER 4

Parametric Modeling of Molecular Weight Distribution Effects in Polyethylene Film Blowing

A simple parametric model relating bimodal molecular weight ratio (MWR) and high molecular weight (HMW) fraction to optimal equivalent film thickness reduction was developed for bimodal high density polyethylene (HDPE) blown films. Equivalent thickness reduction (ETR) was used as a measure of the true strain of biaxially inflated HDPE. The model predicts greatest thickness reduction at a MWR of ~ 7 and HMW fraction of ~ 20 wt%. Important film blowing parameters are outlined and model development is demonstrated.

4.1. Process Background

The polyethylene (PE) film blowing process is similar to gum bubble inflation in that both are describable as "biaxial elongational, nonisothermal" flows [95, 96]. In fact, both materials are inflated from a viscous state with a pressure gradient (ΔP) into a lower temperature environment (37 °C to 22 °C for gum and ~ 200 °C to 25 °C for PE). Pressure and temperature processability are similarly optmized for both systems in that pressure required for inflation is usually minimized while pre-extrusion material temperature is set to satisfy viscosity constraints. Most importantly, the overall goal for both processes is the achievement of large biaxial deformations, for PE large biaxial deformations reduce costs [97] and for gum bubbles large biaxial deformations lead to greater customer satisfaction.

Overall, the PE film blowing process can be depicted as shown in Figure 4.1. Here, a PE melt (180-210 °C) extrudes from an annular die (die gap = H_o) at an initial radius and velocity of R_o and V_o. Extruded material is subjected to a pressure gradient which biaxially inflates the extrudate to a final radius (R), once inflated, cooled film is continuously drawn by nip rolls at a final velocity of V_f. Cooling air ($\sim$10-60 °C) flows outside the annular film ring freezing in the film's molecular orientation at a distance between Z and L above the extruder die also known as the "freeze" line height (FLH). No further biaxial evolution occurs after this height.
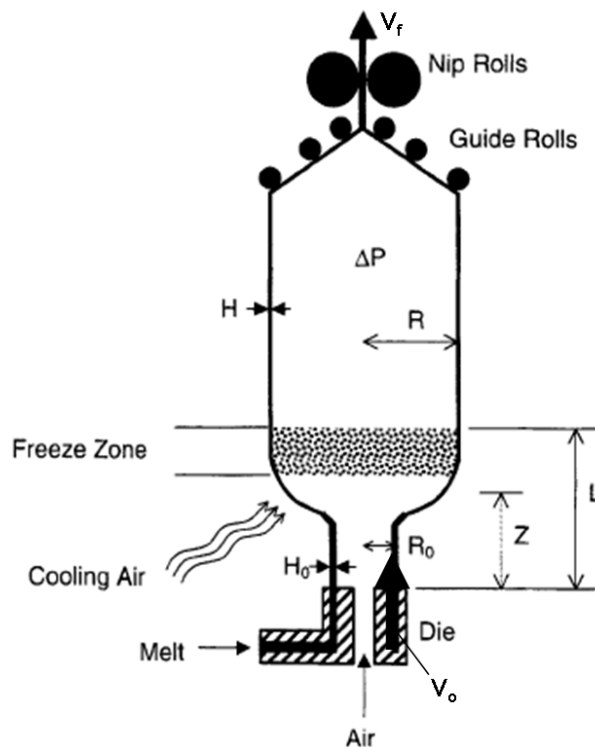
Figure 4.1. PE film blowing schematic [98].

The PE film blowing industry achieves large thickness reductions because they have mastered the advantageous utilization of controlled strain hardening for plastic flow stabilization.

Such stabilization is required because processing conditions often induce instabilities such as film thickness variations, bubble diameter pulsations, and helical bubble motion [20]. In 1977, Han and Shetty first realized process stability could be increased by increasing the elongational viscosity of the PE melt [6]. Since then, PE molecular architectures which have the ability to increase their elongational viscosity *during* flow, i.e. strain harden, have been extensively studied to understand their effect on inflation stability and film homogeneity [14–16, 18, 20, 24, 25, 27–29, 57, 58].

4.2. Model Development

4.2.1. Selecting PE Molecular Architectures

Molecular architectures for high density polyethylene (HDPE, $\rho = 0.94 - 0.96 g/cm^3$) and low density polyethylene (LDPE, $\rho \approx 0.92 g/cm^3$), the most thoroughly studied polyethylenes, are shown in Figure 4.2 [99]. Unimodal HDPE is stabilized for improved film blowing performance by broadening its MWD with a distinctively higher molecular weight HDPE spiked into it while LDPE has inherent film blowing stabilization because of an already broadened MWD resulting from its long chain branching. Both approaches induce bimodality which lengthens material relaxation time and increases strain hardening by increasing entanglement during flow induced molecular alignment but only HDPE was used as a model molecular architecture for this work for its greater potential for transferability of concepts to PVAc.

The high density PE data is especially relevant here because its thermoplastic character and overall linear structure are analagous to that of PVAc grades available for use in gum base. Neat PVAc has a greater hydrogen bonding character than HDPE and thus stronger adjacent chain interactions but this difference is minimized for PVAc in gum base because it exists in a

high density polyethylene
(HDPE)

low density polyethylene
(LDPE)
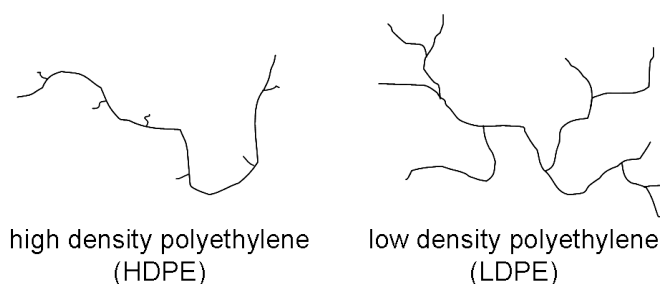
Figure 4.2. Typical HDPE and LDPE molecular architectures.

plasticized state. Additionally, PVAc and HDPE are amorphous and semi-crystalline polymers at low temperature, respectively, but this difference is of little importance because HDPE deforms as an amorphous melt until quenched at the FLH. This means that HDPE blown films are highly dependent on strain hardening plastic flow stability before quenching which are the exact flows we wish to design into gums for maximum bubble diameter. Analagous to the LDPE, a block copolymer, poly(vinyl acetate/vinyl laurate), with small chain branching was also briefly studied as an alternative gum base and will be discussed more in Chapter 6.

4.2.2. PVAc Proof of Principle

As shown in Figure 4.3, the same bimodal HDPE polymer physics which results in optimal strain hardening from molecular alignment caused entanglement are observable and shown to be beneficial in neat PVAc. As some irreproducibility was seen in the data, the plotted curves are those which achieved the greatest biaxial true strain therefore representing membranes having minimal initial defects. Different flow rates were utilized in an effort to match unimodal and bimodal PVAc low strain behavior for the constraint of material viscosity so that large strain behavior is likely a result of molecular architecture and not material viscosity. Bimodal PVAc

is shown to have greater strain hardening than unimodal PVAc (k = 1.25 vs 1.05) which leads

to upward $\sigma_B^T - \varepsilon_B^T$ curvature, better stability, and greater biaxial true strains.
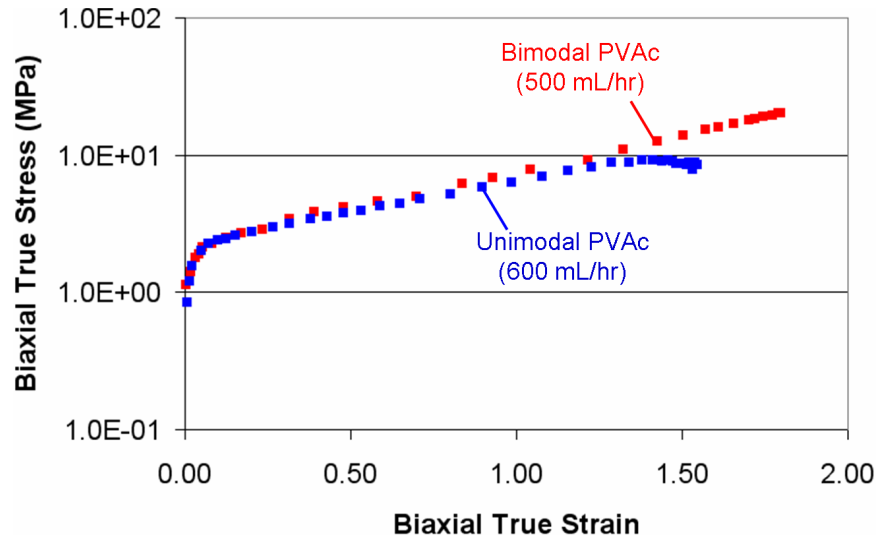
Figure 4.3. Comparison of unimodal (50 kg/mol) and bimodal (20/80 380/50 kg/mol) neat PVAc constitutive biaxial flow behavior at ~22 °C.

4.2.3. HDPE "Data Mining"

Understanding the effect of process variables on final film thickness (gauge) was important for

the acquisition of data during model development. In the simplest case, equivalent thickness

reduction (ETR) was calculated directly from final film thickness (H) and initial die gap width

(H_o) as shown in Equation 4.1. These values are not always reported, requiring thickness re-

duction (TR) calculation from the blow-up ratio (BUR) and take-up ratio (TUR) as shown in

Equation 4.2. For this, BUR was calculated from the initial (R_o) and final (R) bubble radius

(Equation 4.3) while TUR is calculated from the initial (V_o) and final (V_f) material velocities

(Equation 4.4). The BUR and TUR affect final film thickness because they correspond to bi-

axial and uniaxial process deformations, respectively, caused by initial melt inflation which is

followed by uniaxial mechanical acceleration.

$$ETR = ln(TR) = ln\left(\frac{H}{H_o}\right) \tag{4.1}$$

$$TR = \frac{1}{BUR * DDR} \tag{4.2}$$

$$BUR = \frac{R}{R_o} \tag{4.3}$$

$$TUR = \frac{V_f}{V_o} \tag{4.4}$$

HDPE melt thickness reduction data were parametrically correlated to the molecular weight ratio (MWR) and high molecular weight (HMW) fraction of their corresponding bimodal molecular weight distribution (MWD) using the graphical deconvolution method illustrated in Figure 4.4. Software applications FindGraph^{TM} and Image J^{TM} were employed for data acquisition and were used to measure the molecular weight and the area under MWD curves, respectively. The molecular weight ratio was calculated directly from measurement of high molecular weight (HMW) and low molecular weight (LMW). The areas under each MWD curve (A_{HMW} and A_{LMW}) were measured assuming them to be symmetric, and overlapping areas were divided proportionally between the two peaks. Weight fractions were then calculated by dividing the symmetrically measured area by the total area (A_{Total}) underneath the MWD [99, 100].

4.3. Parametric Model

The accumulated data was plotted with a semi log y-axis and is shown in Figure 4.5. Optimal equivalent thickness reductions are seen to monotonically increase from the upper-right to the lower-left corner of the HDPE film blowing operation region, suggesting optimal biaxial flow strain hardening and thus ductility at a MWR of ∼7 and a HMW fraction of ∼20 wt%. This
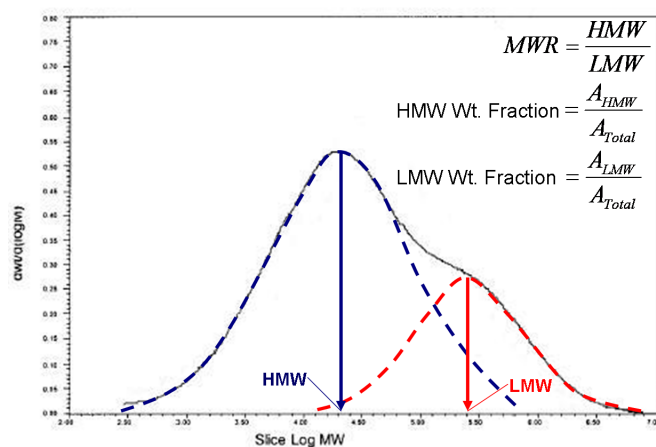
Figure 4.4. MWD deconvolution method used to for data collection from literature [101].

guidance provided a direction for the design of the bimodal PVAc gum base component of the third generation of gum prototype.

It is important to note other characteristics of the parametric model as they have implications to the design of future bubblegums. First, the model demonstrates decreased ductility at high MWRs and high HMW fractions which is effectively a graphical illustration of the scientific fact that *too much strain hardening is detrimental to ductility*. When bimodal polymers have high MWRs or high HMW fractions, their plastic flows are dominated by the HMW portion of the polymer which results in an activation of stress-controlled failure mechanisms. Thus, stable ideal plastic flow occurs when a bimodal blend is made with cooperative properties where the LMW portion largely controls viscosity while the HMW portion largely controls strain hardening.

Finally, the graphical model shows a lack of patent coverage existing for the explored PVAc design space [104–106]. Thus, prototypes designed in and around this box warrant even
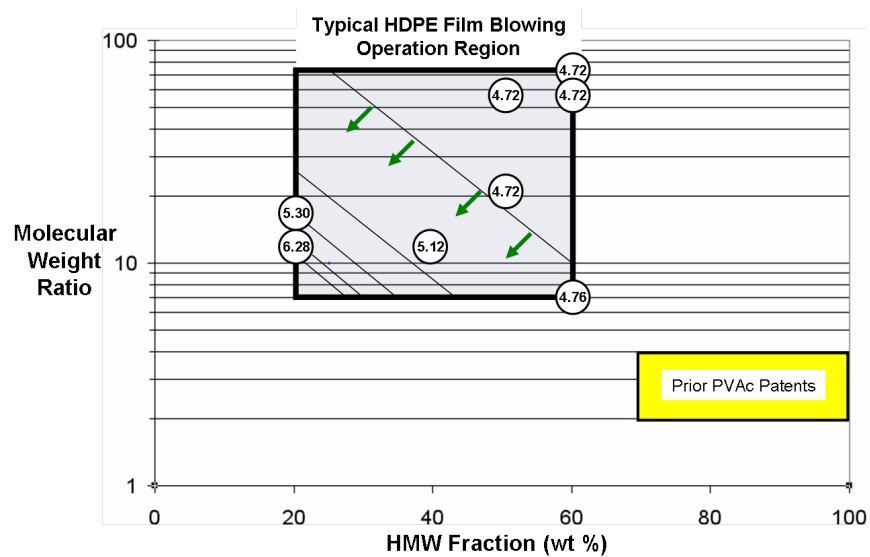
Figure 4.5. Typical MWR and HMW fraction parameterized HDPE film blowing operation region with overlayed optimal equivalent thickness reduction contours [58, 102, 103].

stronger consideration because they have a good chance at becoming patentable intellectual property.

CHAPTER 5

Modeling Gum Base Composition Effects on Chew Viscosity

As stated in Chapter 1, a secondary but equally important objective for this research is the application of a chew viscosity constraint to designed bubblegums. Such a constraint is of importance because it insures consumer satisfaction and ensures prototype design bubble diameter increases are a result of the parametric design of the PVAc MWD and not erroneous high gum viscosity effects, which can also lead to larger bubble diameters. Chew viscosity was characterized using oscillatory shear rheometry. This technique effectively quantifies differences in bubblegum complex viscosity (η^*, Pa*sec) resulting from gum base PVAc molecular weight, PVAc molecular weight distribution (MWD), talc ($Mg_3Si_4O_{10}(OH)_2$), and triacetin ($C_9H_{14}O_6$) compositional variations. A good correlation between complex viscosity and human-perceived chewability confirms the use of complex viscosity as a chew viscosity analog. Local and global solid solution-based empirical models were developed to describe viscosity behavior for application as a design constraint.

5.1. Shear Rheological Characterization of Bubblegum

Oscillatory strain sweeps at 10 rad/sec and 37 °C reveal a small linear viscoelastic range between 0.01 and ~2.0 % strain, with the upper limit of that range tending to decrease with increasing gum viscosity. Preliminary strain sweeps on high viscosity gums displayed radical departures from linear viscoelasticity, indicating sample disadhesion from the parallel-plate

fixture. Disadhesion was prevented in further studies by terminating strain sweeps as soon as non-linear behavior became apparent.

Typical linear viscoelastic behavior for the HBSS laboratory control bubblegum after mastication is shown in Figure 5.1. Properties such as storage (G', Pa) and loss (G", Pa) modulus, and consequently η^*, obey a strong power-law dependence on angular frequency (ω, rad/sec). Additionally, G' and G" are shown to increase proportionally to each other displaying the same dependence with very few discrepancies in magnitude. Subsequently, the damping factore ($tan\delta = G''/G'$) varies only slight from unity if at all and is not an adequate predictor of elastic character, especially in extensional flows which are primarily non-linear in nature. This behavior is indicative of the material having essentially infinite relaxation modes across all time scales [5]. Such behavior is qualitatively expected considering gum has a complex microstructure of plasticized and compatibilized phases, each with their own contribution to material relaxation. In the end, it has been shown that the power-law dependence of masticated gum is very robust with only the overall property and power magnitude varying.

A complex viscosity of 660 Pa*sec is marked in Figure 5.1 illustrating the exact viscosity constraint imposed on prototype gums. The next section will address the reason for the viscosity specification at a high angular frequency of 628 rad/sec while model predictions and prototype results will be discussed near the end of this chapter.

5.1.1. Time Dependent Linear Viscoelastic Behavior

As mentioned in Chapter 2, water soluble components are lost from gum as they dissolve in saliva during mastication. Figure 5.2 shows this resulting in a sharp decrease in complex viscosity (<1 min) followed by a somewhat less sharp increase (1-5 min) to a plateau value of
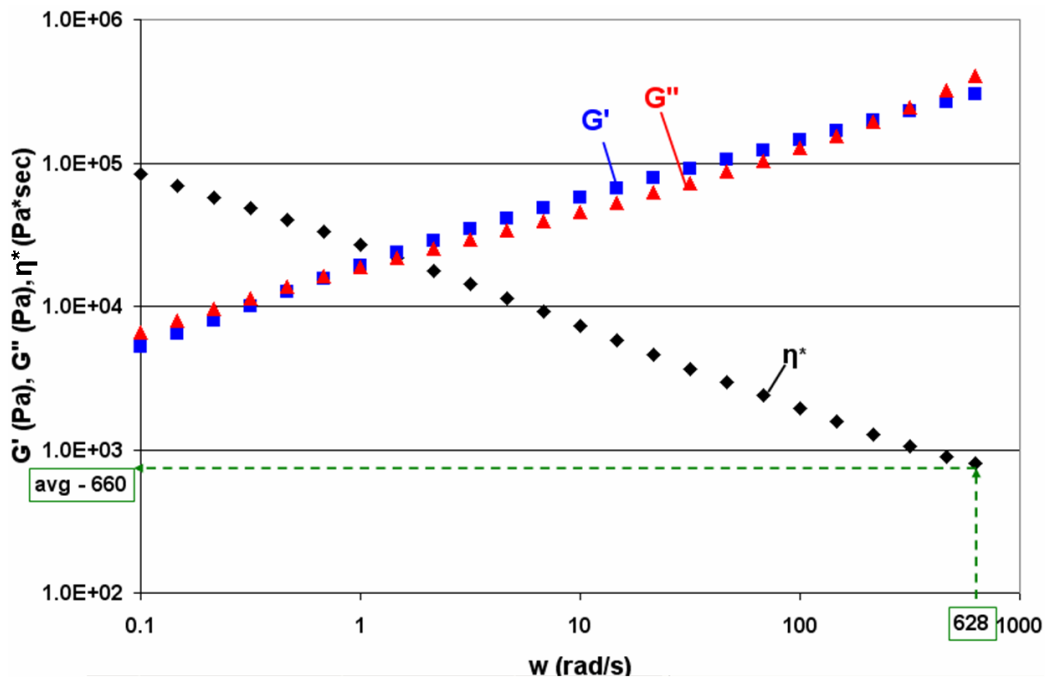
Figure 5.1. Masticated HBSS dynamic linear viscoelastic behavior at 37 °C.

~1,450 Pa*sec (5-30 min). This figure illustrates viscosity as being infinite at a zero chew time because the initial bite into the bubblegum chunk is essentially infinitely viscous, compared to the viscosity of the bubblegum at long chew times. The region of interest for the "chew viscosity" model is the time after 5 min because this is when gum properties are most influenced by gum base microstructural composition. A chew time of 10 min was chosen for characterization of gum viscosity and extensional inflation properties to ensure that characterization occurs far enough into this essentially constant viscosity regime (5-30 min).

A finger chew procedure was used to pseudo-masticate gums for complex viscosity characterization. As per Figure 5.3, typical complex viscosity behaviors for 10 min mouth and finger chewed gums show decreasing differences in complex viscosity to an optimal comparison at angular frequencies greater than 10 rad/sec (differing by ~11%). Since this region of
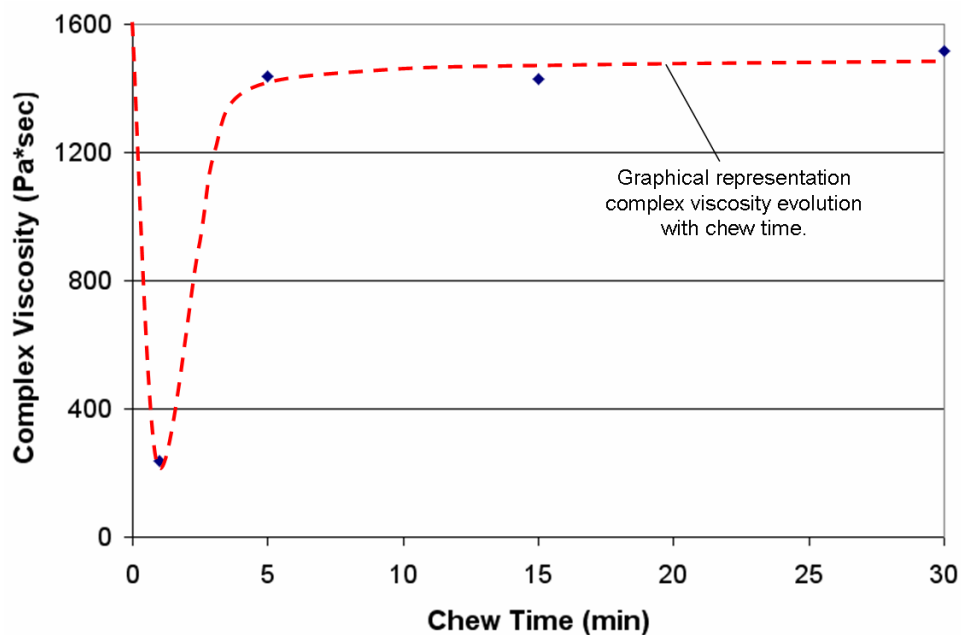
Figure 5.2. Bubblegum complex viscosity η^* chew time dependence (37 °C, 100 rad/sec).

optimal comparison shifts to higher angular frequencies with increasing gum viscosity it was important to measure data for model development at the highest possible angular frequency because these were least prone to procedural artifacts. Furthermore, the control was shown to vary across different batches by $\sim$17% at the highest achievable angular frequency on the Anton-Paar MCR 300 rheometer (628 rad/sec), a greater difference than what was observed between mouth chewed and finger chewed experimental gums, suggesting that the procedure was sufficient within the error that can be assigned to gum base and gum batch production.
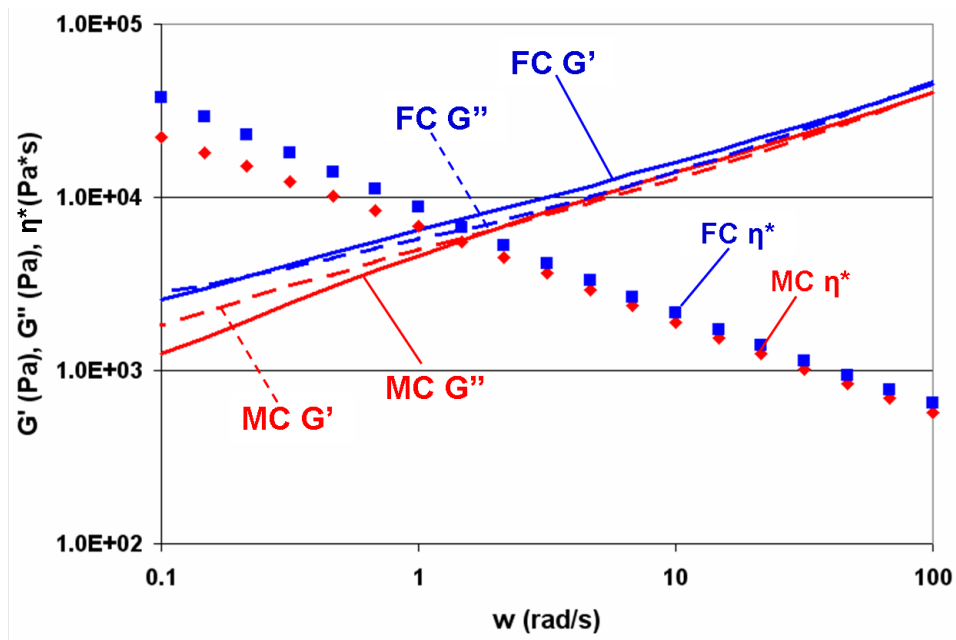
Figure 5.3. Comparison of 10 min mouth chewed (MC'd) and finger chewed (FC'd) gum linear viscoelastic behavior (37 °C).

5.2. Chew Viscosity Model Development

An empirical complex viscosity solution model was developed to constrain bubblegum designs to acceptable chew viscosities while exploring parameterized molecular architectural effects on the strain hardening of bimodal gum base. This model describes the compositional dependence of bubblegum complex viscosity on gum base PVAc molecular weight, PVAc molecular weight distribution, triacetin ($C_9H_{14}O_6$), and talc ($Mg_3Si_4O_{10}(OH)_2$) at 37 °C and an angular frequency of 628 rad/sec for predictive design of bubblegum prototypes. Although it is true that solution models are normally used to describe thermodynamic behaviors, they are "phenomenological in nature" and especially effective at describing multi-component systems [107].

5.2.1. Chew Acceptability

Feedback was collected from bubble blowing subjects during preliminary inflation studies in the Spring of 2005 and Summer of 2006 which allowed for the construction of the complex viscosity region (η^*) of chew acceptability seen in Figure 5.4. Unacceptable gums were often characterized as "oystery" or "tirey" by human subjects leading to the labels employed in the figure. These perceptions were mapped into the complex viscosity domain through the rheological characterization of these gums. Interestingly, the ends of the domain are capped by the complex viscosities of the two commercial gums of interest, Hubba Bubba^{TM} Seriously Strawberry ($\sim$660 +/- 80 Pa*sec) and Hubba Bubba Max^{TM} (360 +/- 200 Pa*sec). Designed prototypes were therefore designed to a viscosity the viscosity of the control, 660 Pa*sec, so as to eliminate cross-formulation viscosity effects on strain hardening for prototype proof of concept.

5.2.2. Local Chew Viscosity Model

This chewability model is termed "local" because its fitting parameters were developed for each molecular weight ratio pair (15/380, 40/380, and 50/380 kg/mol) in bimodal PVAc gum base independently from the others. This allowed the parameters to most effectively describe the potentially complex mixing behavior of each bimodal PVAc gum base and prevent errors arising from MWD differences in the LMW (15, 40, and 50 kg/mol) polymers used in each formulation.

A series of two sublattice solution models are proposed for the constraint of chew viscosity in bimodal prototype gums. A site occupation sublattice representation is shown in Equation 5.1. In this representation, PVAc molecular weights A (15, 40, and 50 kg/mol) and 380 kg/mol
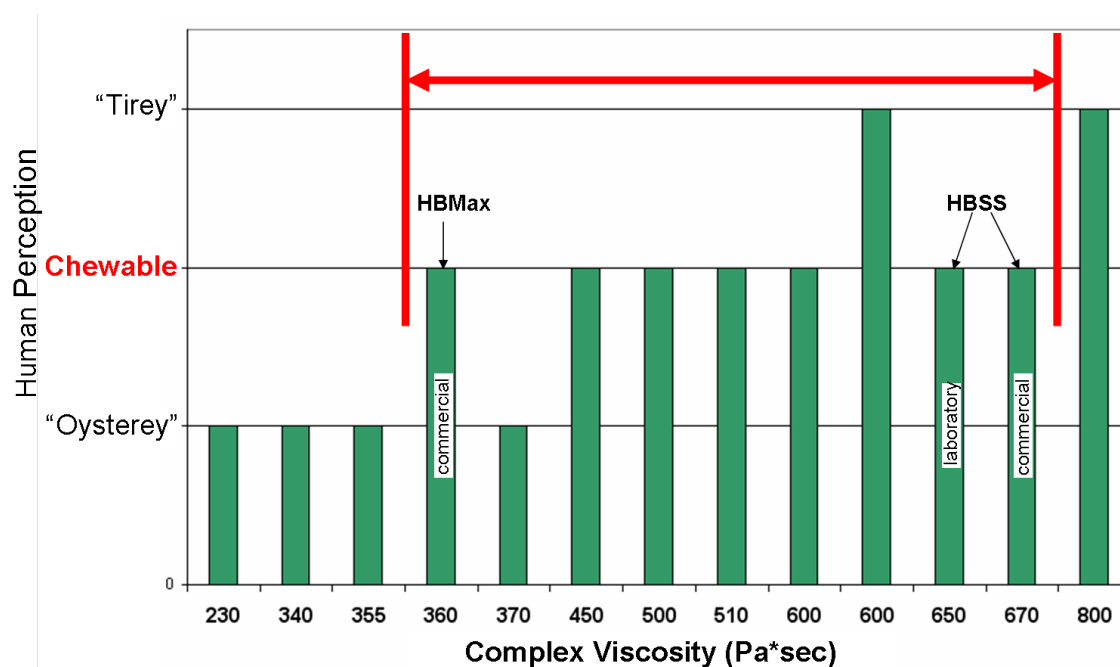
Figure 5.4. Acceptable chewability plot comparing human perception to complex viscosity (37 °C, 628 rad/sec).

(HMW addition for broadening of unimodal MWD to a bimodal MWD) are compositionally varied on the first sublattice of each independent local model while triacetin (*Tr*), talc (*Ta*), and vacancies (*Va*) are compositionally varied on the second. Sublattices were used to treat molecular weight as a substitutional phase while treating triacetin, talc, and vacancies as interstitial phases. This allowed for variance of PVAc molecular weight across its entire range of gum base weight fraction on the first sublattice and triacetin and talc to be modeled far from their "reference" states on the second. By doing so, component fractions were constrained to regions of interest without describing unuseful compositions. Furthermore, the two sublattice model affords description of internal substructure while helping define stoichiometric gum base relationships of interest, together helping to describe specific complex viscosity behaviors that

might otherwise go unnoticed.

$$(A, 380) \, (Tr, Ta, Va) \tag{5.1}$$

Compositions in this work are described with respect to weight fraction in accordance with standard industry practice. Equations 5.2 and 5.3 illustrate the compositional interdependence *within* each sublattice (denoted by superscripts) and independence *between* each sublattice. This is the mathematical manifestation allowing the first sublattice to be treated as substitutional (y_i^I = 0 to 1) and the second sublattice as interstitial (y_{Tr}^{II} =0 - 0.26 and y_{Ta}^{II} =0 - 0.74). The physical significance of the range of weight fractions relates to the amount of each of these components in the control gum base formula. A gum with $y_{380}^I = 1$ and $y_{Tr}^{II} = 1$ suggests that all PVAc ($\sim 40\%$) in the gum base has a 380 kg/mol molecular weight and that the amount of triacetin equals its normal weight plus the normal weight of talc ($\sim 25\%$ of base). Finally, a vacancy term was included for modeling the behavior of the second sublattice when triacetin or talc were present in a lower amount than in the control gum base. Ultimately, the vacancy term helps in understanding the effect of the gum base components being held constant (PIB, wood rosin, fats and oils, etc.).

$$\sum_i y_i^I = y_A^I + y_{380}^I = 1 \tag{5.2}$$

$$\sum_j y_j^{II} = y_{Tr}^{II} + y_{Ta}^{II} + y_{Va}^{II} = 1 \tag{5.3}$$

In general, the complex viscosity (η^*) of gum can be described by Equation 5.4. This equation represents complex viscosity having ideal and non-ideal contributions denoted η^{*ref} and η^{*xs}, respectively. Ideal complex viscosity contributions are considered reference (*ref*) states where each sublattice is entirely filled by one component (example: $(y_{50}^I, y_{Ta}^{II}) = (1,1)$).

The excess (*xs*) term accounts for non-ideal component interactions which either positively or negatively deviate complex viscosity from the ideal mixing of reference states.

$$\eta^* = \eta^{*ref} + \eta^{*xs} \tag{5.4}$$

Ideal complex viscosity mixing was described as shown in Equation 5.5. This equation expands for each local chewability model pair into an equation of six reference states ($\eta_{i,j}^{*o}$) where i and j represent the two substitutional and three interstitial components, respectively.

$$\eta^{*ref} = \eta_{ideal}^{*ref} = \sum_{i,j} y_i^I y_j^{II} \eta_{i,j}^{*o} \tag{5.5}$$

As most multicomponent systems do not have composition-independent interactions that sufficiently describe the non-ideal mixing behavior, Redlich-Kister polynomials were applied to this system to describe composition-dependence [107, 108]. Non-ideal component interactions are accounted for by using binary interaction parameters ($L_{i:j}^{v*}$), where *i* or *j* are replaced by binary interactions i_1, i_2 or j_1, j_2 occurring on sublattices one or two, respectively. These interactions account for binary mixing effects on each sublattice and their affect on the whole is shown in Equation 5.7. The first half of the equation accounts for interstitial interactions (j_1, j_2) with a filled first sublattice while the second half accounts binary PVAc molecular weight interactions resulting from the bimodal broadening of the gum base MWD with a filled interstitial sublattice. Binary interactions terms are the highest order interactions described in this work because they sufficiently describe the non-ideal behavior of most material systems [107]. It should be noted that in Equation 5.7 the $v*$ superscript is meant as a descriptor for the order of

the binary interaction while v is an exponent with a physical value.

$$\eta_M^{*xs} = \eta_{nonideal}^{*xs}$$

$$= \sum_i \sum_{j_1} \sum_{j_2} y_i^I y_{j_1}^{II} y_{j_2}^{II} \sum_v L_{i:j_1,j_2}^{v*} \left((y_{j_1}^{II})^2 - (y_{j_2}^{II})^2\right)^v \quad (5.6)$$

$$+ \sum_{i_1} \sum_{i_2} \sum_j y_{i_1}^I y_{i_2}^I y_j^{II} \sum_v L_{i_1,i_2:j}^{v*} \left((y_{i_1}^I)^2 - (y_{i_2}^I)^2\right)^v$$

Equations 5.5 and 5.7 were combined in Equation 5.4 to model the complex viscosity of gums with varying gum base compositions. Model development gums were made at the compositional extremes, and binary interaction midpoints, and characterized using shear rheology. These measured values were used for the extrapolation of complex viscosity of gums having $y_{380}^I = 1$. Power-law fits like that seen in Figure 5.5 were used because of their effectiveness and historical use in describing the viscosity of polymers of all concentrations [5].
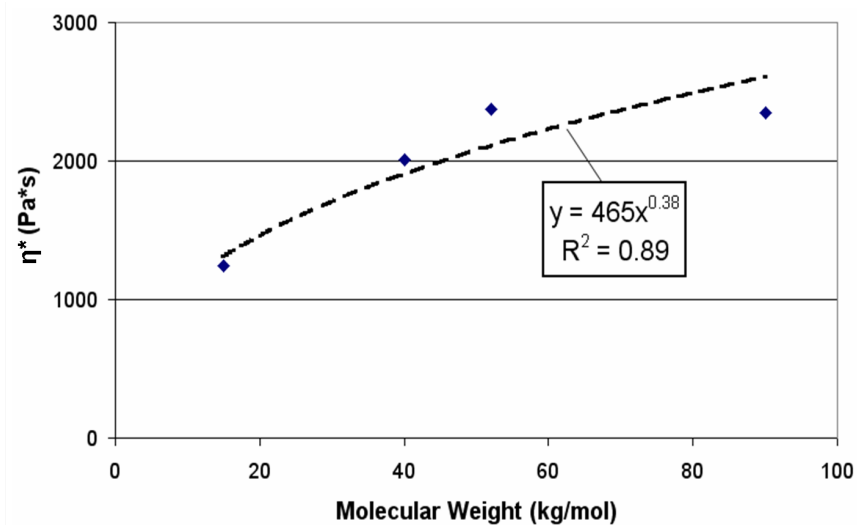
Figure 5.5. Example for the extrapolation of the complex viscosity for a $y_{380}^I = 1$, $y_{Tr}^{II} = 0$, $y_{Ta}^{II} = 0.74$ gum.

Microsoft® Excel's solver function was used to fit collected data by varying model end-points and binary interaction parameters for the minimization of the sum squared errors of the model ($SSE = \sum \left(\eta^{*}_{measured} - \eta^{*}_{model}\right)^2$). The resulting model parameters seen in Tables 5.1, 5.3, and 5.2 fit 90% of the data with an error of less than 5%. A more extensive analysis is described in the Model Validation section of this chapter.

Model endoint parameter ($\eta^{*ref}_{i,j} = \eta^{oref}_{i,j}$) values in Table 5.1 are all *effective* parameters except for those in column four ($\eta^{o*}_{i,Va}$). As explained previously, these reference states are compositions where each sublattice is completely filled. These parameters are treated as *effective* parameters because this model does not seek to describe all compositions, only those of interest. Thus, most of these parameters do not represent physical values but are useful for modeling the variance of complex viscosity without having to have collect data at extremes of little compositional interest. Additionally, multiple values for $\eta^{o*}_{380,Tr}$, $\eta^{o*}_{380,Ta}$, and $\eta^{o*}_{380,Va}$ are seen because they represent effective values for that specific *local* bimodal PVAc system. In general, the sign of each parameter is the same suggesting that no significant differences exist between described behaviors.

Table 5.1. Endpoints ($\eta^{*o}_{i,j}$, Pa*sec) for Redlich-Kister solution modeling of complex viscosity.

PVAc MW (kg/mol)	j		
i	Tr	Ta	Va
15	5,738	1,309	969
40	-1,558	1,700	1,725
52	-1,639	3,455	1,340
380 (15)	-3,333	5,576	3,404
380 (40)	-4,668	5,727	3,404
380 (52)	-3,525	8,488	3,404

The interstitial binary interaction parameters in Table 5.2 give insight into the interaction of components on each sublattice. For instance, large negative deviations from ideality are seen in column two, suggesting a triacetin/talc interaction in which their combined effect is drastically different than their independent interactions with the gum base. This may suggest a mechanism by which the plasticization of the gum base both softens the matrix and increases talc shearability. A synergistic interaction is proposed because neither triacetin nor talc have such effects by themselves on the gum base (as seen in the Va,Tr and Ta,Va interactions).

The substitutional binary interaction parameters shown in Table 5.3 indicate other interaction possibilities. For instance, gums with only triacetin on the second sublattice tend to positively deviate above ideal behavior indicating a stronger complex viscosity contribution by the 380 kg/mol PVAc. This is expected since viscosity often scales with a power-law dependence and higher MWs should quickly dominate a bimodal blend, assuming the two MWs are mixed well. More interestingy, HMW additions in the presence of talc show a negative deviation suggesting decreased HMW effects owing to the presence of talc. This might be an effect resulting from the easy cleavage of talc's basal planes resulting in more internal movement which overcomes the effects of HMW addition. Overall, gums with talc have been found to have a higher

Table 5.2. Interstitial binary interaction parameters ($L^{V*}_{i:j_1,j_2}$), Pa*sec) for modeling complex viscosity with Redlich-Kister polynomials.

Binary Order →	k = 0			k = 1		
$i \backslash j_1, j_2$	Ta,Tr	Va,Tr	Ta,Va	Ta,Tr	Va,Tr	Ta,Va
15	-9,522	-9,362	-118	0	-285	439
40	-8,804	2,603	803	0	-9,118	1,562
52	-7,799	2,158	-2,826	0	-6,017	280
380 (15)	-8,431	7,638	-5,453	1,650	-27,810	6,019
380 (40)	-6,678	9,928	-5,813	-1,378	-28,831	5,551
380 (52)	-8,637	7,965	-12,402	2,608	-27,953	-3,010

complex viscosity than those without, so this effect might be a synergistic one resulting because of the enhanced matrix viscosity from HMW PVAc addition. Vacancy effects are shown to be less apparent.

Chewability model results for talc-filled (15,380) and (50,380) bimodal PVAc gum bases are shown in Figures 5.6 and 5.7, respectively. All local models show similar trends and indicate similar endpoint comparisons (Equation 5.7). More glaringly, the 15,380 bimodal PVAc gum base displays (both in color and in red on the contour plot) a larger area of acceptable chewability compositions than the 52,380 bimodal PVAc gum base. This suggests a limitation in the ability to design a "chewable" gum in this system without an extrapolation of the local model to higher triacetin contents ($y_{Tr}^{II} > 0.26$).

$$\eta^*(y_{380}^I = 0; y_{Tr}^{II} = 0.26) \quad < \quad \eta^*(y_{380}^I = 0; y_{Tr}^{II} = 0) < \ldots$$

$$\eta^*(y_{380}^I = 1; y_{Tr}^{II} = 0.26) \quad < \quad \eta^*(y_{380}^I = 1; y_{Tr}^{II} = 0) \tag{5.7}$$

Table 5.3. Substitutional binary interaction parameters ($L_{i_1,i_2:j}^{V*}$), Pa*sec) for modeling complex viscosity with Redlich-Kister polynomials.

Binary Order $\rightarrow$	$k = 0$		
$i_1, i_2 \backslash j$	Tr	Ta	Va
15 , 380	3,266	-3,984	-1,297
40 , 380	8,994	-1,890	-3,317
52 , 380	1,141	-5,923	473
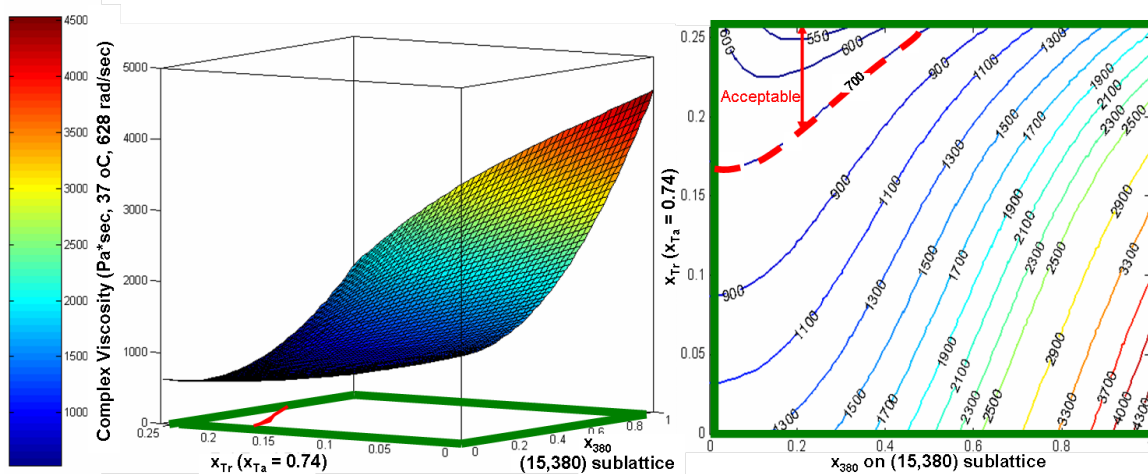
Figure 5.6. Complex viscosity (37 °C, 628 rad/sec) for (i_1, i_2)=(15,380) kg/mol bimodal PVAc gum base having x_{Ta}=0.74.
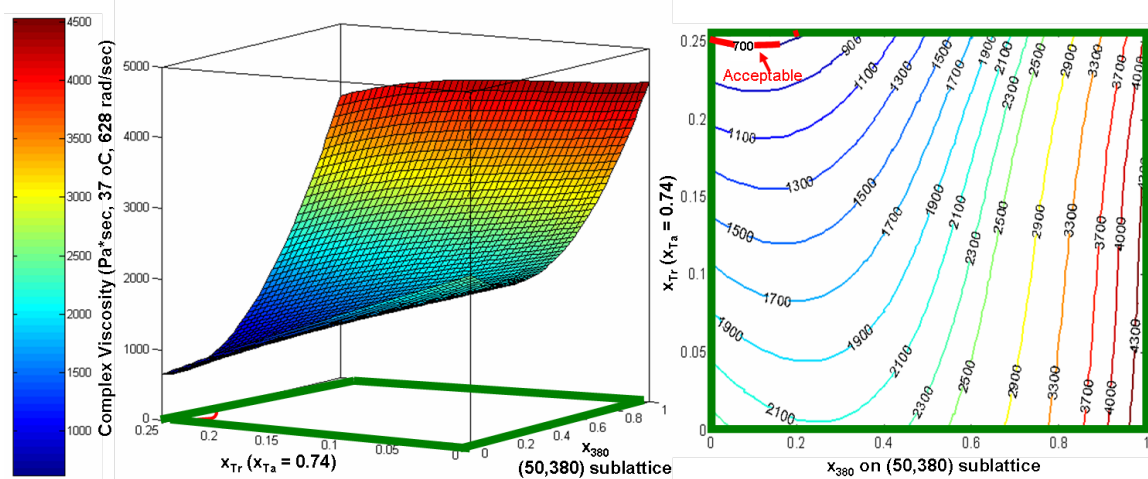
Figure 5.7. Complex viscosity (37 °C, 628 rad/sec) for (i_1, i_2)=(50,380) kg/mol bimodal PVAc gum base having x_{Ta}=0.74.

5.2.3. Global Chew Viscosity Model

A global chew viscosity model was developed for the purpose of creating a general molecular weight model for use in the development of gum with any molecular weight distribution, beyond just the pairs used in the local chewability models previously presented. The goal was to create

a subset of equations for use in the prediction of any endpoint or binary interaction parameter that may be needed for the constraint of chew viscosity in future gum designs.

The first step in the creation of this model was the unification of the three local models discussed above by constraining their model fits to the same 380 kg/mol endpoints and binary interaction parameters. The SSE of the unified model were re-minimized, and resulting endpoints and interaction parameters were plotted and fit with smooth functions in a manner similar to that seen in Figure 5.8. The top row of plots show each parameter plotted in order to find a general function for fitting. Then, the form of each function was held constant while its identifying parameters (pre-exponential factor, intercept, etc.) were varied to fit the function through the 15 kg/mol point in an effort to weight the function to the low MW end. Weighting was a necessity because high molecular weights are minimally used in gum design and thus their endpoints and interactions are of less importance to the calculation of complex viscosity with a Redlich-Kister solution model discussed above.
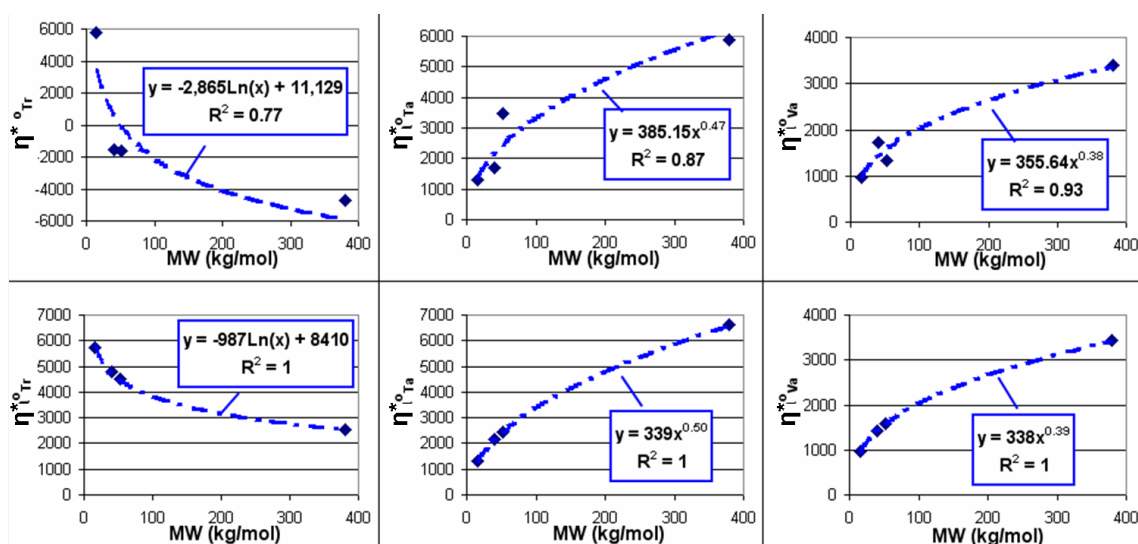
Figure 5.8. Endpoint (η_j^{*o}) smooth function fitting examples for global chewability model development.

The binary interaction parameters for the substitutional ($L^{v*}_{i_1,i_2:j}$) and interstitial ($L^{v*}_{i:j_1,j_2}$) sub-lattices are presented in Tables 5.4 and 5.5. As shown, most parameters can be calculated from simple linear equations where i represents MWs of 15, 40, 50, or 380 kg/mol. It should be noted that this model does a reasonable job modeling the experimental data from which it was developed. Of all the data being empirically fit, 95% of them are fit within 20% of their experimental value. For a little perspective on this, the acceptable chew viscosity range is between 350 and 700 Pa*sec. If a gum were designed to be at a gum viscosity of 525 Pa*sec, in the middle, then there would be a 175 Pa*sec or 33% leeway for model error. Thus, the model appears to fit the data well.

Finally, the global model has the potential to include equations for the prediction of other substitutional binary interactions such as those for a $i_1, i_2 = 15, 50$ kg/mol bimodal PVAc system. If those interactions were determined and included, then this global model could be used

Table 5.4. Global equations for the calculation of substitutional binary interaction parameters ($L^{v*}_{i_1,i_2:j}$) (Pa*sec) for modeling complex viscosity with Redlich-Kister polynomials.

j	$v* = 1$
Tr	$L^1_{i,380:Tr} = -115i + 8,940$
Ta	$L^1_{i,380:Ta} = 15i - 4,603$
Va	$L^1_{i,380:Va} = 68i - 3,925$

Table 5.5. Global equations for the calculation of interstitial binary interaction parameters ($L^{v*}_{i:j_1,j_2}$) (Pa*sec) for modeling complex viscosity with Redlich-Kister polynomials.

Interaction	$v*$	
j_1, j_2	1	2
Ta , Tr	$L^1_{i:Ta,Tr} = i - 11,844$	$L^2_{380:Ta,Tr} = -6,928$
Va , Tr	$L^1_{i:Va,Tr} = 19i - 9,542$	$L^2_{i:Va,Tr} = -64i + 864$
Ta , Va	$L^1_{i:Ta,Va} = -22i + 579$	$L^2_{i:Ta,Va} = 5i + 1,077$

for the calculation of any mixture of PVAc molecular weights and a very powerful tool for the design of a wide range of gum bases, both chewing and bubble.

5.3. Model Validation

5.3.1. Gum Base Shear Rheological Characterization

An inspection of Figure 5.9 reveals that the control gum base has a similar power-law linear viscoelastic properties to that of the control gums made from it, Figure 5.1, hence supporting the assumption that gum base compositional variations are reflected in their resulting gums during shear rheological characterization. Additionally, a comparison between control gum base and 10 minute finger masticated control gum base shows very little change ($\sim$10% on average) in its linear viscoelastic properties. Such behavior could mean that water, recall that saliva is 99% water [109], plays a small role in the actual plasticization of gum during mastication, the microstructure of gum itself is important to the water's plasticization of gum, or that gum's flavor components,not water, dominate masticative properties. Intuition suggests that the linear viscoelastic properties of bubblegum are dominated by a combination of (1) its structure, aiding water infiltration and (2) flavor components causing plasticization of the gum base.

A comparison of control gum base and 10 minute finger chewed control gum, in Figure 5.10, shows an $\sim$810% complex viscosity ($\eta*$) decrease (at 37 $^\circ$C) after finger mastication. Until now, gum and gum base linear viscoelastic behavior have only shown a power-law dependence when characterized in the angular frequency regime between 0.1 - 100 rad/sec, but this comparison reveals a shift in the relaxation of gum base to shorter times scales because of increased plasticization. This can be thought of in reference to time-temperature superposition. Increased plasticization increases polymer movement in the same manner as temperature
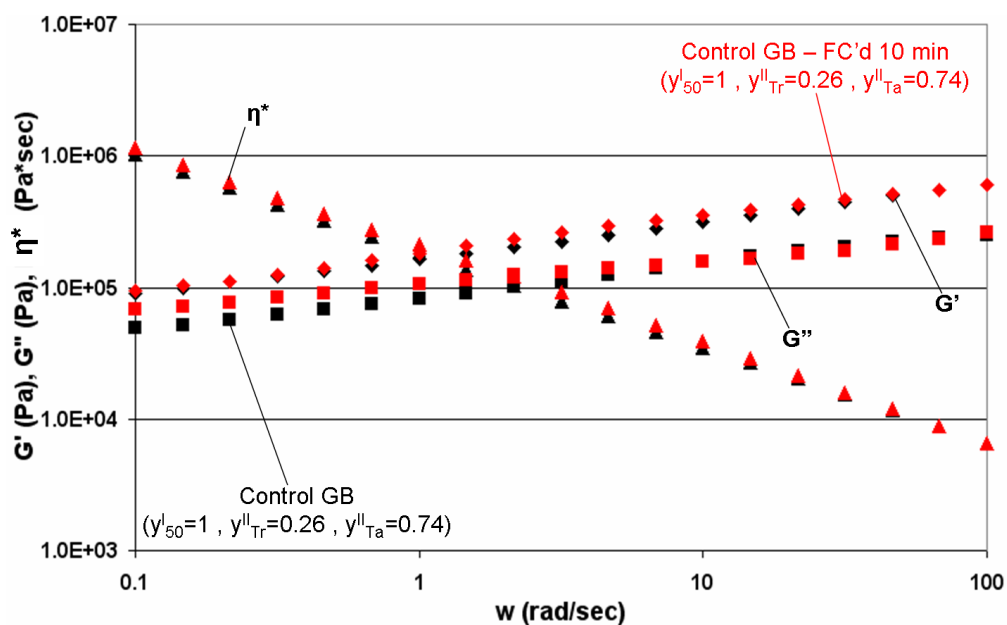
Figure 5.9. Oscillatory frequency sweep comparison of control gum base with and without a 10 min finger chew, at 37 °C.

increase does. Thus, increased plasticization of the control gum base results in its complex viscosity shifting to smaller angular frequencies and eventually overlapping with the gum curve. Another interesting observation is that of a possible G' vs G" crossover in the gum suggesting gum base represents the high frequency behavior and gum represents the low frequency behavior of the same concentrated polymer liquid material.

The linear viscoelastic behavior of P3B bimodal PVAc gum base is shown in Figure 5.11. The figure illustrates the same ~840% complex viscosity (η^*) decrease as shown for the control, indicating the same plasticization mechanisms at work for both gums. More interestingly, the bimodal PVAc gum base has the beginnings of a high angular frequency plateau, as seen by the G" curve. This plateau is thought to be a result of increased entanglements from the addition of high molecular weight PVAc in much the same manner as is normally attributed in concentrated
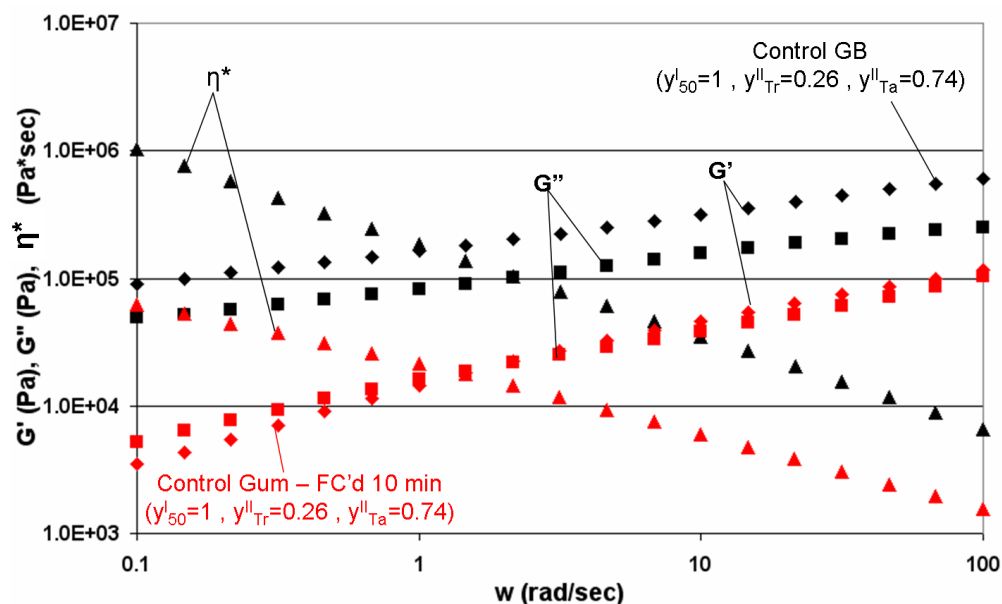
Figure 5.10. Oscillatory frequency sweep comparison of control gum base and 10 min finger chewed control gum at 37 °C.

polymer systems (see Appendix pure PVAc shear rheology). A mild plateau behavior is seen in Figure 5.10 for the control gum base but this behavior has been found to be reproducible for all bimodal PVAc gum bases studied. It should be noted that the same entanglement plateaus is not seen in the finger chewed gum because of increased plasticization resulting in a shift towards shortening material relaxation time as discussed above.

Ultimately, gum base was shown to characteristically determine the power-law dependence of resulting gums therefore validating the modeling of gum base for the establishment of a chew viscosity model to constrain prototype designs to acceptability chewability.
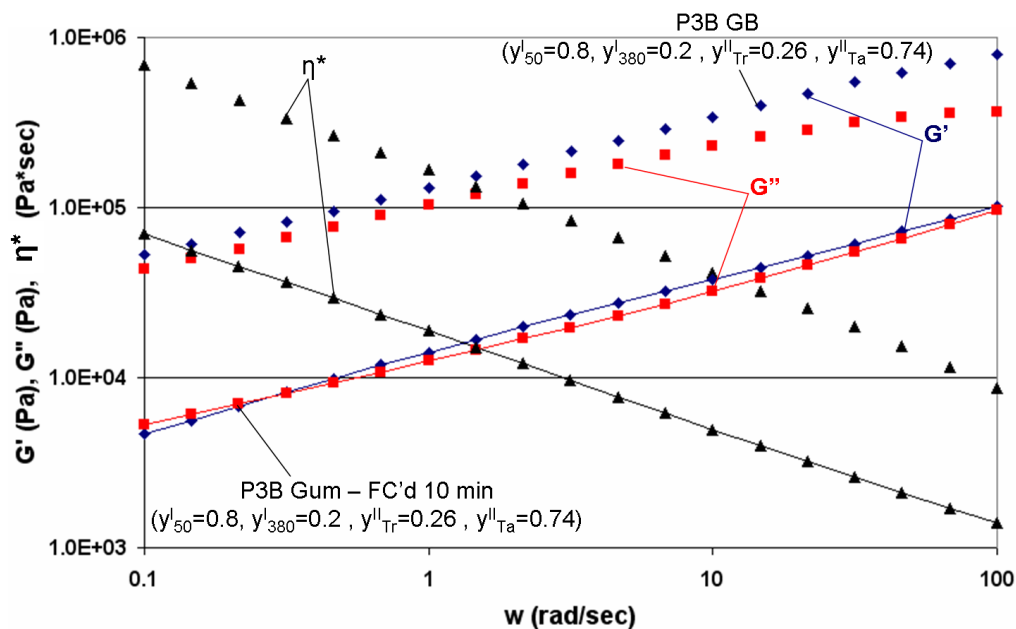
Figure 5.11. Oscillatory frequency sweep comparison of bimodal 20/80 380/50 kg/mol PVAc gum base (without connecting lines) and 10 min finger chewed gum (with connecting lines) at 37 °C.

5.3.2. Local Chewability Model Predictions *vs* Measurements

As mentioned above, the local chewability model was used to constrain gum complex viscosity to acceptable values for the exploration of novel bimodal PVAc gum bases for the design of a high performance bubblegum. Table 5.6 shows measured values for five third-generation proto- types and compares them to the average control complex viscosity (660 ± 80 Pa*sec) to which they were constrained. The error in this value represents one standard deviation of error and is $\sim$12% of the value. Therefore, third-generation prototypes were constrained within a standard deviation of the control, and thus the developed models sufficiently constrained the gum designs within the errors resulting from batch formulation, finger chew method, and instrumentation. The third-generation prototype will be discussed more in Chapter 7. For now, it is important to

know that the model sufficient constrained its chew viscosity and thus achieved bubble diameters are most likely a result of increased plastic flow stabilization due to strain hardening biaxial flows.

Table 5.6. Comparison of local chewability model predicted and measured complex viscosities for P3 bubblegums.

Prototype	y_i^I	y_j^I	y_{Tr}^{II}	y_{Ta}^{II}	η_{pred}^*, Pa*sec	η_{meas}^*, Pa*sec	Error,%
Control	y_{50}^I=1	y_{380}^I=0	0.26	0.74	660 ± 80	593	-10
P3A	y_{15}^I=0.8	y_{380}^I=0.2	0.2	0.74	660 ± 80	625	-5
P3B	y_{50}^I=0.8	y_{380}^I=0.2	0.26	0.74	660 ± 80	650	-2
P3-VAVL	y_{VAVL}^I=1	y_{50}^I=0	0.09	0.74	660 ± 80	680	3
P3*	y_{15}^I=0.6	y_{380}^I=0.4	0.26	0.74	660 ± 80	750	14

CHAPTER 6

Conceptual Designs

6.1. Conceptual Molecular Architectures for Flow Stability

As previously mentioned, polymer entanglements during molecular alignment stabilize plastic flow because of their unique ability to resist deformation by strain hardening. A central concept to this approach is that of the *cross-link*. There are two types of cross-links: physical and chemical. Physical cross-links are caused by external driving forces which physically confine polymer chains and tend to be temporary, while chemical cross-links are formed by covalent bonds linking adjacent polymer chains and are permanent [100]. Chemical cross-links are not ideal for this application because they are not easily tailorable for use in gum base and tend to restrict polymer flow and limit achievable strain. On the contrary, temporary physical cross-links evolve with deformation-induced molecular alignment and do not limit strain.

Molecular architectures which strain harden through physical cross-linking mechanism and have been studied in this work for the control of gum base are shown in Figure 6.1. Segregated domain physical cross-links were of interest because of their ability to offer tunable strain hardening. Polymer chain branching was also of interest because long chain branches like those in LDPE broaden the MWD, enhance entanglement, and increase physical cross-linking during flow more efficiently than broadened HDPE MWDs (Figure 6.1B). Finally, unimodal to bimodal MWD broading by spiking a linear polymer with one of distinctly higher MW was of interest because it has been shown to effectively stabilize HDPE film blown plastic flows (Figure 6.1C).

The architectures seen in Figures 6.1A and 6.1B are conceptually studied in this chapter while that in Figure 6.1C is extensively examined in Chapter 7.
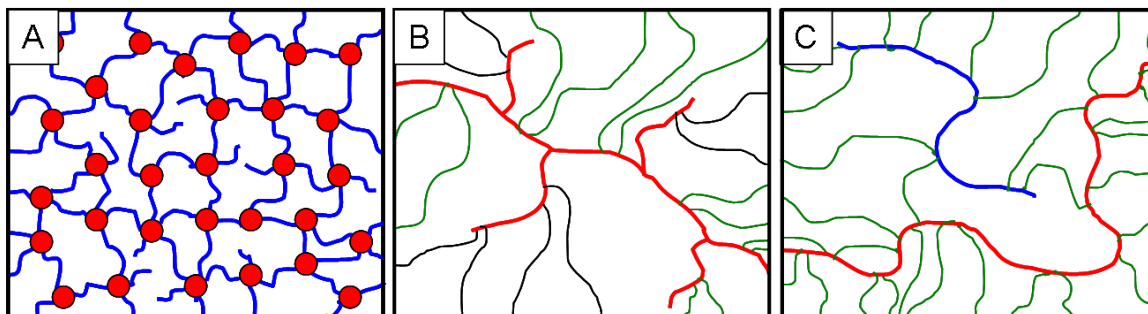
Figure 6.1. Physically cross-linked molecular architectures A.) Segregated domain, where triblock copolymer end-blocks associate (red circles) to physically cross-link elastomeric mid-block (blue lines) to which they are covalently attached B.) Chain branching, where branched structures entangled and physically cross-links during flow C.) Bimodal MWDs, such broad MWDs behave in a manner similar to branched structure through increased entanglement.

The first two architectures (Figure 6.1A and 6.1B) were studied using styrene-isoprene (SI) and vinyl acetate-vinyl laurate (VAVL) block copolymers. VAVL copolymer was the only on of the two systems that was implemented in gum base because SI copolymer availability was limited. Nonetheless, neat SI was still of conceptual interest because styrene and isoprene should be easily approvable by the Food and Drug Administration since their components are already in use as acceptable gum base ingredients in the form of styrene-butadiene rubber (SBR) and isobutylene-isoprene copolymer [110]. Therefore, a fundamental understanding of SI block copolymer and its potential application to gum base is still beneficial for potential future application.

6.2. Model Block Copolymers for Flow Stabilization

6.2.1. Styrene-Isoprene-Styrene/Styrene-Isoprene Blends

Neat styrene-isoprene-styrene/styrene-isoprene (SIS/SI) block copolymer blends were studied to better understand their nonlinear elastic behavior at large biaxial strains. Such blends are of interest in the gum industry because they show tunable strain hardening with and without tackification, see Figures 6.2A and 6.2B. Their tackified behavior is of interest to the gum industry because low MW, high T_g tackifiers such as Escorez 5380 are like glycerol ester gum rosins which are used for the compatibilization of gum base (see Figure 2.3), thus providing a qualitative analog to gum base behavior.
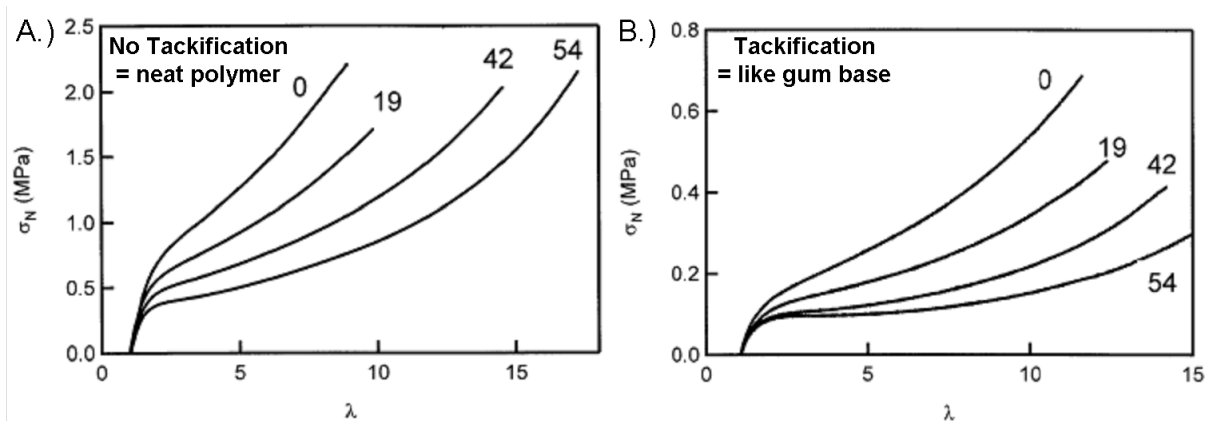
Figure 6.2. Nominal stress as a function of strain for tensile tests at 500 mm/min crosshead velocity on SIS/SI blends: A.) with 0, 19, 42, and 54 wt% SI B.) with 0, 19, 42, and 54 wt% SI in 40/60 copolymer/tackifying resin blend, adapted from [83].

Figure 6.2 shows that the diblock copolymer addition results in decreased strain hardening in uniaxial flows. A schematic of the primary mechanism for the unique tunability of SIS/SI block copolymer blends is illustrated in Figure 6.3. Here, SIS/SI blends are shown having glassy polystyrene block segregated domains (red circles) which act as physical cross-links between

polyisoprene elastomeric bridging blocks (blue lines). A decrease in triblock/diblock ratio is shown to result in a decrease in the number of bridging chains and therefore a decrease in strain hardening owing to the fact that the dwindling SIS block copolymer network less efficiently inhibits large strain movement. Overall, these materials get their small strain elastic behavior from local molecular motion in their rubbery bridges and their large strain hardening behavior from long range molecular behavior due to cross-link connectivity, resulting in the behaviors described.
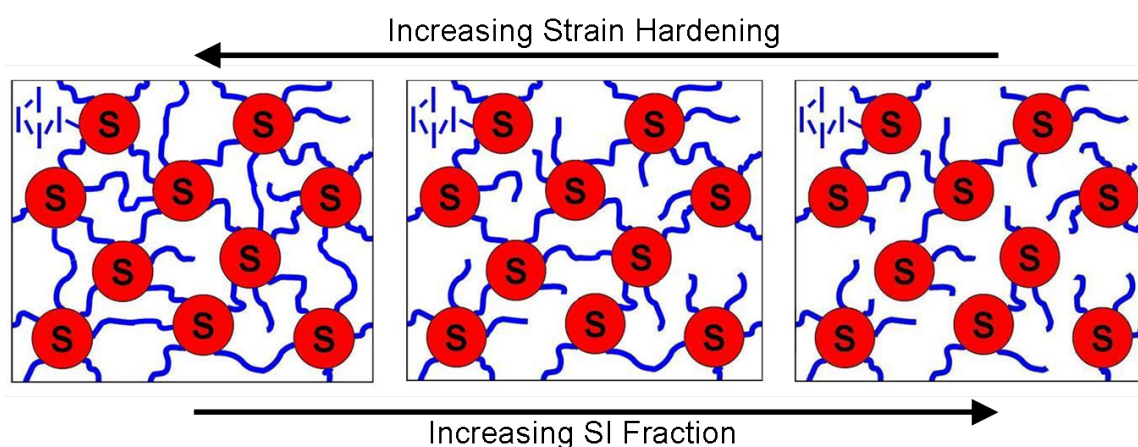
Figure 6.3. SIS/SI mechanism for strain hardening tunability showing glassy polystyrene block segregated domains (red circles) act as physical cross-links between polyisoprene elastomeric bridging blocks (blue lines).

Conceptually, this model system has a vast range of applications to gum base. As per Figure 6.2, SIS/SI copolymer blends have been extensively characterized in uniaxial flows. Such characterization is important, but a fundamental constitutive understanding of the biaxial flow of SIS/SI blends was needed to aid development of novel, tunable materials for application to gum base.

Biaxial true stress (σ_B^T) *vs* biaxial extension ratio ($\lambda_B = \frac{A_m}{A_o} = \varepsilon_m + 1 = \overline{\delta}^2 + 1$) curves are shown in Figure 6.4. The curves represent at least two superimposed inflations of each membrane, differing symbols, and show good reproducibility. Additionally, little variance was observable with changing inflation rates. It is important to note the mechanical instability which occurs between biaxial extensions of 2-4.5 for most of these membranes. This is a geometric transition where the membrane inflates outward as well as upward from a hemispherical to a spherical cap. This instability is reduced as film modulus increases. As seen, increasing SI content decreases modulus (λ_B=1-2) and increases this unstable region. Data gathered in this region require high image capture rates, low inflation rates, or membrane thickening to slow unstable inflation.

More importantly, the curves in Figure 6.4 show decreasing upward curvature with increasing SI content as seen and expected from the data collected by Roos and Creton (Figure 6.2), suggesting a similar biaxial flow control mechanism as that seen in Figure 6.3. Unfortunately, Roos's data (Figure 6.2) and this data are presented differently (σ^N vs σ^T), limiting large strain behavior analysis. Small strain behavior is an adequate comparison to make because nominal and true stress converge at this extreme. The small strain behavior of uniaxial and biaxial SIS/SI flows show similarities. Most apparent is the fact that the tensile and biaxial curves show similar proportional limits for each of the SIS/SI blends ($\sim$20-50%) after which nonlinear behavior dominates. Softening is not as apparent as shown by Roos and Creton because of the difference in stresses reported but some softening is apparent for 19, 42, and 54 wt% SI in SIS/SI blends at intermediate extensions (λ_B =2-6).

A Mooney-Rivlin rubber elasticity model was applied because it tends to model large strain flow behavior better than affine or neo-Hookean theory [5, 111, 112]. Mooney and Rivlin
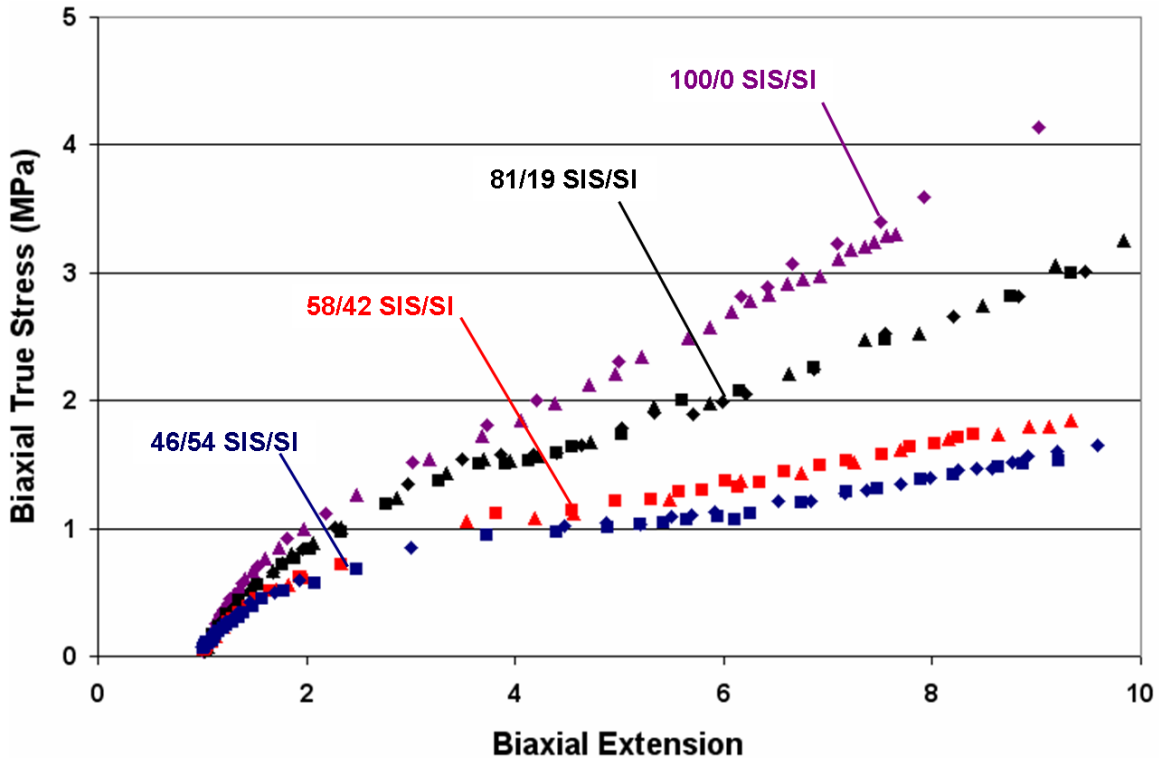
Figure 6.4. SIS/SI blend biaxial constitutive flow behavior. Curves represent at least two superimposed inflations of each membrane, differing symbols, and show good reproducibility.

improved upon affine theory by semi-empirically quantifying deviations from neo-Hookean behavior by using two material constants, C_1 and C_2, which allow modulus evolution with strain. Equation 6.1 shows the Mooney-Rivlin model employed as an elastic strain energy function (U_e) [113]. This model includes extension ratios λ_r, λ_θ, and λ_h which describe deformation in the radial, circumferential, and thickness directions, respectively.

$$U_e = C_1 \left(\lambda_r^2 + \lambda_\theta^2 + \lambda_h^2 - 3 \right) + C_2 \left(\frac{1}{\lambda_r^2} + \frac{1}{\lambda_\theta^2} + \frac{1}{\lambda_h^2} - 3 \right) \tag{6.1}$$

After using Equations 6.1 and 6.2 to describe overall membrane deformation energy, the overall membrane tension can be obtained from Equation 6.3. In these equations, T_o and A are

the membrane pretension and area, respectively. Pretension was assumed to be $\sim 2\gamma$, or 0.07 J/m^2, which is typical for most polymers, where γ is the membrane's surface energy [114].

$$U = T_o A + U_e \tag{6.2}$$

$$T = \frac{dU}{dA} = T_o + A_o h_o \frac{dU_e}{dA} \tag{6.3}$$

After applying symmetry ($\lambda_r = \lambda_\theta = (\varepsilon_m + 1)^{1/2}$) and incompressibility ($\lambda_r \lambda_\theta \lambda_h = 1$), $\lambda_h = (1/\lambda_r)^2$ is obtained. Equation 6.4 was found by combining these assumptions with the differentiation of Equation 6.3.

$$
\begin{aligned}
T &= T_o + 2h_o \left(C_1 + C_2 \lambda_r^2 \right) \left(1 - \frac{1}{\lambda_r^6} \right) \\
&= T_o + 2h_o \left(C_1 + C_2 \frac{A_m}{A_o} \right) \left(1 - \left(\frac{A_o}{A_m} \right)^3 \right) \\
&= T_o + 2h_o \left(C_1 + C_2 (1 + \varepsilon_m) \right) \left(1 - \frac{1}{(1 + \varepsilon_m)^3} \right)
\end{aligned}
\tag{6.4}
$$

The Mooney-Rivlin equation for membrane tension (Equation 6.4) was combined with Equations 6.5 and 3.9 to model the biaxial extensional flow behavior of SIS/SI blends as shown in Equation 6.6. Equation 6.6 was further simplified knowing that $h = h_o \lambda_h$.

$$\lambda_r^2 = \frac{A_m}{A_o} = \lambda_A \tag{6.5}$$

$$\sigma_B = \frac{T_o \lambda_A}{h_o} + 2 \left(C_1 + C_2 \lambda_A \right) \left(\lambda_A - \frac{1}{\lambda_A^2} \right) \tag{6.6}$$

The Mooney-Rivlin constitutive equation (dashed lines) shows an inability to describe biaxial extensional flow behavior of SIS/SI blends with Mooney-Rivlin constants obtained from

uniaxial extensional flows in Figure 6.5. Fundamentally, modeling the biaxial flow behavior of SIS/SI blends with the Mooney-Rivlin equation was important because it could have been a useful predictive tool which has been suggested to give molecular insights into material behavior. For instance, Ferry [115] and Holden *et al.* [116] suggest that C_1 is representative of the trapped entanglements and physical cross-links in a material and that C_2 is more indicative of temporary entanglements. However, it is not surprising that Roos' constants [83], shown in Figure 6.6, do not fit both uniaxial and biaxial flows well because biaxial flows are known to strain soften significantly more thus large strain behavior should especially not be modeled well. This expectation is clearly shown in that the model predicts low strain behavior well but fails at biaxial extensions (λ_A) greater than ~1.5.
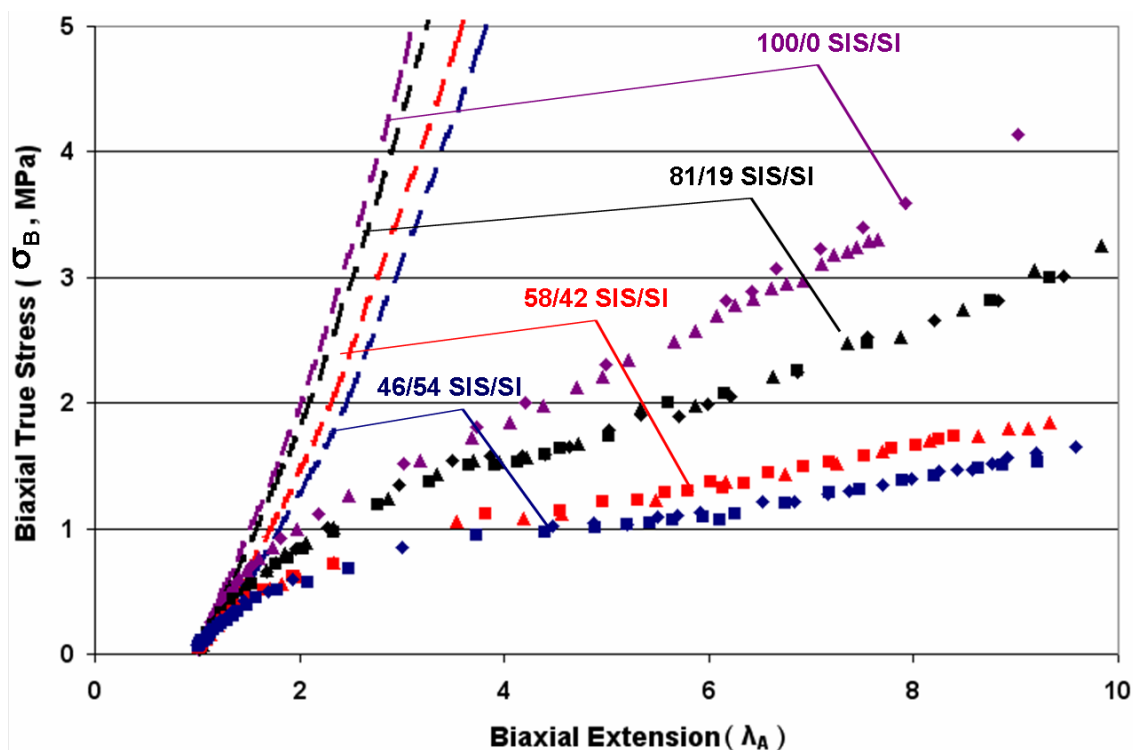
Figure 6.5. SIS/SI blends with Mooney-Rivlin model superimposed. Mooney-Rivlin model utilizes Roos' constants shown in Figure 6.6.
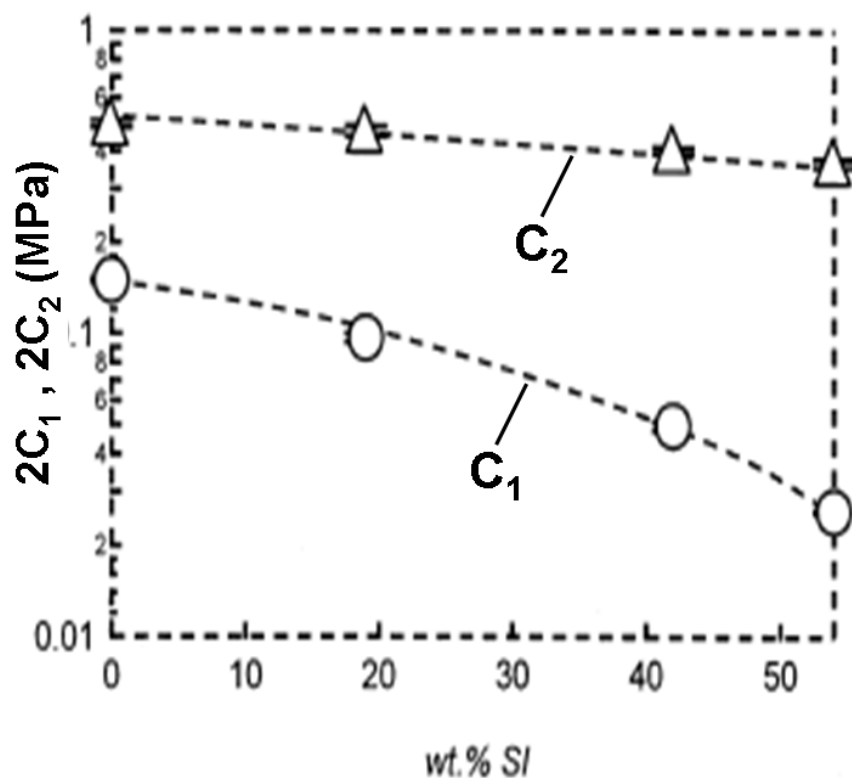
Figure 6.6. MR constants for fitting σ_U^N vs ε_U behavior at $\sim$22 °C for SIS/SI blends of 0, 19, 42, and 56wt% SI, adapted from [83].

A fit of the SIS/SI blend data with the general exponential strain hardening expression in Figure 6.7 reveals a 30% decrease in both σ_o (0.49 - 0.35) and k (0.95 - 0.66) when going from 0 to 54 wt% SI. The decrease in σ_o and k values were expected because the physically cross-linked SIS network has decreased load transferability with increased SI content. Although close, the maximum achievable biaxial strain hardening parameter k_B-values in this study were only found to be 0.95, while theory says a value of at least 1 is needed for resistance to plastic flow localization and failure in balanced biaxial flow. Therefore, this polymer system offers encouragement for the potential future design of novel gum bases, but does not immediately offer any solutions to help design a super bubblegum.
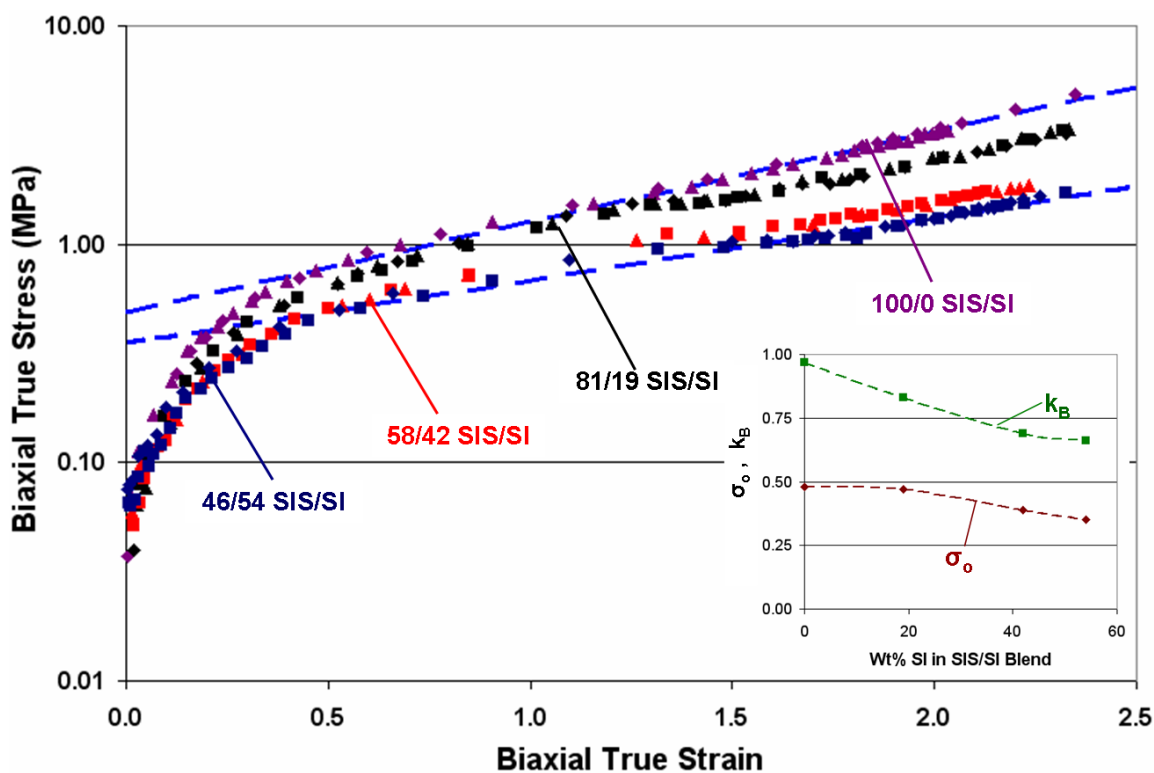
Figure 6.7. SIS/SI blends with exponential hardening superimposed. A plot of exponential strain hardening fitting parameters is inset into this figure and showns decreasing uniaxial strain hardening parameter (k_U) with increase SI wt%.

6.2.2. VAVL Block Copolymer Model System

A vinyl acetate / vinyl laurate (VAVL) copolymer was briefly studied for prototyping super bubblegum base because its modified PVAc branch-like molecular architecture, shown schematically in Figure 6.8 was thought to possess possible strain hardening benefits. Preliminary investigations with unconstrained chew viscosity gums involved substitution of VAVL copolymer into the PVAc portion of the control. All ($y_{VAVL}^{I} = 1$) and half VAVL ($y_{VA/VL}^{I} = 0.5$) copolymer substitution resulted in mean bubble diameters which were only 63% and 36% of the HBSS control's diameter (Figure 6.9).
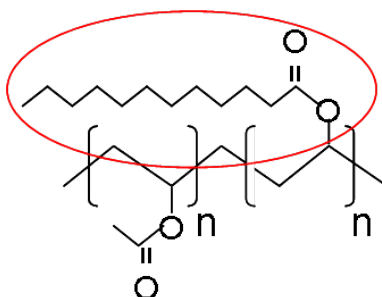
Figure 6.8. Poly(vinyl acetate - vinyl laurate) molecular structure. Red circle points out the branch-like laurate side chain.
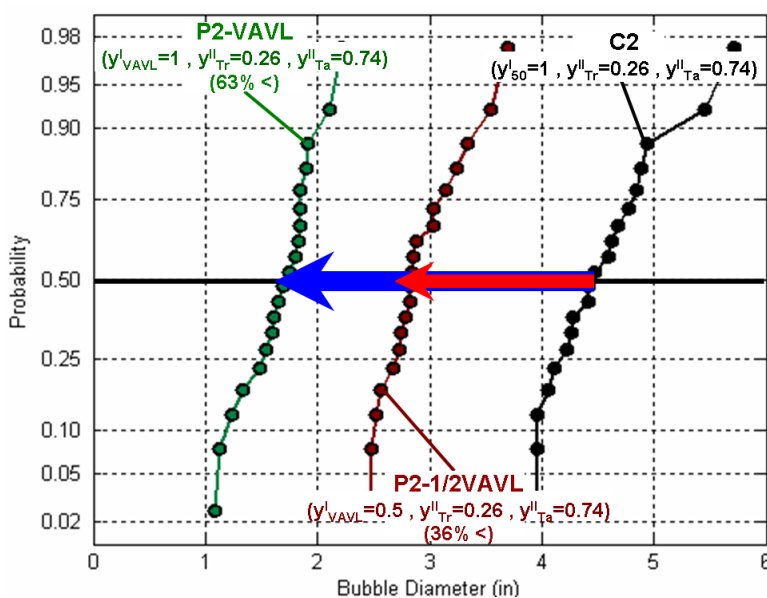
Figure 6.9. Poly(vinyl acetate - vinyl laurate) bubble diameter results without viscosity constraint. Blue and red arrows point out the decrease in bubble size for P2-VAVL and P2-1/2VAVL prototypes, respectively.

The uniaxial characterization of VAVL shown in Figure 6.10 shows strong evidence, whether it be a result of viscosity or molecular effects, for increased strain hardening (vertical yellow arrow) being correlated to increased bubble diameter (horizontal yellow arrow). Curvature was characterized using the exponential strain hardening expression, and the strain hardening parameter (k) is graphically shown to be 13% and 56% less than the control's (C2, 2 = design

iteration) value for the P2-VAVL and P2-1/2VAVL prototypes, respectively. Additionally, the decrease in σ_o is also graphically demonstrated suggesting the result arising from dominant viscosity effects in this prototype iteration.
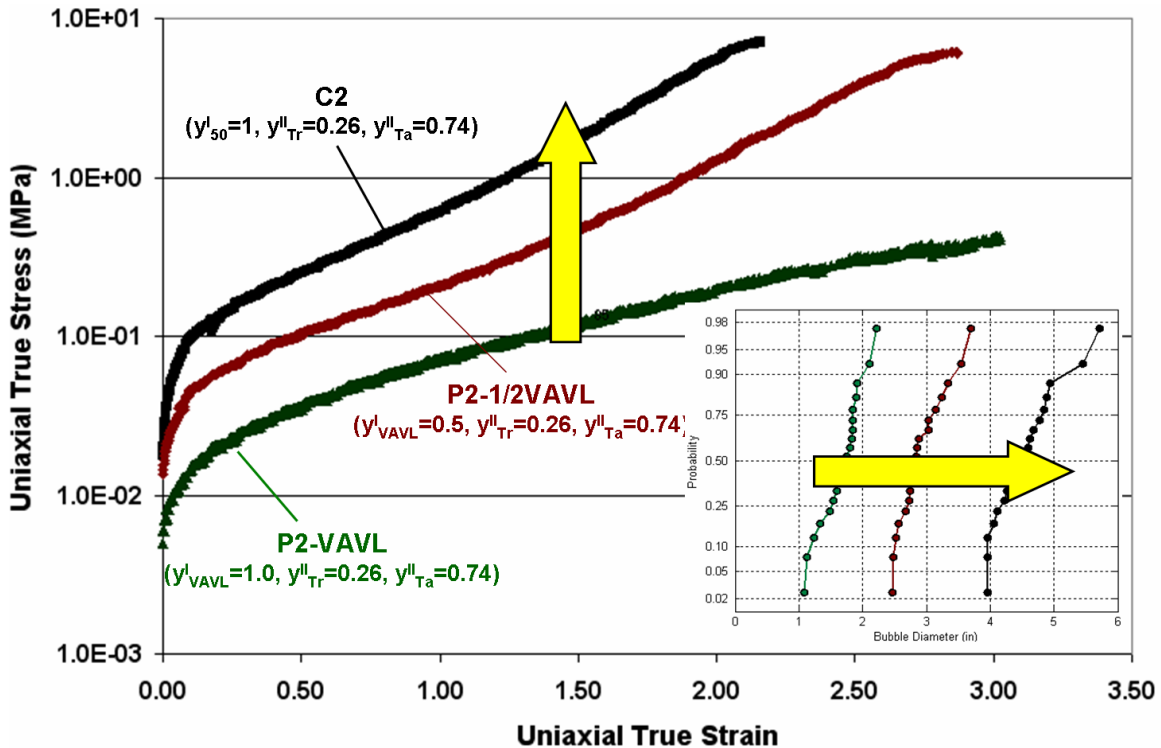
Figure 6.10. Preliminary poly(vinyl acetate - vinyl laurate) gum base comparison of uniaxial σ^T vs ε^T behavior and mean bubble diameter. A severe decrease in flow stress is seen demonstrating the need for a viscosity constraint for the characterizaton of this gum base system. Yellows arrows qualitatively demonstrate the increase in bubble diameter (inset graph) associated with increasing uniaxial strain hardening parameter, k.

Results from the constrained viscosity prototype iteration for the VAVL conceptual gum base (P3-VAVL) are shown in Figure 6.11. The complex viscosity of this prototype was shown to be designed within 3% of the control in Chapter 5, therefore assuring the minimization of viscosity effects. The VAVL copolymer continued to show a 45% smaller mean bubble diameter

than the control, indicating an inherent performance disadvantage within VAVL bubblegum base attributed to its vinyl laurate sidechain.
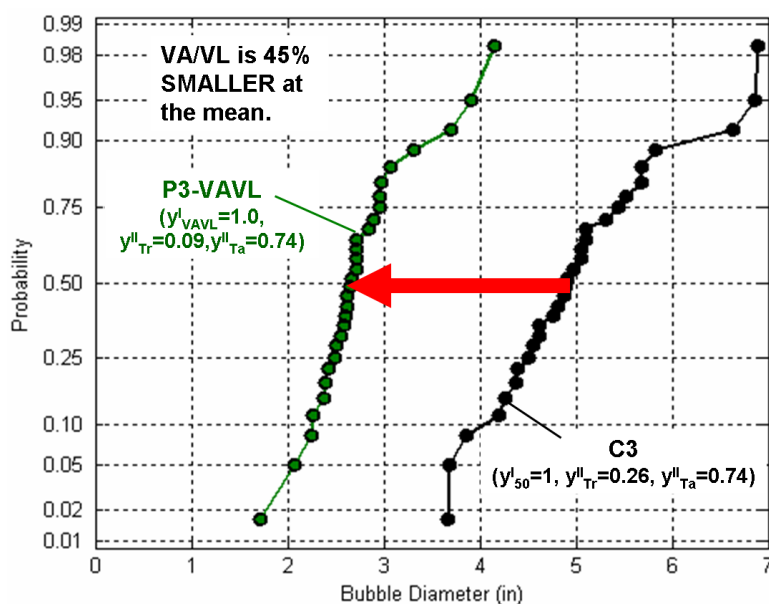
Figure 6.11. Poly(vinyl acetate-vinyl laurate) bubble diameter results with viscosity constraint. The red arrow still shows a 45% decrease in bubble diameter with a constrained viscosity.

Uniaxial characterization of VAVL gum base displays strain hardening which is still 20% less than the control gum base, C3 (see Figure 6.12). Such a decrease in strain hardening under the constraint of constant viscosity further indicates that the poor performance of VAVL gum bases is dictated by the VAVL molecular architecture. The decrease is most likely due to the laurate side chains acting as flexible molecular spacers between adjacent polymer chains instead of entanglement enhancers as hoped. This result was not necessarily unexpected because the PE film blowing industry takes advantage of long chain branched LDPE with side chains of 1,000s of carbons in length, not 11 as seen in Figure 6.8 [58].
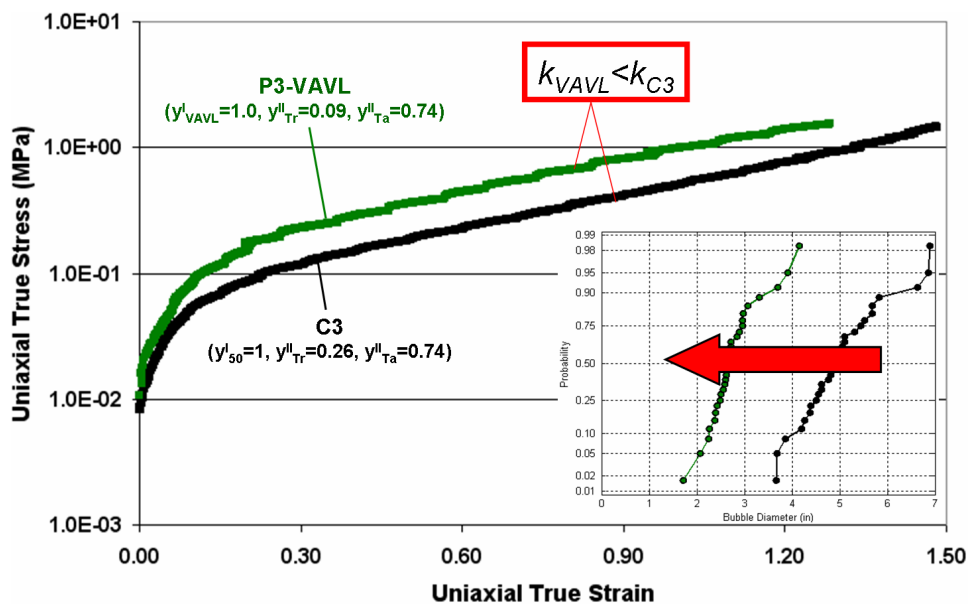
Figure 6.12. Poly(vinyl acetate - vinyl laurate) constrained gum base viscosity comparison of uniaxial σ^T vs ε^T behavior and mean bubble diameter. Red arrow indicates decreased strain hardening resulting in decreased bubble diameter resulting from the VAVL molecular architecture.

Uniaxial yield (σ_o) and strain hardening parameter (k) values are tabulated in Chapter 7 where uniaxial extensional behavior *vs* mean bubble diameter comparison will undergo extensive analysis. Based on the conceptual investigations peformed in this chapter, the design of bimodal PVAc gum bases looks like the best opportunity for the design of high performance bubblegums.

CHAPTER 7

Bimodal PVAc Gum Base Prototype Design and Characterization

Poly(vinyl acetate) (PVAc) bimodal architectures were designed into bubblegum base as the most promising approach to stabilize biaxial plastic flow and increase *in-vivo* bubble diameter. Bimodal distributions which were parameterized, modeled, and qualitatively validated in Chapter 4 were used to guide bimodal prototype designs. The chew viscosity model developed in Chapter 5 was employed to constrain second and third generation prototypes to acceptable viscosities (350-700 Pa*sec). Gum bases and gums were characterized in uniaxial and biaxial extensional flow, respectively, for the validation of *in-vivo* bubble results. Uniaxial extensional flow is demonstrated as an adequately predictive method for the description of *in-vivo* bubble performance via strain hardening parameter (SHP, k). Excess uniaxial strain hardening is also demonstrated to accurately promote ideal biaxial constitutive behavior.

7.1. Approach Overview

The purpose of this chapter is to demonstrate the systems approach to the design of the PVAc component of gum base to optimize bubble diameter while maintaining acceptable chew viscosity. In Chapter 6, two alternative design concepts were examined but neither demonstrated the type of exponential σ_B^T-ε_B^T behavior desired to optimize bubble diameter. SIS/SI blends were shown to have uniquely tuned strain hardening but require further development before implimentation in bubblegum base. Additionally, VAVL copolymers are used in the gum industry but also do not show an ability to strain harden during flow to increase bubble diameter.

Thus, a focused effort in the application of PE film blowing technology to PVAc gum base was employed for the design of a high performance bubblegum.

Based on the survey and modeling of the PE film blowing industry (see Chapter 4), molecular weight ratio (MWR) and high molecular weight (HMW) fraction were found to be the parameters of greatest interest for the design of the PVAc molecular weight distribution (MWD) of gum base to achieve optimal ductility. The PE film blowing technology showed high density polyethylene (HDPE) as being advantageously designed between MWRs of 7-70 and HMW fractions of 20-60%. This data was modeled and used to guide bimodal PVAc prototype design. Such stabilization is achieved in the HDPE film blowing industry by broadening HDPE MWDs to lengthen overall relaxation time, increase entanglements/flow induced physical crosslinks, and increase flow strain hardening. This chapter will present how strain hardening was increased in bubblegum base while under the constraint of gum chew viscosity following the model developed in Chapter 5. Ultimately, gum bases and gums were characterized under uniaxial and biaxial extensional flow to quantitatively validate *in-vivo* bubble size increases with measurable fundamental constitutive behavior.

7.2. Prototype Design

7.2.1. *In-vivo* Performance Time Evolution

One test subect, the author, was used for all *in-vivo* tests performed after the first prototype (P1). These tests were performed as double blind studies where samples were weighed and coded independently of the author. Only one subject was used for prototypes 2 (P2) and 3 (P3) because the 380 kg/mol PVAc utilized to induce bimodality of the PVAc MWD is not normally used in gum base and thus not administered to test subjects unaffiliated with the research sponsor. The

concern is with the high pre-processing vinyl acetate monomer content, but it should be noted that internal industry reports indicate a significant diminishing of its presence after volatilization during processing [117].

Since one subject was used for *in-vivo* experimentation of P2 and P3 prototypes it is important to understand that subject's evolution of bubble blowing ability. An analysis of Figure 7.1 shows an initial average Hubba Bubba Max (HBMax) bubble blowing ability for maximum diameter and a slightly better than average for mean diameter, with respect to a bubble blowing population of 70 Northwestern University Engineering Design Communication (EDC) undergraduates. The purpose for the EDC study was to use the population as a reference for future *in-vivo* tests in an attempt to track the overall ability increase of the author. Prototype 2 was tested on two different occasions (labeled t_1 and t_2) and 3 was tested at a third time point, t_3. The author's position on the distribution is represented by green, blue, and purple stars for tests t_1, t_2, and t_3, respectively. As seen, the subject's ability increases from t_1 to t_2 for the inflation of P2 and even more evidently at t_3 for the testing of P3. Some effect was expected based an different aging times for the Hubba Bubba Max^{TM} Outrageously Original gums used but similar increases have been seen for laboratory control HBSS gum performance. Because of this, all prototype gums are compared to the results of that prototype iteration's control diameter.

7.2.2. Prototype 1

7.2.2.1. P1 Development. The PE film blowing industry's use of bimodal MWDs to improve plastic film stability and ductility through increased entanglement governed the design of the first generation prototype (P1). This approach was initially mimicked without the use of the PE film blowing parametric model (presented in Chapter 4) as a design guide or the gum viscosity
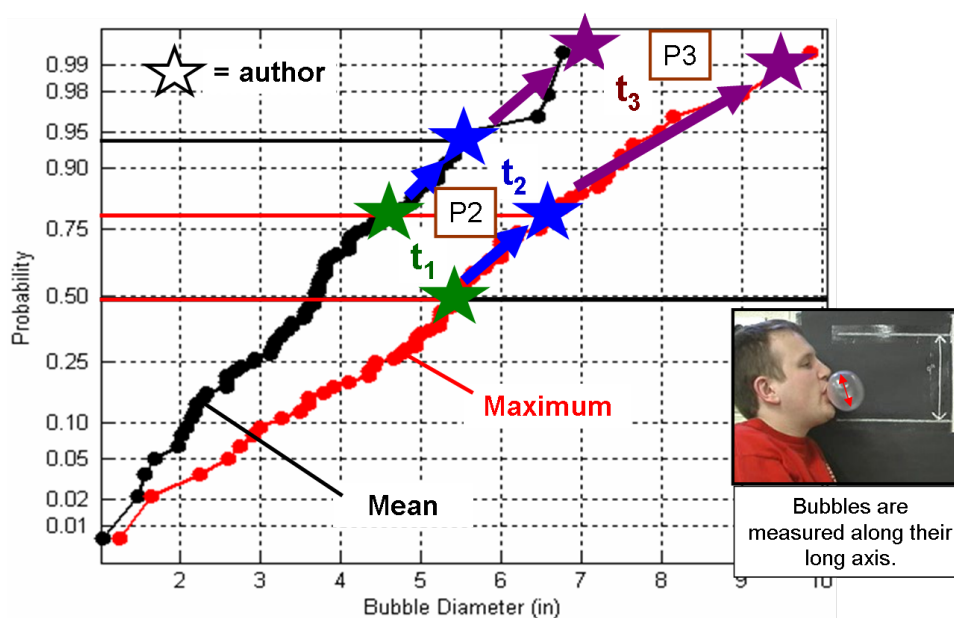
Figure 7.1. Hubba Bubba^{TM} Max bubble diameter population (70 NU EDC undergraduates) with subject's performance overlayed (t_1¡t_2¡t_3).

constraint (presented in Chapter 5) in an effort to gain early experience. Simultaneously, some initial experiments pointed towards the need for more triacetin to prevent excessive chew viscosities after adding 380 kg/mol PVAc. Ultimately, P1 gum bases were designed with y^I_{380}= 0 - 7.5 wt% of the PVAc component being 380 kg/mol with the balance being 50 kg/mol (based on HBSS control). More 380 kg/mol PVAc would have been used but a survey of five company interns found such increases resulting in perceived chew unacceptability and no model had yet been formulated to predict the amount of triacetin required for acceptability.

The first generation prototype (P1A-D) was designed having y^I_{380}= 0 - 7.5%, at 2.5 wt% increments, with y^{II}_{Tr}=0.33 and y^{II}_{Ta}=0.74. P1D (y^I_{380} = 7.5 wt%) had the greatest bubble diameter of all P1 prototypes but did not show a significant increase compared to the HBSS laboratory control (C1) (see Figure 7.2). Its bubble diameter was larger than the control by 20% and 3% at the median and 90th percentile, respectively, but 4% smaller at the 99th percentile. Overall,

P1 showed a 14% greater mean bubble diameter than the control. These small bubble diameter increases support the concept but show the need for further optimization.
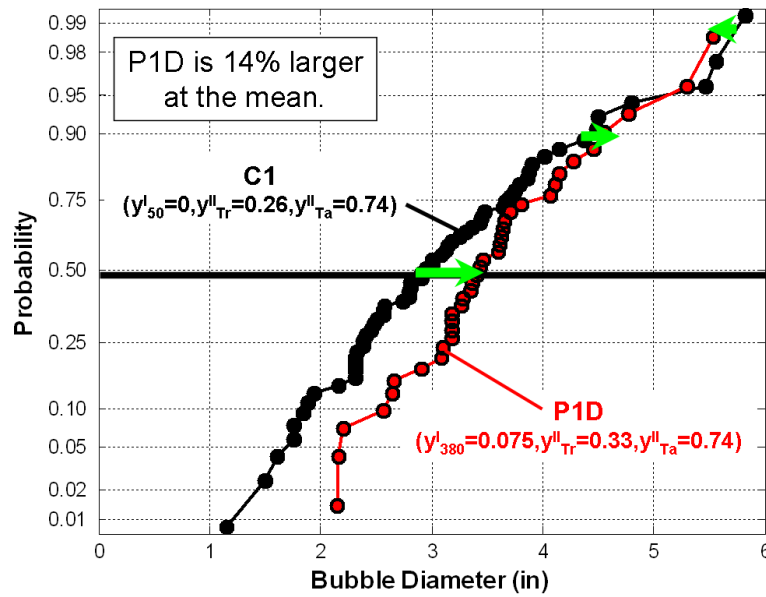
Figure 7.2. Normal probability plot of P1 results without a chew viscosity constraint show a ∼14% bubble diameter increase for P1D with respect to the C1.

The mean bubble diameter was initially used because it is the best statistically defined and accounts for entire bubble diameter distribution. On the other hand, the 90th percentile may be a more appropriate performance metric because it represents the performance increase that a bubble blowing customer should achieve at least 10% of inflation events, which is thought to realistically be frequent enough to influence "perceived" bubble diameter.

7.2.2.2. P1 Characterization. Uniaxial σ_U^T vs ε_U^T curves for C1 and P1D gum bases, shown in Figure 7.3, suggest a lack of bubble stabilization resulting in unimproved biaxial ductility and minimal bubble diameter increase (shown in Figure 7.2). A lack of measured uniaxial strain hardening increase was most likely due to a combination of the HMW portion of the bimodal gum base either having too small a weight fraction for adequate homogeneity or a large enough

weight fraction for adequate homogeneity but still too little an amount to overcome triacetin's plasticization and produce a stabilizing effect.
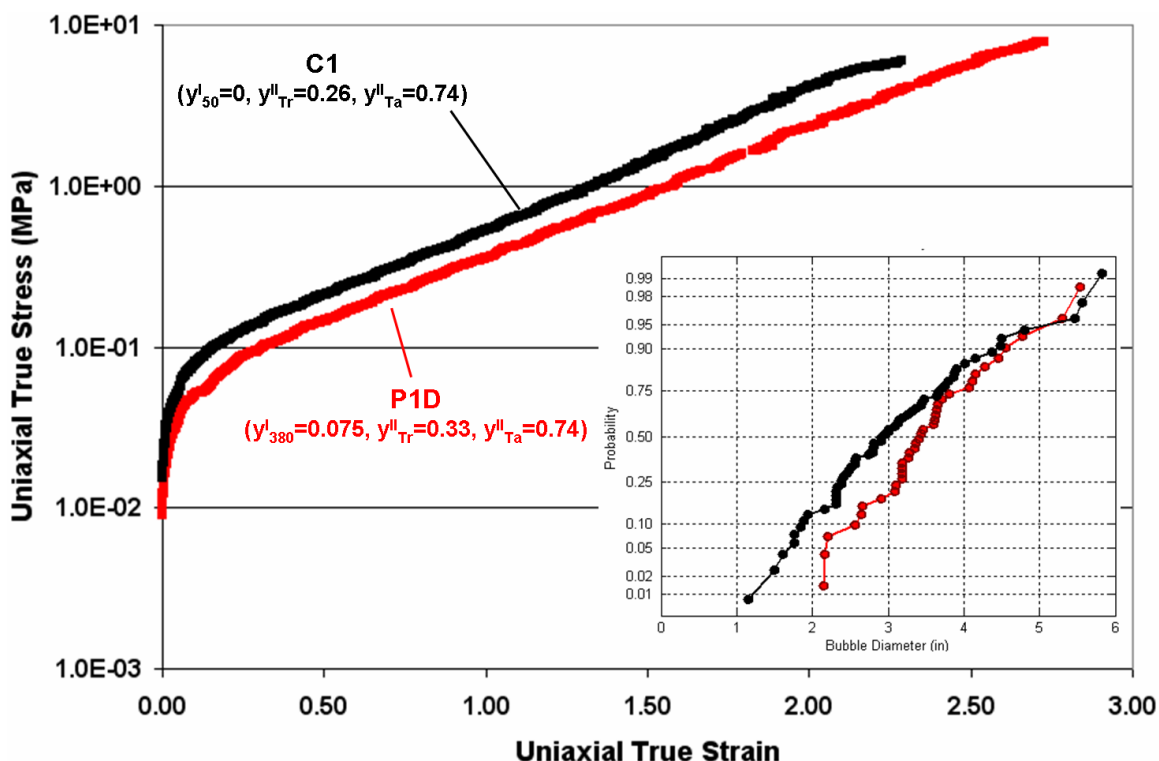
Figure 7.3. Uniaxial σ_U^T vs ε_U^T curves for Ca and P1D at 22 °C. Correlating colors are used to compare σ_U^T vs ε_U^T constitutive behaviors to their resulting bubble diameter normalized probability distributions while yellow arrows correlate increasing strain hardening to increasing bubble diameter.

Perhaps this result is best understood when examining the σ_U^T vs ε_U^T behavior of all first generation prototypes. Figure 7.4 illustrates that increased strain hardening (vertical yellow arrow) results in increased bubble diameter (horizontal yellow arrow) for P1A-P1D. Therefore, the desired effect was achieved within the P1 prototype data set but not with respect to C1. The answer to the role of HMW fraction in gum base lies in the location and shape of the P1 bubble diameter distributions. First, an increase in HMW fraction in 2.5 wt% (from P1A= 0

wt% to P1D= 7.5 wt%) results in increased bubble diameter suggesting that, although HMW materials is in gum base in small amounts, it is still homogeneously mixed into gum base to effect *in-vivo* bubble performance. Additionally, P1A and P1B display a slim distribution of bubble diameters centered on the low side of the control showing triacetin's large diminishing effect on bubble diameter when weight fraction of triacetin is increased without also increasing the weight fraction of HMW PVAc in gum base. However, as HMW fraction is increased, P1C and P1D demonstrate a comparative broadened S-shape to their bubble distributions resulting in bubble performance greater than the control in P1D.
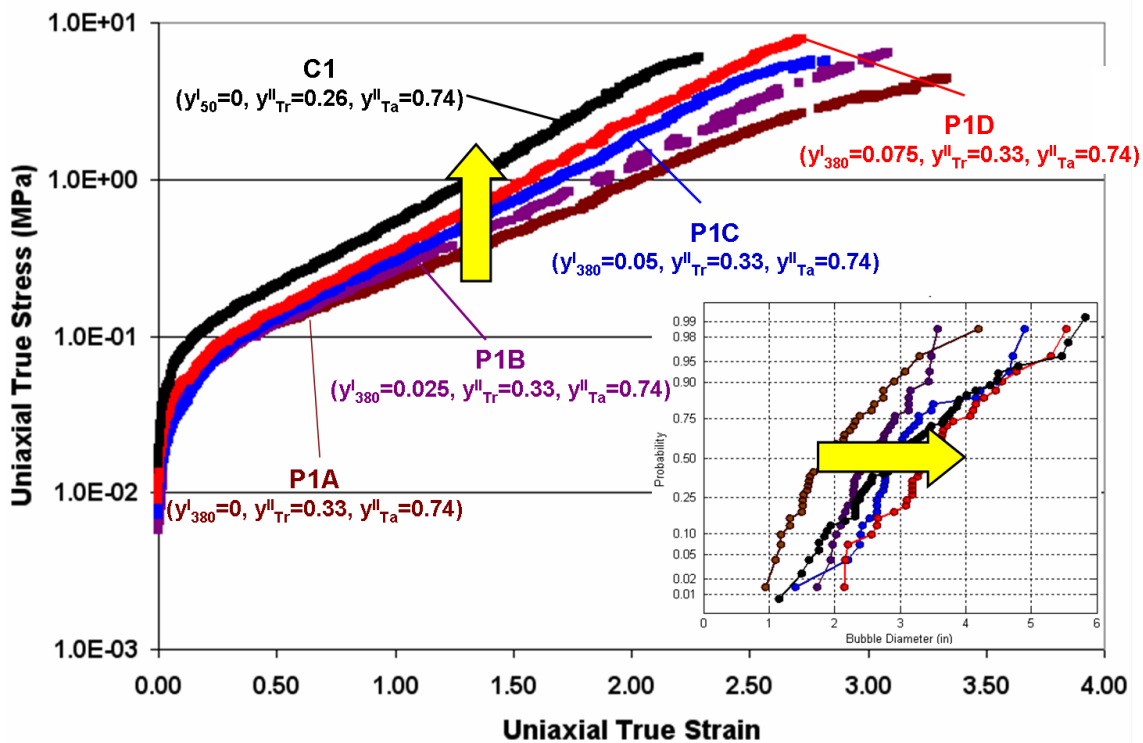
Figure 7.4. Uniaxial σ_U^T vs ε_U^T curves for C1 and P1A-D at 22 °C. Correlating colors are used to compare σ_U^T vs ε_U^T constitutive behaviors to their resulting bubble diameter normalized probability distributions while yellow arrows correlate increasing strain hardening to increasing bubble diameter.

7.2.3. Prototype 2

7.2.3.1. P2 Design. A more detailed review of the PE film blowing literature was undertaken after obtaining limited results with P1. In Figure 7.5, it is apparent that P1 resided outside the surveyed HDPE film blowing operating region both in MW ratio (380 kg/mol / 50 kg/mol = 7.6) and high molecular weight (HMW) fraction (7.5 wt%). The second generation design was chosen to reside well within the HDPE operating region (MWR = 25, HMW fraction = 30 wt%) so as to design excess strain hardening.
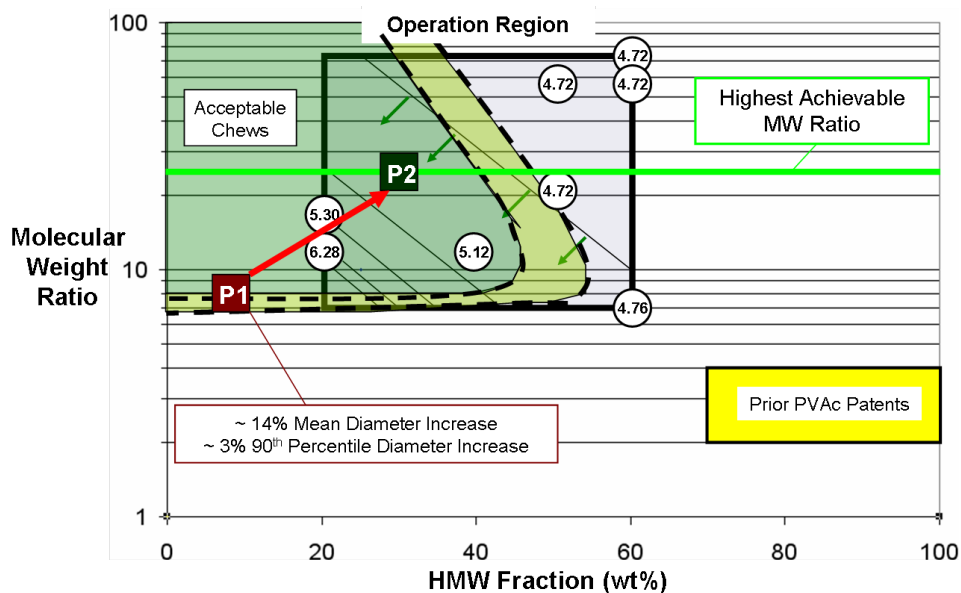
Figure 7.5. P2 design with overlayed chew viscosity constraint. Dark and light green shaded areas represent the upper limit (700 Pa*sec) of the acceptable chew viscosity region for two different levels of triacetin in gum base as predicted by the recalibrated viscosity model.

Two second generation prototypes were designed, one with talc ($y_{Ta}^{II} = 0.74$) and one without talc ($y_{Ta}^{II} = 0$) are denoted P2A and P2B, respectively. These two designs were made to

answer the question of whether or not talc limits high strain hardening biaxial flow bubble diameter. If not, then there would be confirmation that bubble size was plastic flow stability controlled as has been the assumption of this design approach.

P2A and P2B design depended highly upon studying the chew viscosity effect of MWR and HMW fraction because its intention was to explore as deep within the HDPE film blowing operation region as possible before the loss of chew adequacy. The highest achievable MWR (380 kg/mol / 15 kg/mol = 25.3) was limited by commercial PVAc MW availability, but the amount of HMW capable of being placed into the gum base was not yet understood. Therefore, a preliminary chewability model for the constraint of chew viscosity to that of the control (660 Pa*sec) was formulated and utilized. This model predicted a HMW fraction upper limit of ~30 wt%. The chew viscosity of P2A was found to be 550 Pa*sec after testing, resulting in it lying to the left of the limits proposed, and thus required recalibration to the current accurate limits of Figure 7.5.

P2's design represents the first prototype where the Materials by Design^{TM} systems approach was implemented with parametric predictive modeling of PE performance and chew viscosity constraints as guides. This approach resulted in a bubble diameter increase by P2A with respect to the laboratory HBSS control (C2) of 26%, 30%, 41%, and 39% on the mean, median, 90th, and 99th percentiles, respectively (Figure 7.6). More importantly, this gum design achieved bubble diameters which were comparable to those of Hubba Bubba^{TM} Max (HBMax) Outrageously Original, the best performing commercial bubblegum as determined by a bubble study performed with the NU Engineering Design and Communication classes in the Spring of 2006 (Figure 7.7). This work proved that a bubblegum with a simple microstructure like HBSS (8 gum base components) can be designed to perform as well as empirically developed complex

bubblegums like HBMax (14 gum base components). Such simplicity has potential cost saving

benefits if implemented correctly commercially.
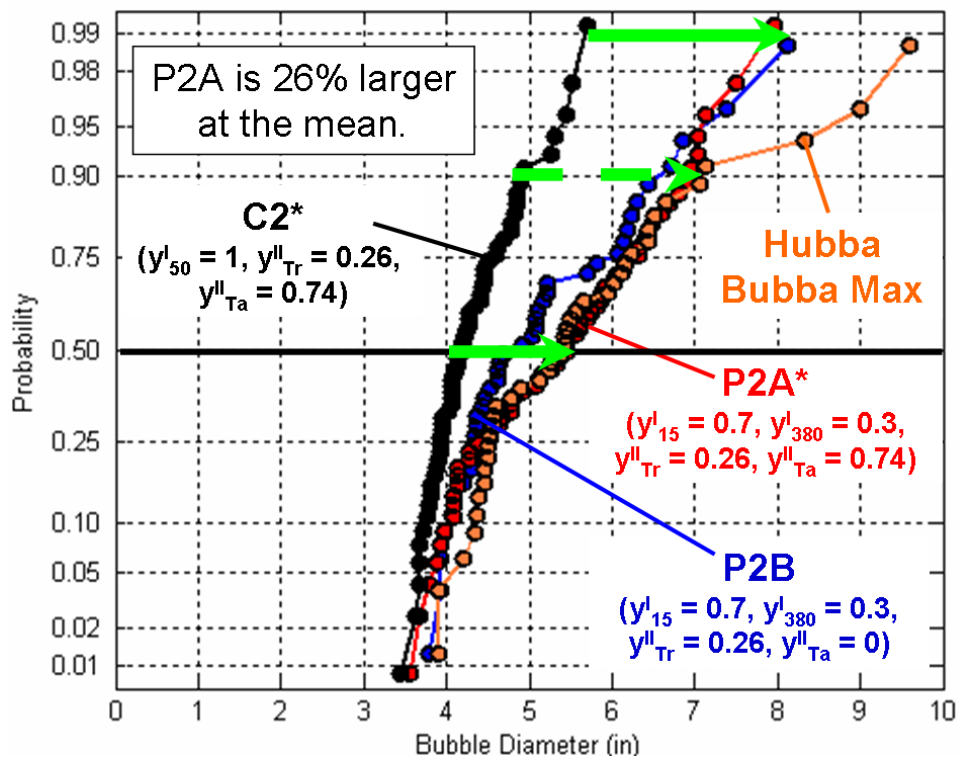
Figure 7.6. Second generation prototype bubble diameter results comparison to control and HBMax. This provided graphical proof that a bubblegum with a simple microstructure such as HBSS (8 components) can be designed to perform as well as an empirically developed, complex bubblegum like HBMax (14 gum base components).

Interestingly, P2A and P2B display comparable bubble diameters in Figure 7.6 suggesting

the initial design assumption that bubble size was controlled by plastic flow stability rather

than talc induced fracture mechanisms was correct. Furthermore, additional concerns about

super bubble prototypes costing more than the HBSS control if they had to be talc free were

temporarily removed.
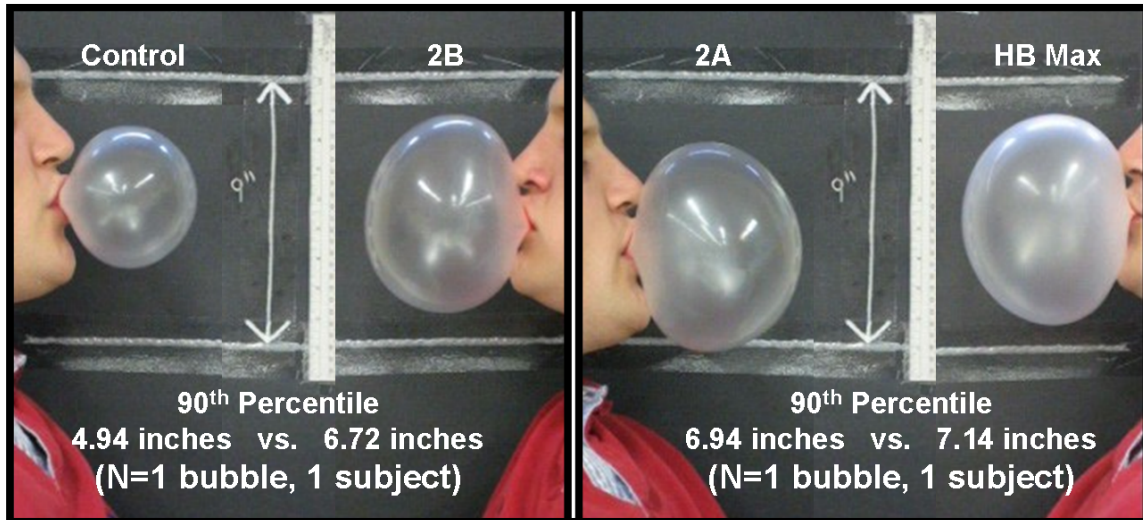
Figure 7.7. Visual comparison of P2A and P2B bubble diameter versus the control and HB Max at the 90th Percentile.

7.2.3.2. P2 Characterization. The second generation prototype continued to display increased strain hardening that resulted in increased bubble diameter as shown in Figure 7.8. In this case, bubble diameter shifts to the right (gets larger) across the entire normal probability distribution and broadens at the highest performance percentiles. This kind of skewed distribution is favorable because it means larger bubbles are achieved more often for P2A and P2B than for the control resulting in greater perceived performance. The lack of bubble diameter increase for P2A over P2B suggests a saturating behavior for uniaxial strain hardening parameter's (k) prediction of bubble diameter. However, the limit of that behavior had not yet been reached in this design. More discussion is presented in the next section of this chapter.

Additionally, talc demonstrates a positive effect on material strain hardening as shown by the comparison of the P2A ($y_{Ta}^{II} = 0.74$) and P2B ($y_{Ta}^{II} = 0$) constitutive behaviors in Figure 7.8. This observation has been seen in other data but not yet entirely explained. Some potential explanations are that talc likely has a role in maintaining homogenization after mechanicial
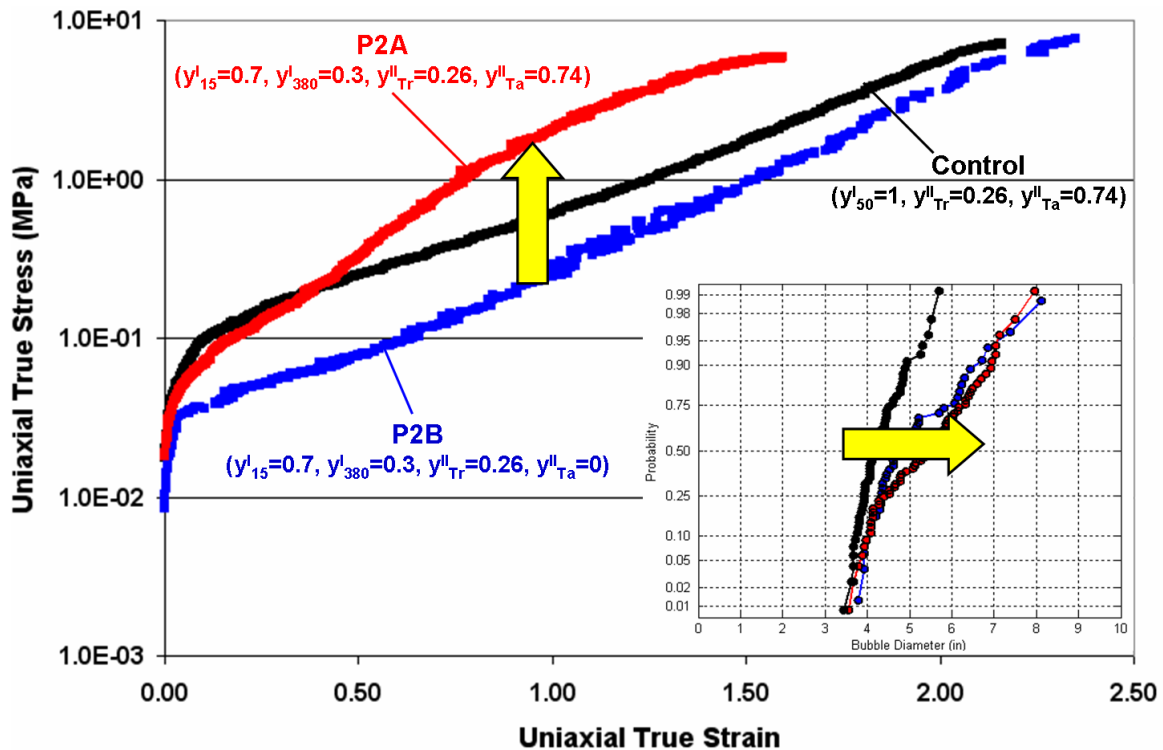
Figure 7.8. Uniaxial σ_U^T vs ε_U^T response comparisons to control (C2) for second generation prototypes, P2A and P2B. Correlating colors are used to compare the σ_U^T vs ε_U^T constitutive behaviors to their resulting bubble diameter normalized probability distributions while yellow arrows indicate increased bubble diameter with increased strain hardening.

mixing, which has been observed in simple binary PVAc systems by Nesterov et al. [118, 119], or aids the compounding process itself by enhancing the shear viscosity of the gum base.

7.2.4. Prototype 3

7.2.4.1. P3 Design. Even though P2A exhibited an increased mean bubble diameter of 26% with respect to the control, the overall objective of increasing mean bubble diameter by 50% and bubble diameters to 10 inches had not yet been achieved. For this, the parametric PE model developed in Chapter 4 was fully implemented for prediction of the third generation prototype

(P3). As seen in Figure 7.9, the model suggests largest achievable strains occurring in MWD's with a 20 wt% HMW fraction. An overlay of the acceptable chewability model (seen at two triacetin levels in different shades of green) demonstrates the possibility of reaching the entire left hand edge of the HDPE operation region. Thus, two prototypes were designed at MWRs of 25.3 (P3A) and 7.6 (P3B) with 20 wt% HMW fractions. As mentioned in Chapter 5, their viscosities were constrained to within 5% of the average laboratory control value (660 Pa*sec).
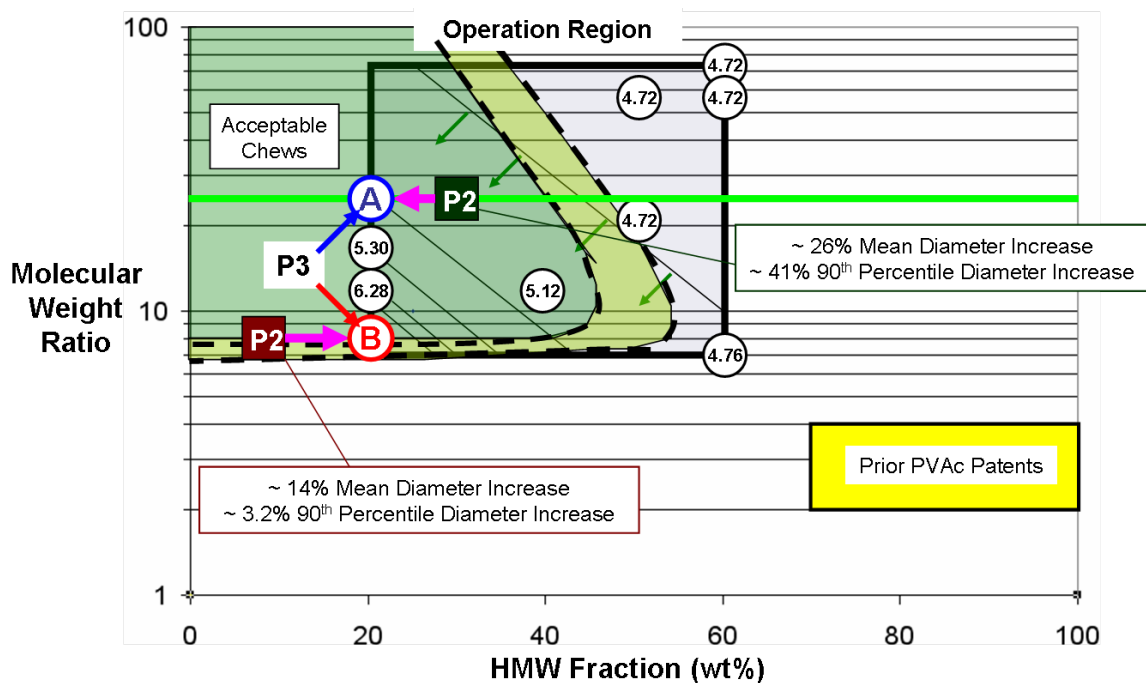
Figure 7.9. Third generation prototype design with overlayed chew viscosity constraint. Dark and light green shaded areas represent the upper limit (700 Pa*sec) of the acceptable chew viscosity region for two different levels of tri-acetin in gum base as predicted by the recalibrated viscosity model.

The third generation prototype was tested in two test sessions, once against the laboratory control and another against HBMax. Bubble diameter increases of 50%, 53%, 40%, and 38% are seen at the mean, median, 90th, and 99th percentiles in Figure 7.10, respectively. This

prototype reached both design objectives for the super bubblegum by having a mean bubble diameter increase of 50% and and maximum bubble diameter of ∼10 inches. One interesting observation is that P3A and P3B have a qualitatively similar bubble diameter increases, which follow the predictions of the parametric PE model and thus lend validity to further development of that model for the prediction of a fourth prototype (see Chapter 8.5).
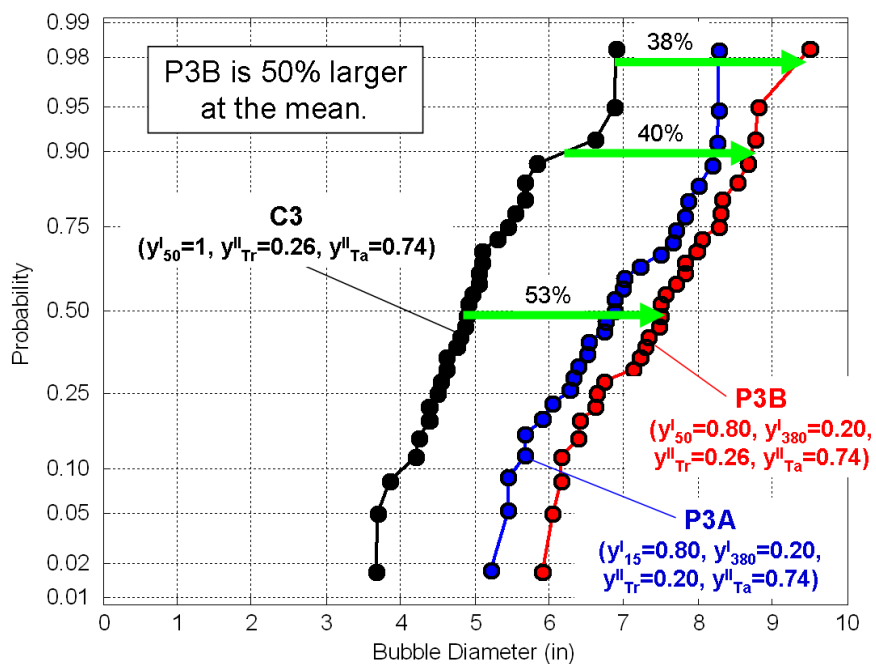
Figure 7.10. Normal probability distribution of third generation prototypes *vs* control bubble diameter results. This graph shows a mean bubble diameter increase of 50% over that of the control to a diameter of ∼7.5 inches.

In-vivo bubble tests indicate P3B outperforming HBMax by 14%, 10%, 25%, and 22% at the mean and median, 90th, and 95th percentiles, respectively, as shown in Figure 7.11. This further confirms that a simple microstructure can outperform a complex one with a properly designed MWD. The dashed black line in this figure indicates an even greater bubble diameter for P3B with respect to the control where maximum bubble diameters approach 11 inches!
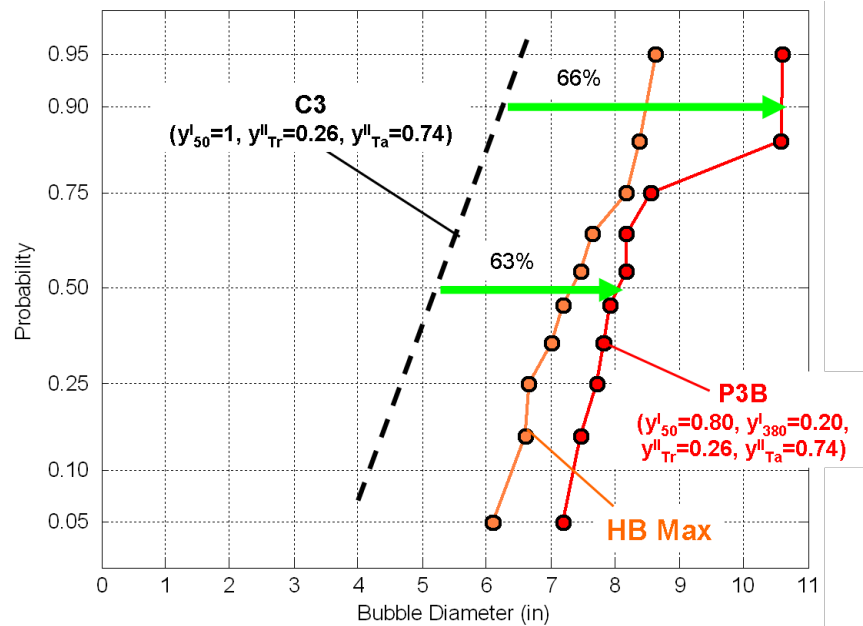
Figure 7.11. Normal probability distribution of third generation prototype *vs* Hubba Bubba^{TM} Max bubble diameter results. This graph shows P3B outperforming the best commerically available bubblegum, Hubba Bubba^{TM} Max.

The new prototype is shown to be more impressive than both the laboratory control and commercial HBMax at the mean and 90th percentile performance indexers in Figure 7.12. Now, that such a large bubble has been achieve it is up to the author to scientifically demonstrate why bubbles as large as 11 inches are being achieved.

7.2.4.2. P3 Characterization. Figure 7.13 shows the same trends which have been shown throughout this chapter but also indicates the beginning of possible fracture mediated flows rather than stabilized plastic flow mediated flows. The strain hardening of P3A was larger than for P3B as tabulated in Table 7.1 but results in a decreased mean bubble diameter. This implies that excessive strain hardening was becoming detrimental to film ductility and that a possible fracture limited regime has been entered. This fracture limited regime was even further evidenced by a loss in stabilizing upward curvature in the uniaxial extensional flow tests seen
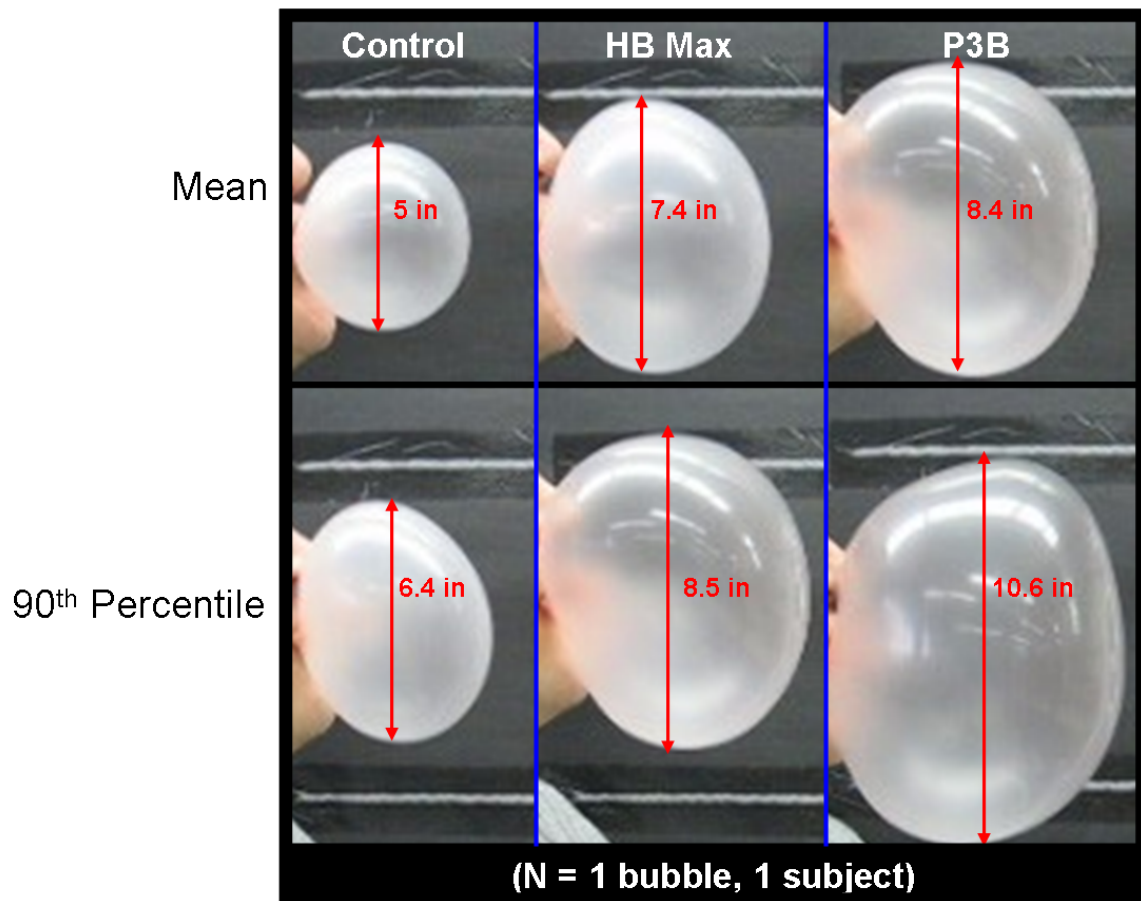
Figure 7.12. Visual comparison of simple Control, simple third generation pro-
totype (P3B), and complex Hubba Bubba^{TM} Max commercial formulation.

in Figure 7.13 at low strains. Thus, P3B has less fracture initiated processes than P3A and
therefore maintains a fixed strain hardening ($\frac{d\sigma}{d\varepsilon}$) parameter k longer before failure.

7.3. Extensional Flow Characterization Analysis

7.3.1. Uniaxial Extensional Flow

Uniaxial strain hardening parameter values for all previously displayed uniaxial σ *vs* ε curves
are tabulated in Table 7.1. This table is organized from lowest to highest uniaxial strain hard-
ening parameter (*k*) corresponding to P2-VAVL to P3b* where P3b*, as well as the rest of the
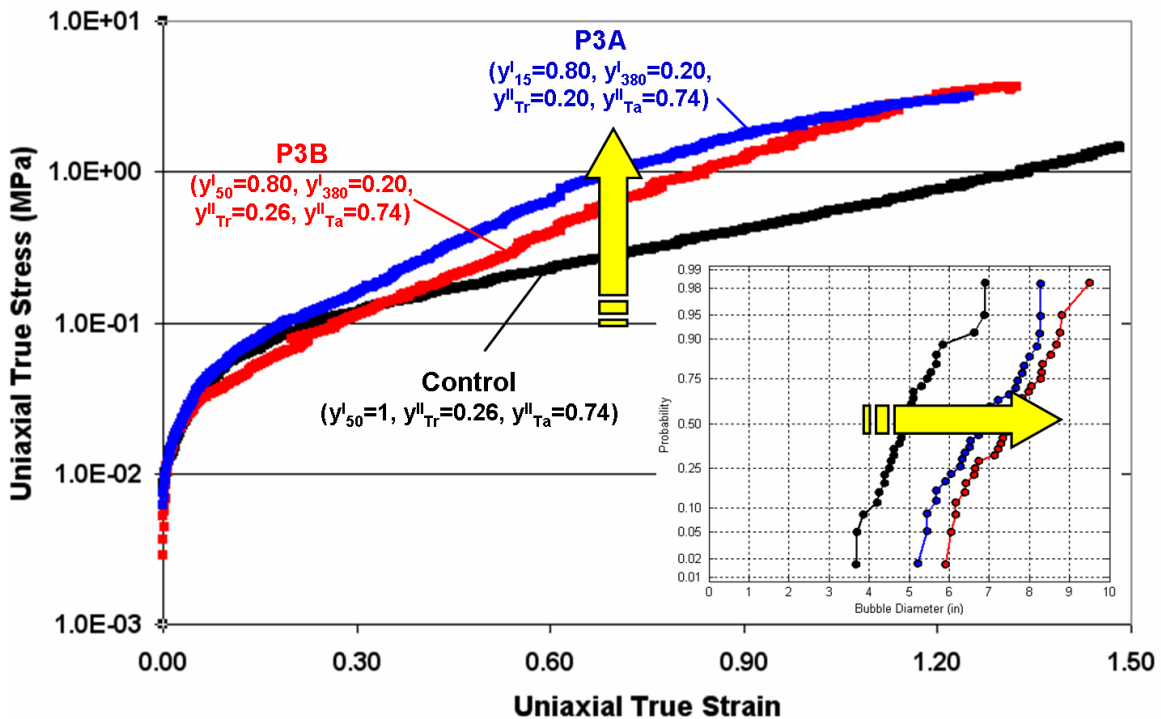
Figure 7.13. Uniaxial σ_U^T vs ε_U^T response comparison for control, P3A, and P3B. Correlating colors are used to compare the σ_U^T vs ε_U^T constitutive behaviors to their resulting bubble diameter normalized probability distributions. Yellow arrows indicate increased bubble diameter with increased strain hardening.

prototypes encoded with a *, represents a gum base and gum that had their extensional and *in-vivo* properties studied but have not yet been mentioned in this work. The value for P3b* is important because it has the highest strain hardening parameter but much smaller bubble diameters than the rest of the P3 prototypes, indicating a transition from plastic flow stabilization to fracture inition. Additionaly, the multiple values for the control (C1-C3) were shown because their respective mean bubble diameters were used to normalize mean bubble diameters for prototypes 1 - 3 for the development of a normalized mean bubble diameter (NMD) vs SHP mechanistic model in Figure 7.14. Such normalization was required for proper comparison between successive gum prototypes due to the author's bubble blowing ability enhancement.

Table 7.1. Uniaxial exponential hardening fitting constants for prototype constitutive behaviors and their correlation to *in-vivo* bubble performance.

Prototype	y_i^I	y_j^I	y_{Tr}^{II}	y_{Ta}^{II}	σ_o (MPa)	SHP^a(k)	$D_{mean}(in)$	$D_{90th}(in)$
P2-VAVL	$y_{VAVL}^I=1$	$y_{50}^I=0$	0.26	0.74	$0.03 +/- 0.01$	$0.77 +/- 0.11$	1.67	2.11
P1A	$y_{50}^I=1$	$y_{380}^I=0$	0.33	0.74	$0.05 +/- 0.01$	$1.36 +/- 0.01$	2.01	2.97
$P1a^{*b}$	$y_{50}^I=0.95$	$y_{380}^I=0.05$	0.39	0.00	$0.02 +/- 0.01$	$1.45 +/- 0.07$	2.74	3.98
P2-1/2VAVL	$y_{VAVL}^I=0.50$	$y_{50}^I=0.50$	0.26	0.74	$0.05 +/- 0.01$	$1.54 +/- 0.05$	2.91	3.55
P1B	$y_{50}^I=0.975$	$y_{380}^I=0.025$	0.33	0.74	$0.05 +/- 0.01$	$1.63 +/- 0.04$	2.61	3.44
$P1a^{*b}$	$y_{50}^I=0.925$	$y_{380}^I=0.075$	0.39	0.00	$0.03 +/- 0.01$	$1.66 +/- 0.05$	2.76	3.58
P3-VAVL	$y_{VAVL}^I=1$	$y_{50}^I=0$	0.09	0.74	$0.12 +/- 0.01$	$1.72 +/- 0.42$	2.75	3.70
$C2^{*b}$	$y_{50}^I=1$	$y_{380}^I=0$	0.26	0.74	$0.06 +/- 0.01$	$1.77 +/- 0.01$	4.53	5.45
P1C	$y_{50}^I=0.95$	$y_{380}^I=0.05$	0.33	0.74	$0.04 +/- 0.01$	$1.79 +/- 0.02$	3.09	4.55
P1D	$y_{50}^I=0.925$	$y_{380}^I=0.075$	0.33	0.74	$0.05 +/- 0.01$	$1.83 +/- 0.04$	3.52	4.63
C1	$y_{50}^I=1$	$y_{380}^I=0$	0.26	0.74	$0.06 +/- 0.02$	$1.90 +/- 0.07$	3.07	4.17
C2	$y_{50}^I=1$	$y_{380}^I=0$	0.26	0.74	$0.06 +/- 0.01$	$2.08 +/- 0.04$	4.18	4.86
C3	$y_{50}^I=1$	$y_{380}^I=0$	0.26	0.74	$0.06 +/- 0.01$	$2.20 +/- 0.04$	5.01	6.63
P2B	$y_{15}^I=0.7$	$y_{380}^I=0.3$	0.26	0.00	$0.04 +/- 0.01$	$2.63 +/- 0.04$	5.12	6.72
P2A	$y_{15}^I=0.7$	$y_{380}^I=0.3$	0.26	0.74	$0.03 +/- 0.01$	$3.70 +/- 0.68$	5.52	6.99
$P3a^{*b}$	$y_{15}^I=0.6$	$y_{380}^I=0.4$	0.26	0.74	$0.06 +/- 0.01$	$3.80 +/- 0.42$	6.92	8.31
P3B	$y_{50}^I=0.8$	$y_{380}^I=0.2$	0.26	0.74	$0.03 +/- 0.002$	$4.23 +/- 0.67$	7.49	8.76
P3A	$y_{15}^I=0.8$	$y_{380}^I=0.2$	0.20	0.74	$0.04 +/- 0.01$	$4.35 +/- 0.35$	6.85	8.25
$P3b^{*b}$	$y_{40}^I=0.8$	$y_{380}^I=0.2$	0.29	0.74	$0.05 +/- 0.01$	$4.75 +/- 0.64$	5.59	6.99

a.) K-values are placed in ascending order in this table. b.) These gums were tested in addition to the other prototypes but not mentioned in the body of this document.

Figure 7.14 shows normalized mean diameter (D_i^j/D_C^j) plotted vs uniaxial strain hardening parameter (k) with errors bars representing one standard deviation of error. Normalized mean diameter (NMD) is formulated so that all gums (i) are normalized by the mean value of the control from their *in-vivo* testing event (j). Figure 7.14 shows a quantified correlation between uniaxial strain hardening displayed in gum base and biaxial ductility demonstrated in *in-vivo* bubble performance. The figure displays three distinct regions. The first region is between k value boundaries of 0 and ∼1. This region represents an unstable plastic flow region for gum base. Gum bases with k-values in this region have an inflating bubble that is severely unstable and is very susceptible to minor localized plastic strains. The next region contains a sharp initial rise in bubble diameter at an SHP (k) of ∼1 which follows an S-curve until a plateau at a k-value of ∼4. The sharp rise is most likely a result of there being a minimum k-value for plastic flow stabilization and bubble diameter increase. The saturation of the NMD *vs* SHP behavior is likely are graphical respresentation of the initiation of new failure mechanism unmediated by plastic flow stability. Finally, the third region is represented by SHP values greater than ∼4.5. This is most like a fracture control mediated region where the gum bubble diameter is limited by talc protrusion resulting in matrix dewetting or talc fracture.

The S-curve mechanistic behavior was described using the logistic function [120] shown in Equation 7.1. Gum complex viscosity was examined by a Spring 2008 MSE 390 Materials Design undergraduate student team and found to be insignificant. Therefore, strain hardening parameter is taken as the reasonable parameter to use for the mechanistic description of *in-vivo* bubble performance. In doing so, the logistic function fits the data seen in Figure 7.14 with a sum squared error value of 0.3. The fitted logistic function parameter were $a = 1.4$, $m = 34$, $n = 141$, and $\tau = 0.3$. There are likely more complex mechanisms dominating mean *in-vivo* bubble
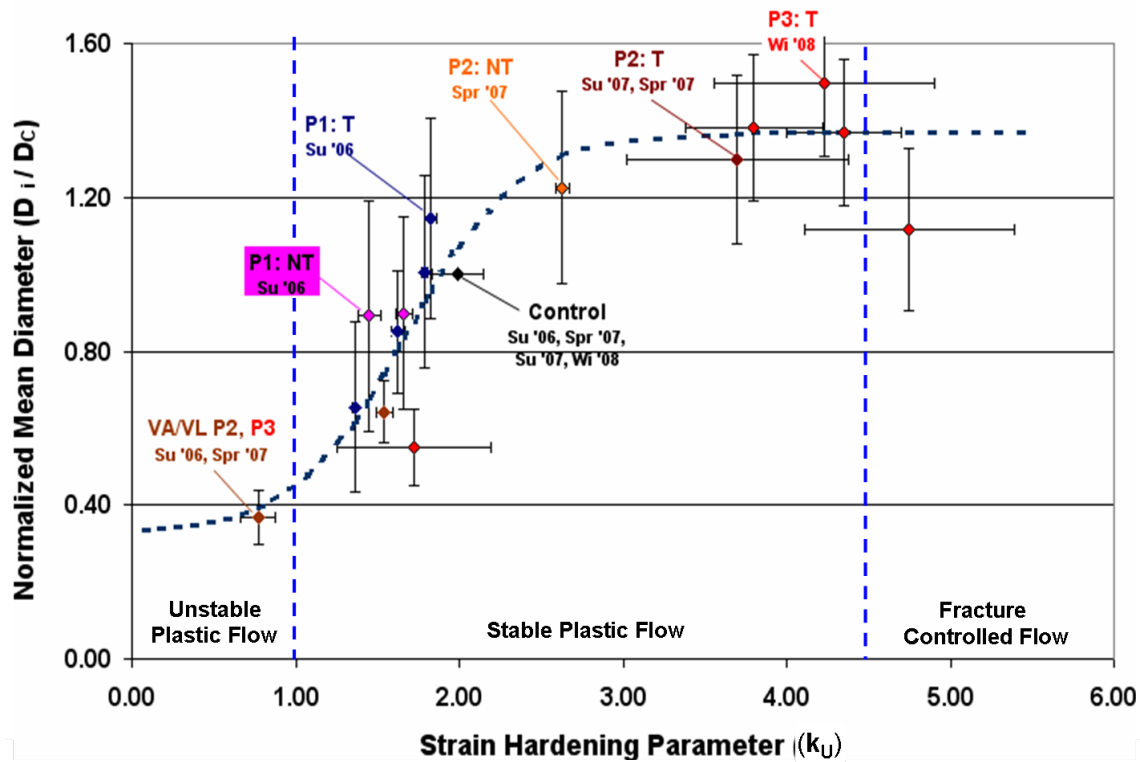
Figure 7.14. Normalized mean diameter (D_i/D_C) vs uniaxial strain hardening parameter (SHP, k_U) presented with one standard deviation of error bars. At $k_U < 1$, bubble flows are very unstable and susceptible to minor localized plastic flows. At $1 < k_U < 4$, flows ramp up to ideal bubble stability (k_B=1) stability. At $4 < k_U$, biaxial flows start getting too much strain hardenign it becomes detrimental.

performance than can be described by this model however the model appears to describe the behavior sufficiently well.

$$NMD = \frac{D^i}{D^i_c} = a\frac{(1+mexp(-k_U/\tau))}{(1+nexp(-k_U/\tau))} \tag{7.1}$$

One example fracture mechanism which may be causing the transition from plastic flow stability controlled to fracture mediated flows is shown in the polarized optical micrograph in Figure 7.15. This micrograph shows an inflated HBSS membrane with a number of talc particles

spanning its thickness. Protruding talc particles were imaged with optical light polarization knowing that the crystalline structure of talc would unpolarize transmitted light, resulting in detection if it were protruding *through* the membrane. This observation was important because HBSS control bubbles were inflated up to 3 to 4 inches, or almost to failure for this study, and thus it suggests possible bubble size fracture limitations resulting from the presence of talc *in unstable plastic flows* or upon the achievement of maximum biaxial strains (i.e. film thickness becomes comparable to talc particle size). This design centered on and proved the assumption that stable uniform biaxial plastic flow was not initially hindered by the presence of talc in gum base but the strain hardening parameter plateaus suggest further consideration of talc as a fracture limiter.
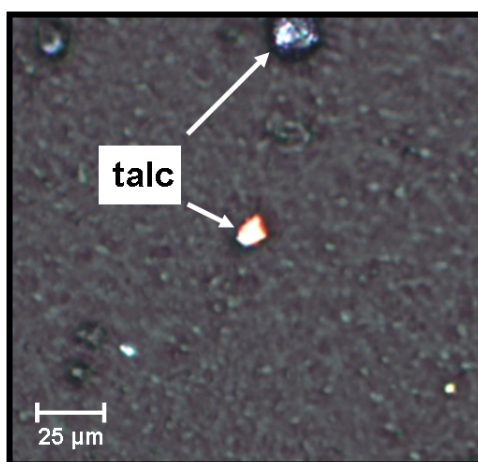
Figure 7.15. Transmission optical micrograph of HBSS control inflated film with polarized light. White crystalline features are talc particles spanning the membrane.

7.3.2. Biaxial Extensional Flow

Biaxial extensional flow characterization was performed on Dr. Shull's biaxial inflation apparatus for prototypes 2 and 3, and their respective controls. Biaxial inflation characterization

of P2A and the control indicate ideal biaxial strain hardening ($k_B = 1$) which is sustained till larger biaxial true strains for P2A (until $\sim$2) than for C2 (until $\sim$1.8). This result indicates a stabilizing effect of P2A caused by the high MW portion increasing uniform ductility before plastic localization causes failure, but unfortunately this result does not resolve any differences in exponential strain hardening between the two bubblegums. Such a resolution of differences are needed to mechanistically confirm previously shown *in-vivo* results.

A literature review revealed the maximum achievable volumetric flow rate for this apparatus, 1,000 ml/hr, to be at the very low end of average human breathing rates which are between 600 and 1.2×10^4 mL/hr [121]. Since, the apparatus flow rate is on the low end of human breathing rates, not exhalation inflation rates which are likely larger for the inflation of gum, it is most likely a good inference that this apparatus does not achieve the rates required to resolve the constitutive behavior of *in-vivo* inflation. The results from P2 are real but not definitive proof of the stabilization of biaxial flows with bimodal PVAc design of gum base.

A lower volumetric flow rate than used during *in-vivo* inflation most likely results in less biaxial strain hardening, less flow resistance, and premature failure. *In-vivo* inflations tend to drastically fail but the low volumetric flow rate failures tend to be a result of the inflated cud leaking through fissures caused by gum fold separation (see Figure 7.17). Additionally, flow behavior wasn't seen to drastically change with flow rate for the third prototype suggesting higher, more human-like flow rates were needed for the appropriate characterization of gum prototypes.

With this in mind, a larger membrane holder was developed by an Engineering Design and Communication team which could hold and inflate $\sim$1.5 mm thick membranes. This holder was set-up in line with the MKS baratron and used to measure pressure during the inflation of 10 min
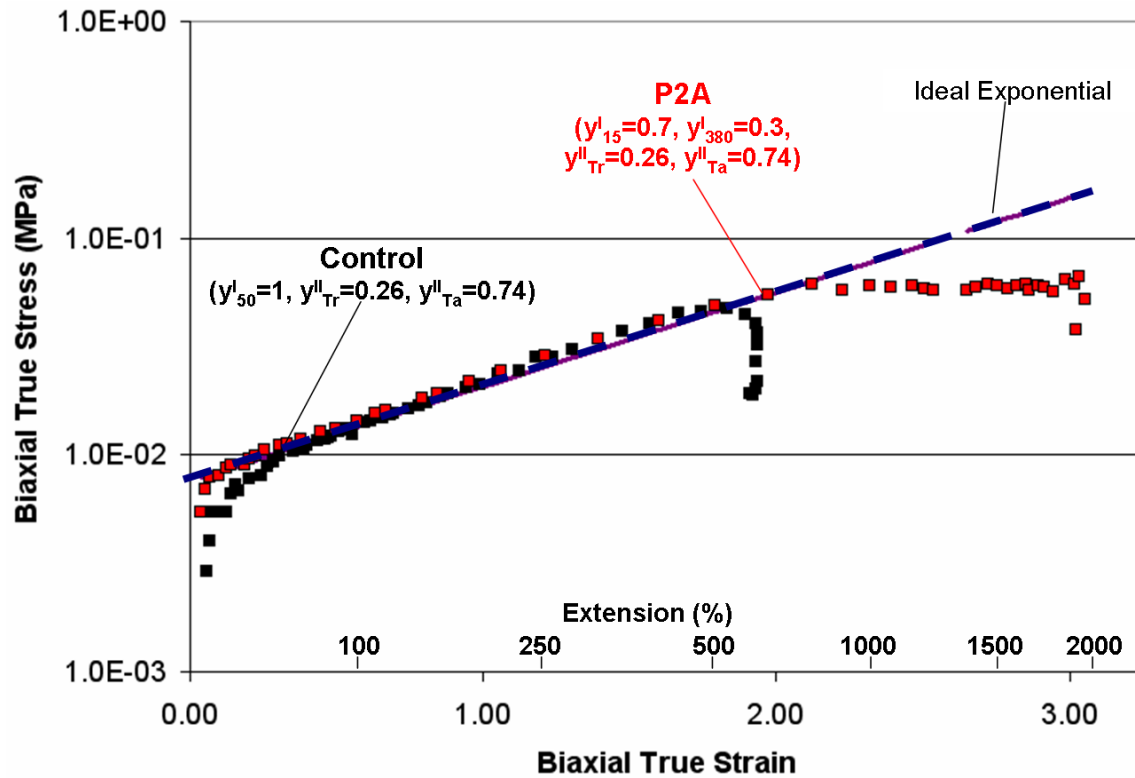
Figure 7.16. Biaxial strain hardening behavior of P2A and C2 gums at 22 °C and a volumetric flow rate of 1,000 ml/hr. Although not demonstrating excessive strain hardening above the ideal, the P2A does show increased continuous strain hardening that elongates its achieved plastic strain.

mouth chewed gum samples (P3B, C3, and HBMax). Samples were rolled out in warm water, mounted and clamped on the holder, and inflations were recorded with the LabView 7.0 [122] computer screen visible in the background. The same equations used for the calculation of biaxial true stress and biaxial true strain for this inflation apparatus in Chapter 3 were applied for these experiments as well. Pressure and and deflection are synchronized by measuring deflection and recording the time on the LabView screen then retrieving the corresponding pressure data from the saved baratron output file. One EDC group member inflated each of the bubble with as consistent a profile as possible.
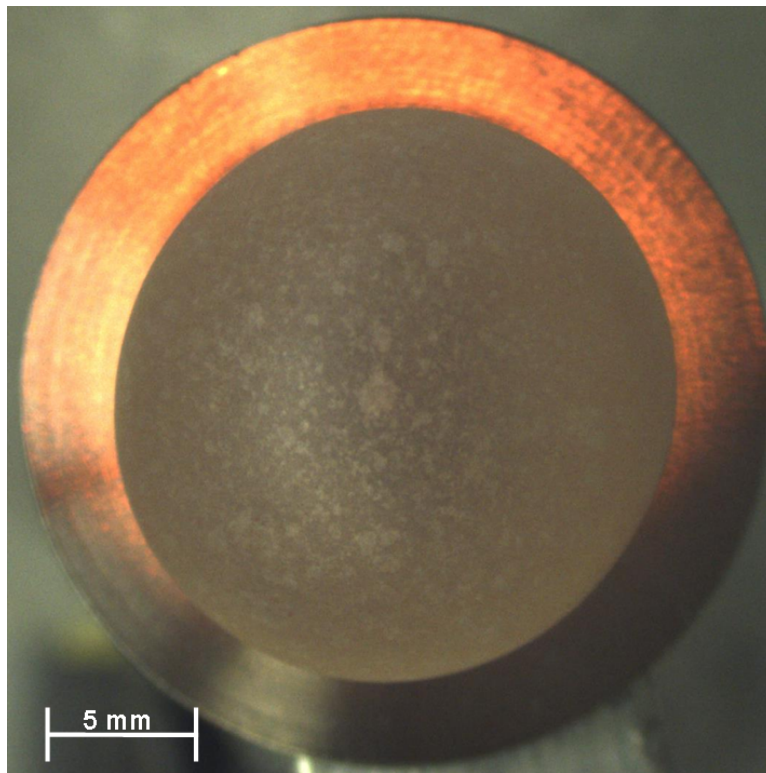
Figure 7.17. Top view of biaxially inflated gum bubble showing small domain formation which is the primary mechanism for instrumented failure.

The average results from the best 3 out of 5 tested membranes from the above procedure are displayed in Figure 7.18. A distinct decreasing exponential behavior from P3B - HBMax - C3 is demonstrated as lines of decreasing slope on the semi-log plot. A representative graph of the reproducibility of the experiments is inlayed in this graph for the P3B prototype. There appears to be some variance in the early strain region but this is most likely a result of measurement error, not material effects, because the camera used had a very large field of view which prevented accurate low strain measurement. This is the same reason for a lack of data existence below biaxial true strains of 1. Thus, this curve is more likely representative of the nonlinear biaxial plastic behavior of these materials.
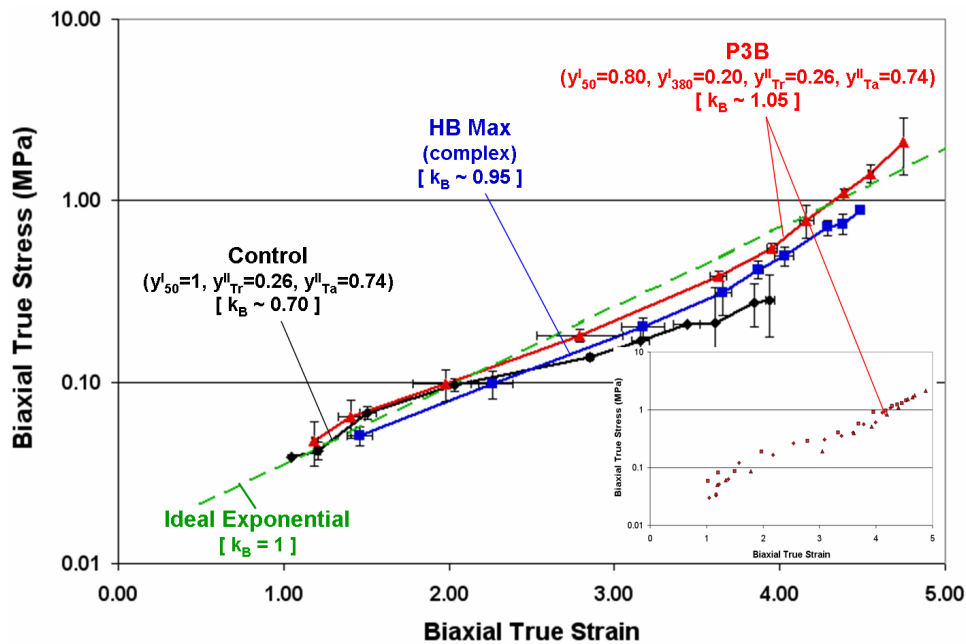
Figure 7.18. Biaxial plastic true stress vs true strain behavior of C3, P3B and HB Max inflated films. A plot of experiment reproducibility is shown inlayed for P3B.

The exponential behavior of the curves in Figure 7.18 was analyzed using the general expression presented in Chapter 2. Straight lines were fit to the data and found P3B, HBMax, and the Control all to have initial yield values (σ_o) of $\sim$0.02 MPa and biaxial strain hardening parameters (k_B) of 1.05, 0.95, and 0.70, respectively. This is significant because theory says that optimal strain hardening for the prevention of plastic flow localization in balanced biaxial flow should occur at a value of 1. Theoretically, values less than this should be unstable and values greater than this should be more stable. Thus, a scientific characterization has been completed which establishes strong evidence for a simple bubblegum like P3 outperforming the control and a complex bubblegum such as HBMax in stabilization of balanced biaxial flow as is inherent in inflated gum bubbles.

7.3.3. Uniaxial vs Biaxial Extensional Flow

The biaxial inflation technique was used to complete biaxial characterization of the P2A bubblegum for the comparison of uniaxial gum base and biaxial gum strain hardening behaviors. A qualitative relationship between uniaxial strain hardening and biaxial strain hardening is observed in Figure 7.19. In tensile flows, P2A's gum base clearly yields at a true stress similar to the control's but is seen to have a much greater strain hardening ($k \approx 3.7$ vs $k \approx 2.0$, respectively). This implies that polymer constitutive behaviors which deviate above the ideal exponential in uniaxial flows promote longer strain hardened and stabilized biaxial flows. This phenomenon is seen in Figure 7.19 where P2A biaxially strain hardens biaxially than the control and achieves a 60% larger true strain. Thus, excess uniaxial strain hardening promotes biaxial strain hardening which stabilizes biaxial flow and increases biaxial stretch ductility.
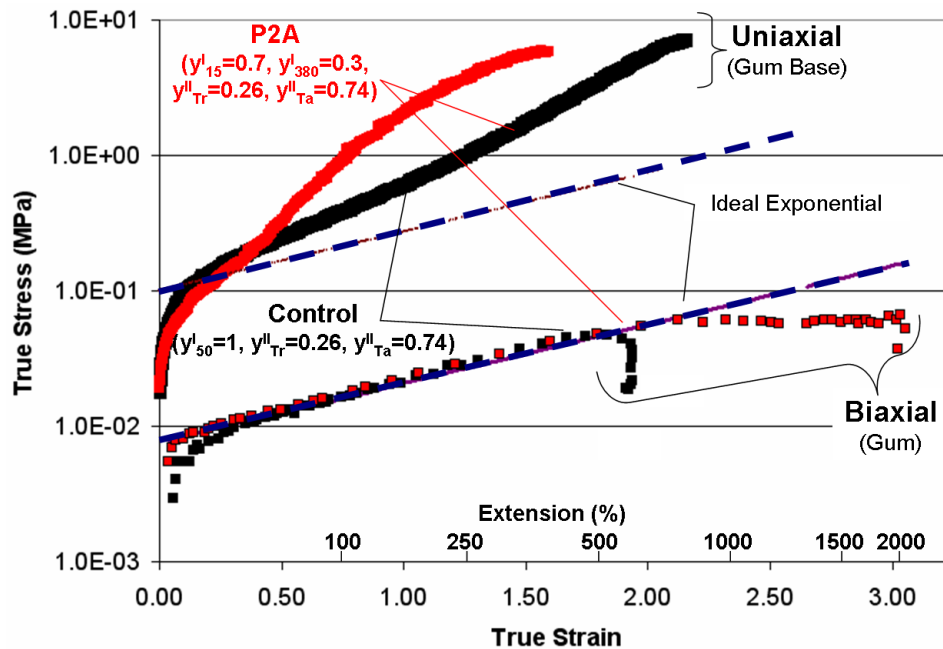
Figure 7.19. Comparison of uniaxial (0.006 s^{-1} and biaxial (1000 mL/hr) strain hardening behavior of P2A and the control gum base and resulting gums at 22 °C, respectively.

CHAPTER 8

Parametric Model for Fourth Generation Bimodal PVAc Gum Base Design

The success of the third generation bubblegum prototype provided motivation for the expansion of the parameterized HDPE model described in Chapter 4. Equivalent strains were extracted and parameterized for bimodal PVAc gum prototype (P1-P3) maximum bubble diameters and added to the parameterized data set for a generalization of the previously discussed parametric model. The generalized parametric model was heavily weighted to the region of highest equivalent strains and modeled using DesignExpert 7.1.5 [123] to regression fit the data with an adequate model for the design of a fourth generation bimodal PVAc gum base prototype.

8.1. Parametric Model Development

8.1.1. Bimodal PVAc Equivalent Strains

Bimodal PVAc prototype equivalent strains were calculated from maximum *in-vivo* bubble diameter data using relationships similar to those employed for the measurement of biaxial true stress and biaxial true strains in Chapter 3. Equivalent strain or bubble equivalent thickness reduction (BETR) was calculated using Equation 8.1. Initial gum cud thickness (t_o) was measured by chewing a 7.00 +/- 0.02 g piece of gum for 10 minutes and then simulating as if it were to be blown into a bubble. The cud thickness was measured with a micrometer to be on average $\sim$0.75 mm. Inflatable cud volume was then measured by submerging it in a graduated cylinder

and recording the height change in the meniscus. The bubblegum chunk for the control HBSS formula resulted in a cud volume of ~ 2.1 cm^3. The same measurement was done on the blown portion of the cud by simulating blowing, stripping the cud from the mouth before inflation, and submerging the pre-inflated cud in a graduated cylinder, $\sim 40\%$ of the cud is inflated during bubble blowing. From there, the surface area of the inflated sphere was found by assuming a spherical geometry and bubble equivalent thickness reduction was calculated.

$$BETR = ln\left(\frac{A_{bubble}}{A_{tongue}}\right) = ln\left(\frac{A_{sphere}}{V_{inflated}/t_o}\right) \qquad (8.1)$$

Another method involving the normalization of a prototype bubble diameter with a HDPE equivalent true strain occupying the same parameterized location was considered for the conversion of bubble diameters to strain values but was abandoned when the method described above provided bubble equivalent strains consistent with data collected from the HDPE literature. More specifically, the above method calculated equivalent thickness reductions of between 4 and 5.32 for inflated prototype bubblegums which overlay well with previously established parameterized HDPE trends. Additionally, the values utilized are likely representative of the population because this procedure was first implimented in the spring of fall of 2006 for the calculation of equivalent biaxial true strains. At this point, the author had yet to become the primary bubble inflator for this research and thus was still representative of the population (see Figure 7.1).

8.1.2. Generalized Parametric Model

A 2-parameter D-optimal design was performed on a generalized data set, including bimodal PVAc gum data and new HDPE data [124–126], was completed using DesignExpert 7.1.5.

Prototypes 1, 2, and 3 as well as HDPE data with the highest equivalent strains were weighted to best model the high biaxial strain region. Additional, non-bimodal data points were used to pin the model to specific values on the MWR- and HMW fraction-axes. The HMW fraction-axis was pinned (at 0, 20, 60, and 80 wt% HMW fraction) to the equivalent thickness reduction of the HBSS control (MWR = 1 or log(MWR) = 0) because low molecular weight (LMW) and high molecular weight (HMW) magnitudes are equal on this axis making HMW fraction a constant parameter here. The model was not pinned at a MWR of 1 and HMW fraction of 100 wt% because a model could not be found without a significant lack of it when doing so. The MWR-axis was pinned at a MWR value of 7.6 and HMW fraction of 0 to the value of the control as well.

An analysis of variance (ANOVA) of the above data set revealed a significant cubic model with a non-significant lack of fit parameter. A response surface for this model is shown in Figure 8.1 with a logarithmic MWR axis and linear HMW fraction axis. Data points which are under predicted by the model appear above the surface in red and data points which are over predicted by the model appear below the surface in pink. A traditional color coding of the response surface is shown where a dark blue to yellow color scheme indicates increasing equivalent thickness reductions, therefore biaxial strain. A large dip in the model is demonstrated at high MWRs and a HMW fraction of 0 which can be correlated to a dominance of the viscosity by a low molecular weight polymer containing unstable plastic flow. This behavior is analagous to that described for low uniaxial strain hardening parameters (k<3/2) in Figure 7.14. Additionally, the model is shown pinned on the axes are predefined for the constraint of those values.

A two-dimensional contour plot of the above response surface is shown in Figure 8.2. The color scheme is a little more apparent here indicating a rise in thickness reduction values in the
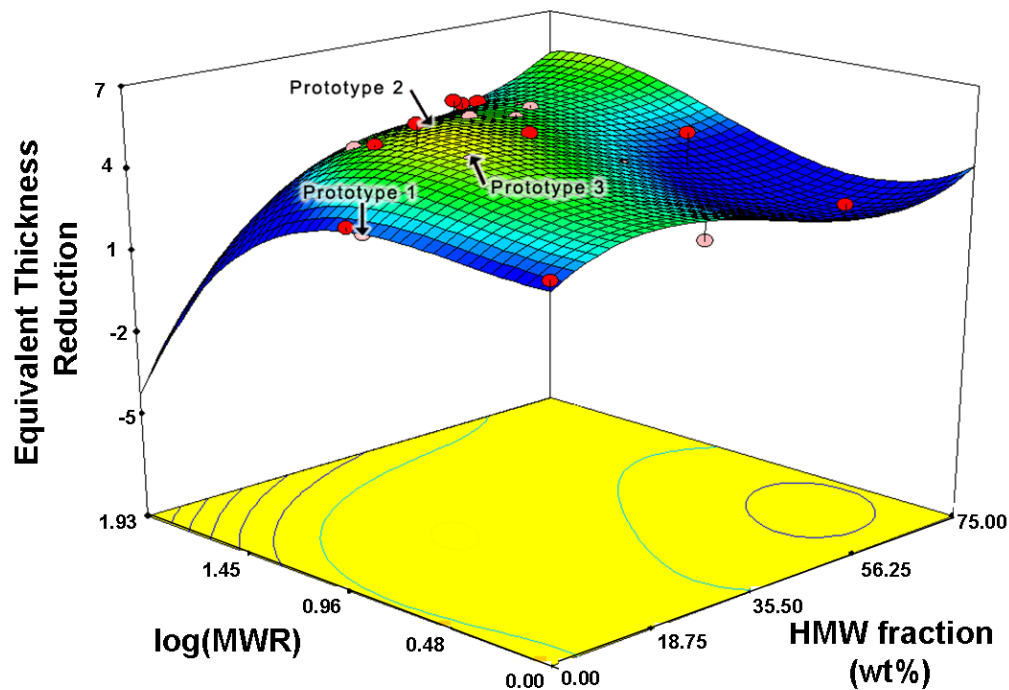
Figure 8.1. Cubic polynomial equivalent thickness reduction response surface for general parameterized bimodal MWD ductility performance for fourth generation prototype design. Red circles correspond to data points above the model response surface fit while pink circles correspond to data points below the response surface fit.

region containing prototype 2 and 3 as well as the highest HDPE strain values (MWR ~10, HMW fraction ~20wt%). These regions are more weight as indicated by the number next to each of the red circles. The number represents a multiplier for each of the red circles which represents a point in the data set.

8.1.3. Model Adequacy

Normal probability are often useful for checking model adequacy because they check the underlying assumption that the data being modeled is normally distributed. This is important because the D-optimal program in DesignExpert 7.1.5 assumes this when calculated model significance
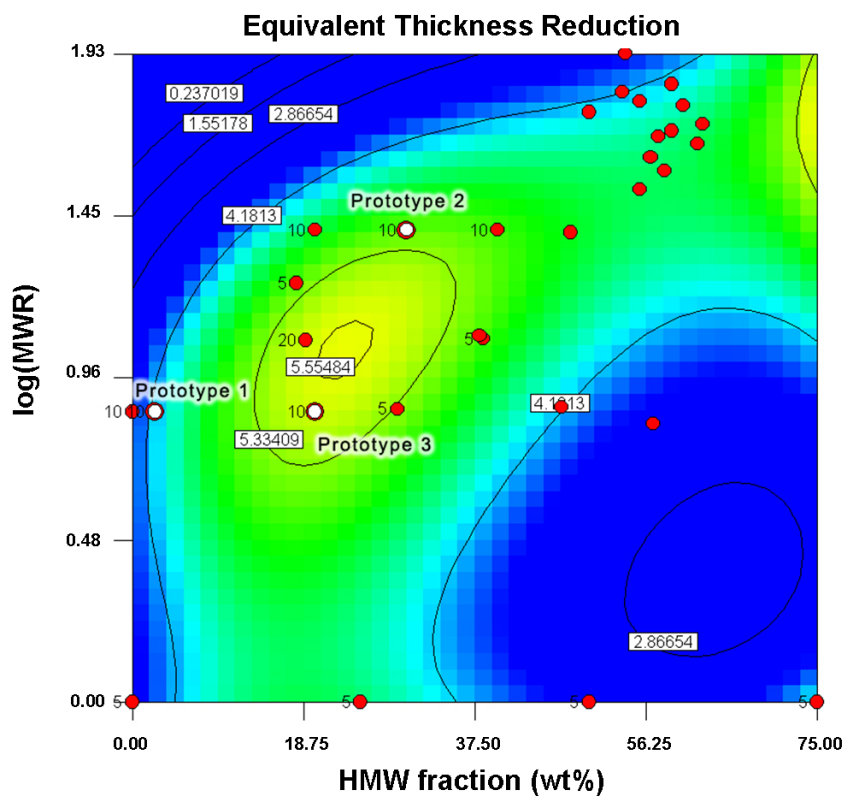
Figure 8.2. Two-dimensional contour plot representation of the equivalent thickness reduction response to MWR and HMW fraction (wt%). Numbers next to circles correspond to more heavily weighted points for best definition of the model near previously designed prototypes and highest HDPE equivalent thickness reductions.

in during ANOVA. An examination of Figure 8.3 shows the assumption to be satisfied because the plot resembles a straight line where residual errors relatively centered around zero. Additionally, prototype 3 gums are shown to have residuals close to zero suggesting their effect on the model is large whereas the values for P2 and P1 bubblegums have less of an effect. Experimentation with weight led to insignificant gains in this respect.

Ultimately, a check of the residuals vs predicted value plot is also important for model adequacy. The model is shown relatively structureless and therefore a good fit. Weighting effects
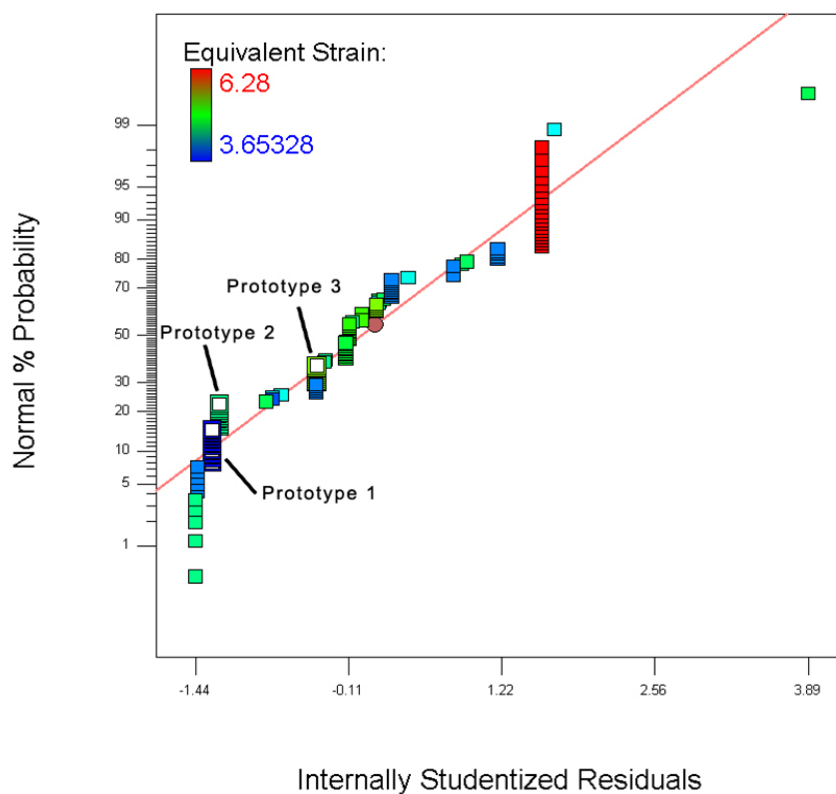
Figure 8.3. Normal probability plot vs residuals for checking cubic model adequacy. Prototype equivalent strains are indicated by white points while multiple residual points are representative of weighting.

are apparent where prototypes 2 and 3 and high strain HDPEs are shown the most structureless around the zero residual value which was expected. One outlier is shown at a low predicted value but is not significant to the design region of interest.

8.2. Fourth Generation Prototype Design

The design of a fourth generation prototype is shown in Figure 8.5. The region of greatest thickness reduction (MWR $\sim$10, HMW fraction $\sim$20wt%) is illustrated to lay within the acceptable viscosity constraint via a projection (red arrow) of the local maxima onto a constrained

Figure 8.4. Residuals vs predicted model values plot for checking cubic model adequacy. Numbers next to points indicate a weight of that data point during model development.

contour plot at the base of the response surface. Therefore, optimal parameters for the maximization of equivalent thickness reduction were predicted by Design Expert 7 to lay at a local maxima log(MWR) of 1.05, or a MWR ~11, and a HMW fraction of ~23 wt%. This corresponds to a HMW of 380 kg/mol placed into a 35 kg/mol PVAc gum base. This local maxima is predicted to yield an equivalent thickness reduction of 5.6 which, via the basic model used for the prediction of bimodal PVAc gum equivalent strains, corresponds to an maximum bubble diameter of ~12 inches. This predicted bubble diameter corresponds to a 40% 95th percentile bubble diameter increase over HB Max. A value for the predicted bubble diameter increase at

the mean formulated by assuming the normal probability distribution in Figure 7.11 remains consistent between trials. Therefore, in knowing that P3 originally bests HB Max by 14% and 22% on the mean and 95th percentiles we can use this calculate to estimate a mean bubble diameter increase for the fourth generation simple bimodal bubblegum design over that of the complex HBMax of ~26% to mean bubble diameter of ~9.3 inches.
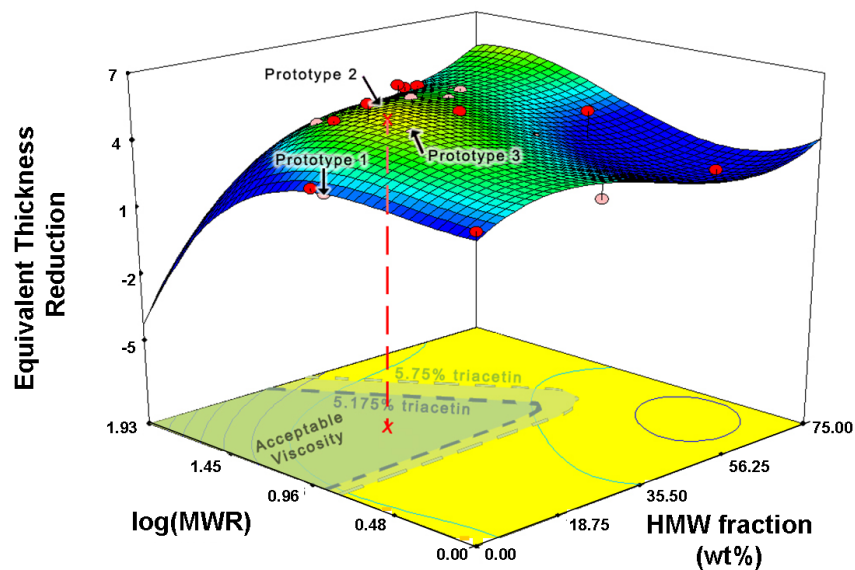
Figure 8.5. Fourth generation prototype design response surface with overlayed local chew viscosity model contours. Dark green boundary represents y_{Tr}^{II}=0.23 and light green boundary represents y_{Tr}^{II}=0.26.

Now that the parameterized model has predicted the performance increase expected for the fourth generation prototype it is important to calculate the amount of triacetin and filler required to maintain its chew viscosity comparability to the control bubblegum (690 Pa*sec). This was done using the global chew viscosity model outlined in section 5.2.3. Model endpoints and interaction parameters were calculated from the functions presented in that section while the second sublattice compositional parameters for triacetin (y_{Tr}^{II}) and talc (y_{Ta}^{II}) were varied. The

global chew viscosity model predicts a comparable chew viscosity to that of the control at a triacetin content of 0.255 $(= y_{Tr}^{II})$ and a talc content of 0.73 $(= y_{Ta}^{II})$.

CHAPTER 9

Conclusions

A science-based systems engineering approach was utilized for the design and optimizaton of gum base strain hardening. Strain hardening was optimized by broadening the molecular weight distribution of the PVAc gum base component to meet parametric requirements established in the well studied PE system. Shear rheological tests were completed to develop a chew viscosity model to constrain gums to acceptable chew viscosities. Tensile tests were completed to validate molecular distribution effects on the strain hardening of designed gum base prototypes. Additionally, biaxial inflation tests were completed to study the molecular architectural effects of neat styrene-isoprene-styrene (SIS) triblock and styrene-isoprene (SI) diblock copolymer blends, neat PVAc bimodal versus unimodal polymers, and designed bubblegums. Finally, optical microscopy studies and theoretical thermodynamic calculations contributed to the design approach.

9.1. Bimodal PVAc Gum Base Designs

A third generation prototype (P3B) was designed for a bimodal PVAc molecular weight ratio (MWR) of 7.6 and high molecular weight (HMW) fraction of 20 wt% using the parametric and chew viscosity model. This bubblegum outperformed HBMax, the currently best performing commercial bubblegum, by 14% and 25% at the mean and 90th percentile diameters, respectively. This provides definitive proof that a simple microstructure with a scientifically designed bimodal PVAc MWD can outperform an empirically developed, complex bubblegum such as

Hubba Bubba^{TM} Max. Figure 9.1 shows maximum bubble diameters as high as $\sim$11 inches were achieved with this simple bubblegum.

Figure 9.1. Simple bubblegum prototype inflated into an 11 inch diameter bubble.

The same prototype exceeded its control's *in-vivo* bubble diameter by 50% and 40% at the mean and 90th percentile, respectively. This was completed by first showing that poly(vinyl acetate) made-up the continuous and thus most advantageous designable phase for governing the constitutive flow behavior and chew properties of current bubblegum. A parametric PE-based molecular weight design of the PVAc phase of gum base was implemented with viscosity constraints based on non-ideal Redlich-Kister complex viscosity models to design a high performance bubblegum having a simplified microstructure.

Complex viscosity models were developed which constrained prototypes within 15% of their designed value and were instrumental to the design of high performance bubblegum prototypes. For a little perspective, this value is half that of the available error, 33%, for a design in the middle of the acceptable chew viscosity constraint (350-700 Pa*sec). Even more so, designs which were predicted within the boundaries of the model, that is gums that do not require extrapolation, were found to be predicted within ∼5% of their designed value.

Linear viscoelastic characterization of gum at 37 °C for the development of a chew viscosity model revealed a strong power-law dependence on angular frequency for both gum base and gum. This observation is combined with the fact that gum complex viscosity (η^*, Pa*sec) changes minimally at chew times greater than 5 minutes, suggesting all sugar dissolution is complete at this time and that gum base dominates cud properties. From here, non-ideal Redlich-Kister polynomials were shown to effectively model quantified differences in bubblegum complex viscosity resulting from gum base PVAc molecular weight, PVAc molecular weight distribution (MWD), talc ($Mg_3Si_4O_{10}(OH)_2$), and triacetin ($C_9H_{14}O_6$) compositional variations.

It was found that linear viscoelastic characterization of gum must be done carefully because it has been noted that gum properties tend to rise with time spent mounted on the rheometer suggesting edge drying effects. A humidity jacket can be used to diminish these effects but do not totally prevent this occurence. Therefore, gum characterization procedures should be consistent for the most comparable values; this is the most likely source of error in the chewability model.

PE bimodal molecular weight advantages have also been demonstrated in neat bimodal PVAc blends which are of the same bimodal PVAc characteristics as that of the third generation

gum base suggesting the underlying polymer phyics governing pure polymer flow are transferable to the complex gum base, thus gum, to increase bubble diameter.

Excess strain hardening in gum base uniaxial flows has been shown to promote ideal strain hardening in biaxial gum flows up to a point where fracture controlled mechanisms may inhibit further bubble diameter increases. The data suggests that the optimal strain hardening for bubble size occurs at a uniaxial SHP (k) value of $\sim$3.7 for a constant true strain rate of 0.006 s^{-1} and temperature of 22°C. This result is consistent with the literature in that it supports the notion that uniaxial flows harden more than biaxial, therefore supporting the notions initially held when entering into this design.

Hansen solubility parameters proved themselves to be effective at assessing the partitioning of gum base phase relations. They predicted the immiscibility of PVAc and PIB as well as the plasticization of the gum base with triacetin. They also provided insight into the interaction of the PVAc portion of the gum base with added flavor components suggesting their key role in complex viscosity determination as well.

9.2. Conceptual Prototype Designs

9.2.1. SIS/SI Block Copolymer Blends

Conceptually, SIS/SI triblock/diblock copolymer blends demonstrated potential benefits for biaxial strain hardening tunability in gum base with biaxial strain hardening parameters, k_B, as high as 0.95. Such a high k-values suggests this polymer system offers encouragement for the potential future design of novel gum bases and definitely warrants more study. Additionally, SIS/SI blend showed a tunability based on the amount of diblock added which would be beneficial to future gum bases because their properties could be tailored to their function. In other

words, high SIS/SI ratio blends would be used for bubblegums while low SIS/SI ratio blends would be used for chewing gums.

SIS/SI block copolymer blends also displayed little volumetric flow rate sensitivity in the biaxial inflation experiment and had very good strain reproducibility in general suggesting little sensitivity to membrane surface defects. This is most likely due to the material's low modulus but elastic character. However, such membrane elasticity has shown increased likelihood for peeling of the membrane holder during inflation therefore resulting in increased difficulty while analytically interpreting measurements.

9.2.2. VAVL Block Copolymer

Vinyl acetate - vinyl laurate (VAVL) block copolymer gum bases demonstrate very limited uniaxial strain hardening as a result of its laurate side chains acting more like molecular spacers than entanglement enhancers. This results in very poor properties for a bubblegum but might be more useful as a replacement in chewing gum formulations because of its rubbery nature at room temperature. A two sublattice chew viscosity model treating VAVL and 50 kg/mol PVAc as substitutional elements and triacetin, talc, and vacancies as interstitial elements has been developed for utilization in future gum designs. This model performs well and has been shown to predict chew viscosity values to $\sim$3% of design values.

CHAPTER 10

Suggestions for Future Work

In this research, bubblegum has proven itself as a formidable material for this systems designer. This work has led to countless new ideas ranging from the abstract to the interesting. For the sake of the reader, the author will try to limit suggestions for future work to the latter.

First and foremost, broadening the molecular weight distribution of the PVAc portion of gum base should be further investigated. A good start would be with the fourth generation prototype to validate the parametric thickness reduction model developed in Chapter 8. A broad understanding of the bimodal molecular weight concept by further developing the design space would help in a number of ways. First of all, a bimodal molecular distribution has tunable properties in the same way as the SIS/SI copolymer did. Therefore, bimodal PVAc concepts could be applied to simplify a wide range of currently utilized gum bases to one molecular weight ratio (MWR) PVAc system, most likely ≥ 25. Such a high MWR bimodal gum base could be developed to exhibit chew viscosity properties of chewing gum at low HMW fractions and bubblegum properties at HMW fractions. These properties would most likely have to be modeled for the proper application of this concept requiring the use of non-ideal Redlich-Kister polynomials for the description of complex material behavior.

Since some of the bubblegum prototypes show excess strain hardening being detrimental to bubble size diameter it would be interesting to test these gums for their adhesion properties because adhesion one application where one can never have too much strain hardening, as long as chew viscosities are still acceptable. For this, an implimentation of long chain branched (LCB)

PVAc might be in order since long chain branching is known to have very high strain hardening behavior, as demonstrated for LDPE in Chapter 2. A simple, disadhesion mechanism like this is very valuable in that it would not require the use of exotic materials for implementation.

An investigation into the role of complex viscosity to bubble diameter in the HBSS control formula would help decide other directions of bimodal PVAc gum base development. Currently, bimodal PVAc gum prototypes have been constrained to the complex viscosity of the control gum formula. However, HBMax knowledgabley has a much lower complex viscosity, and thus chew viscosity, than the HBSS control but still get large bubble diameters. Therefore, a study of this effect is important to understand whether control bubble diameter fracture limitations can be controlled by decreasing the viscosity of the gum therefore delaying fracture mechanism initiation to large biaxial strains.

A study for the processing parameters required for optimal HMW gum base homogeneity is of interest because studies in this work suggest small HMW amounts compound more readily than the higher amounts required for high performance bubblegum production. Thus, a study of the processing parameters (i.e. temperature, time, shear rate, etc.) would be beneficial in determining optimum gum base homogeneity and therefore make product performance more robust.

One of the more interesting observations for this work was the discovery that talc has a positive effect on strain hardening and bubble diameter in a certain viscosity range. Additionally, since current prototypes appear to possibly have fracture limitations from talc's role in the gum base and its connection to gum base homogeneity is also of interest because it is still limited to qualitative scientific knowledge. One interesting study would be an investigation of talc's basal cleavage and its effect on bubble diameter. For instance, one possible mode of bubble fracture is

for talc basal cleavage resulting in localized plastic deformation and failure. This mechanism, if understood, could be prevented by changing talc's aspect ratio, surface modification, or overall equiaxed diameter to decrease cleavage likelihood.

Further investigation of the SIS/SI block copolymer blends with the addition of tackifying resin is of interest because such a system is analagous to its possible implementation in gum base and therefore would afford a better understanding of its effect. Additionally, while on the them of triblock/diblock copolymer blends, a blend system which is compatible to the types of plasticizers, like triacetin, use in gum base definitely deserves research. A tunable gum base would have a significant impact on the simplification of the multitude of gum bases that most gum company's still use in their products. Another study of interest for block copolymer blends is to change their triblock mid-block molecular architecture to optimize flow stabilization. For instance, a decreased bridging chain molecular weight would help increase strain hardening response while gum base formulations with double network block copolymer blends might help as well. One network could be designed to be weak and strain hardening just enough to stabilize initial plastic flow while the other could be made to be tougher to stabilize large strain biaxial flow.

Ultimately, the systems-approach has been demonstrated to be very effective for the design of bubblegum while balancing conflicting performance objectives. Thus, a broad range of material problems can be solved with this approach ranging from gum base biodegradability to biopolymer compatibility. The approach is grounded on scientific modeling of microstructural phenomena of the type that dominate biodegrability and biopolymer compatibility.

References

[1] National Association of Chewing Gum Manufacturers (NACGM). The Story of Gum. http://www.nacgm.org/consumer/storyof.html, August 2006.

[2] Michael Redclift. *Chewing Gum: An Unofficial History*, volume 19. Routledge, New York City, NY, 2004.

[3] Joachin Meissner. Rheometer for the study of mechanical properties of deformation of plastic melts under definite tensile stresses. *Rheologica Acta*, 8(1):78–88, 1969.

[4] H. Munstedt. New Universal Extensional Rheometer for Polymer Melts - Measurements on a Polystyrene Sample. *Journal of Rheology*, 23(4):421–436, 1979.

[5] Christopher W. Macosko. *Rheology: Principles, Measurements, and Applications*. Wiley-VCH, New York, 1994.

[6] C. D. Han and R. Shetty. Flow Instability in Tubular Film Blowing 1. Experimental-Study. *Industrial & Engineering Chemistry Fundamentals*, 16(1):49–56, 1977.

[7] C. D. Denson and R. J. Gallo. Measurements of the Biaxial Extension Viscosity of Bulk Polymers: The Inflation of a Thin Polymer Sheet. *Polymer Engineering and Science*, 11 (2):174–176, 1971.

[8] P. Hachmann and J. Meissner. Rheometer for equibiaxial and planar elongations of polymer melts. *Journal of Rheology*, 47(4):989–1010, 2003.

[9] S. Chatraei and Christopher W. Macosko. Lubricated Squeezing Flow: A New Biaxial Extensional Rheometer. *Journal of Rheology*, 25(4):433–443, 1981.

[10] November 7: Cadbury Debuts Trident in the UK, 2006.

[11] Global Bubblegum Sales, 2006.

[12] Cyril Stanley Smith. *A Search for Structure: Selected Essays on Science, Art, and History*. The MIT Press, Cambridge, 1981.

[13] H. Munstedt. Dependence of the Elongational Behavior of Polystyrene Melts on Molecular-Weight and Molecular-Weight Distribution. *Journal of Rheology*, 24(6):847–867, 1980.

[14] H. Munstedt and H. M. Laun. Elongational Properties and Molecular-Structure of Polyethylene Melts. *Rheologica Acta*, 20(3):211–221, 1981.

[15] B. Schlund and L. A. Utracki. Linear Low-Density Polyethylenes and Their Blends 3. Extensional Flow of LLDPEs. *Polymer Engineering and Science*, 27(5):380–386, 1987.

[16] J. L. White and H. Yamane. A Collaborative Study of the Stability of Extrusion, Melt Spinning and Tubular Film Extrusion of Some Highlow, Lowlow and Linear-Low Density Polyethylene Samples. *Pure and Applied Chemistry*, 59(2):193–216, 1987.

[17] L. Berger and J. Meissner. Linear Viscoelasticity, Simple and Planar Melt Extension of Linear Polybutadienes with Bimodal Molar Mass Distributions. *Rheologica Acta*, 31(1): 63–74, 1992.

[18] M. Takahashi, T. Isaki, T. Takigawa, and T. Masuda. Measurement of Biaxial and Uniaxial Extensional Flow Behavior of Polymer Melts at Constant Strain Rates. *Journal of Rheology*, 37(5):827–846, 1993.

[19] A. Minegishi, Y. Naka, T. Takahashi, Y. Masubuchi, J. Takimoto, and K. Koyama. The effect of ultrahigh molecular weight polymers on the nonlinear response in uniaxial elongational viscosity. *Nihon Reoroji Gakkaishi*, 25(4):215–216, 1997.

[20] G. J. Field, P. Micic, and S. N. Bhattacharya. Melt strength and film bubble instability of LLDPE/LDPE blends. *Polymer International*, 48(6):461–466, 1999.

[21] A. Minegishi, A. Nishioka, T. Takahashi, Y. Masubuchi, J. Takimoto, and K. Koyama. Uniaxial elongational viscosity of PS/a small amount of UHMW-PS blends. *Rheologica Acta*, 40(4):329–338, 2001.

[22] M. Sugimoto, Y. Masubuchi, J. Takimoto, and K. Koyama. Melt rheology of polypropylene containing small amounts of high molecular weight chain. I. Shear flow. *Journal of Polymer Science Part B-Polymer Physics*, 39(21):2692–2704, 2001.

[23] M. Sugimoto, Y. Masubuchi, J. Takimoto, and K. Koyama. Melt rheology of polypropylene containing small amounts of high-molecular-weight chain. 2. Uniaxial and biaxial extensional flow. *Macromolecules*, 34(17):6056–6063, 2001.

[24] H. Munstedt, T. Steffl, and A. Malmberg. Correlation between rheological behaviour in uniaxial elongation and film blowing properties of various polyethylenes. *Rheologica Acta*, 45(1):14–22, 2005.

[25] V. Leal, P. Lafuente, R. Alicante, R. Perez, and A. Santamaria. New results on the correlation molecular architecture-melt elasticity-blowing process-film properties for conventional and metallocene-catalyzed polyethylenes. *Macromolecular Materials and Engineering*, 291(6):670–676, 2006.

[26] S. Kurzbeck, F. Oster, and H. Munstedt. Rheological properties of two polypropylenes with different molecular structure. *Journal of Rheology*, 43(2):359–374, 1999.

[27] P. Micic, S. N. Bhattacharya, and G. Field. Transient elongational viscosity of LLDPE/LDPE blends and its relevance to bubble stability in the film blowing process. *Polymer Engineering and Science*, 38(10):1685–1693, 1998.

[28] P. Micic and S. N. Bhattacharya. Elongational behavior of polyethylene melts - Effect of deformation. *Polymer Engineering and Science*, 40(7):1571–1580, 2000.

[29] P. Micic and S. N. Bhattacharya. Rheology of LLDPE, LDPE and LLDPE/LDPE blends and its relevance to the film blowing process. *Polymer International*, 49(12):1580–1589, 2000.

[30] M. Sugimoto, T. Tanaka, Y. Masubuchi, J. Takimoto, and K. Koyama. Effect of chain structure on the melt rheology of modified polypropylene. *Journal of Applied Polymer Science*, 73(8):1493–1500, 1999.

[31] J. F. Le Meins, P. Moldenaers, and J. Mewis. Suspensions of monodisperse spheres in polymer melts: particle size effects in extensional flow. *Rheologica Acta*, 42(1-2):184–190, 2003.

[32] Gwilym M. Jenkins. *The Systems Approach*. Systems Behavior. Open University Press, 1972.

[33] Gregory B. Olson. Materials Design: An Undergraduate Course. In Peter K. Liaw, J. R. Weertman, Harris L. Marcus, and Joseph S. Santner, editors, *Morris E. Fine Symposium*, pages 41–48. The Minerals, Metals & Materials Society, 1991.

[34] Morris Cohen. Unknowables in the Essence of Materials Science and Engineering. *Materials Science and Engineering*, 25:3, 1976.

[35] Morris Cohen. Metallurgy and the Evolution of Materials Science and Engineering. In Gregory B. Olson, M. Azrin, and E.S. Wright, editors, *Sagamore Army Materials Research Conference Proceedings*, volume 34th of *Innovations in Ultrahigh-Strength Steel Technology*, page 67, 1987.

[36] Gregory B. Olson. Computational Design of Hierarchically Structured Materials. *Science*, 277:1237–1242, 1997.

[37] Raquel Maria D'Oyen. *Systems Design of Case Hardened Polymers for Gears*. PhD thesis, Northwestern University, 1997.

[38] S. Carr, R. D'Oyen, and G. Olson. Design of Thermoset Resins with Optimal Graded Structures. *Proceedings of the Fourth International Conference on Composites Engineering*, pages 205–206, 1997.

[39] Arup Saha. *Systems Design of Transformation Toughened Blast Resistant Naval Hull Steels*. Dissertation, Northwestern University, 2004.

[40] A. Saha and G. Olson. Computer-aided design of transformation toughened blast resistant naval hull steels: Part I. *Journal of Computer Aided Materials Design*, 14:177–200, 2007.

[41] A. Saha, J. Jung, and G. Olson. Prototype evaluation of transformation toughened blast resistant naval hull steels: Part II. *Journal of Computer Aided Materials Design*, 14:201–233, 2007.

[42] G. B. Olson and M. Azrin. Transformation Behavior of TRIP Steels. *Metallurgical Transactions A*, 9A:713–721, 1978.

[43] G. B. Olson. Overview: Science of Steel. *in Innovations in Ultrahigh-Strength Steel Technology, ed. G. B. Olson, M. Azrin, and E. S. Wright, Sagamore Army Materials Research Conference Proceedings*, 34th:3–66, 1990.

[44] Walter A. Backofen. *Deformation Processing*. Metallurgy and Materials. Addison-Wesley Publishing Company, Reading, 1972.

[45] C. Gabriel. Strain hardening of various polyolefins in uniaxial elongational flow. *Journal of Rheology*, 47(3):619–630, 2003.

[46] W. F. Hosford and R. M. Caddell. *Metal Forming: Mechanics and Metallurgy*. Cambridge University Press, Cambridge, 3rd edition, 2007.

[47] J. H. Hollomon and L. D. Jaffe. *Ferrous Metallurgical Design: Design Principles for Fully Hardened Steels*. J. Wiley and Sons, New York, first edition, 1947.

[48] N. L. Chin, P. J. Martin, and G. M. Campbell. Dough aeration and rheology: Part 3. Effect of the presence of gas bubbles in bread dough on measured bulk rheology and work input rate. *Journal of the Science of Food and Agriculture*, 85(13):2203–2212, 2005.

[49] O. Ishizuka and K. Koyama. Elongational Viscosity at a Constant Elongational Strain Rate of Polypropylene Melt. *Polymer*, 21(2):164–170, 1980.

[50] R. N. Haward. Strain-Hardening of Thermoplastics. *Macromolecules*, 26(22):5860–5869, 1993.

[51] Joel R. Fried. *Polymer Science and Technology*. Prentice Hall Professional Technical Reference, Upper Saddle River, second edition, 2003.

[52] P. G. de Gennes. Reptation of a Polymer Chain in the Presence of Fixed Obstacles. *Journal of Chemical Physics*, 55(2):572, 1971.

[53] J. Klein. Evidence for Reptation in an Entangled Polymer Melt. *Nature*, 271(5641): 143–145, 1978.

[54] G. C. Berry and T. G. Fox. The Viscosity of Polymers and their Concentrated Solutions. *Advances in Polymer Science*, 5:261, 1968.

[55] W. W. Graessley. The Entanglement Concept in Polymer Rheology. *Advances in Polymer Science*, 16:1, 1974.

[56] S. A. Khan, R. K. Prudhomme, and R. G. Larson. Comparison of the Rheology of Polymer Melts in Shear, and Biaxial and Uniaxial extensions. *Rheologica Acta*, 26(2):

144–151, 1987.

[57] H. Munstedt, S. Kurzbeck, and L. Egersdorfer. Influence of molecular structure on rheological properties of polyethylenes Part II. Elongational behavior. *Rheologica Acta*, 37 (1):21–29, 1998.

[58] H. H. Winter. A Collaborative Study on the Relation Between Film Blowing Performance and Rheological Properties of Two Low-Density and Two High-Density Polyethylene Samples. *Pure and Applied Chemistry*, 55(6):943–976, 1983.

[59] M. Kompani and David C. Venerus. Equibiaxial extensional flow of polymer melts via lubricated squeezing flow. I. Experimental analysis. *Rheologica Acta*, 39:444–451, 2000.

[60] H. M. Laun and H. Schuch. Transient Elongational Viscosities and Drawability of Polymer Melts. *Journal of Rheology*, 33(1):119–175, 1989.

[61] S. Bazhenov, J. X. Li, A. Hiltner, and E. Baer. Ductility of Filled Polymers. *Journal of Applied Polymer Science*, 52(2):243–254, 1994.

[62] J. X. Li, A. Hiltner, and E. Baer. Fractography and Failure Mechanisms of Particulate-Filled Thermoplastic Polyester. *Journal of Applied Polymer Science*, 52(2):269–283, 1994.

[63] J. X. Li, M. Silverstein, A. Hiltner, and E. Baer. The Ductile-to-Quasi-Brittle Transition of Particulate-Filled Thermoplastic Polyester. *Journal of Applied Polymer Science*, 52 (2):255–267, 1994.

[64] Stephen L. Rosen. *Fundamental Principles of Polymeric Materials*. SPE Monograph. John Wiley & Sons, Inc., New York, second edition, 1993.

[65] V. Kovacevic, M. Leskovac, and S. L. Blagojevic. Morphology and failure in nanocomposites. Part II: Surface investigation. *Journal of Adhesion Science and Technology*, 16

(14):1915–1929, 2002.

[66] V. Kovacevic, M. Leskovac, S. L. Blagojevic, and D. Vrsaljko. Complex adhesion effects of inorganic nanofillers vs microfillers in polymer composites. *Macromolecular Symposia*, 221:11–22, 2005.

[67] V. Kovacevic, S. Lucic, and M. Leskovac. Morphology and failure in nanocomposites. Part I: Structural and mechanical properties. *Journal of Adhesion Science and Technology*, 16(10):1343–1365, 2002.

[68] Y. Chan, J. L. White, and Y. Oyanagi. Fundamental Study of the Rheological Properties of Glass-Fiber-Reinforced Polyethylene and Polystyrene Melts. *Journal of Rheology*, 22 (5):507–524, 1978.

[69] T. Takahashi, J. I. Takimoto, and K. Koyama. Uniaxial elongational viscosity of various molten polymer composites. *Polymer Composites*, 20(3):357–366, 1999.

[70] V. Kovacevic, S. Lucic, D. Hace, and Z. Cerovecki. Tensile properties of calcium carbonate-reinforced poly(vinyl acetate). *Journal of Adhesion Science and Technology*, 10(12):1273–1285, 1996.

[71] V. Kovacevic, S. Lucic, D. Hace, and A. Glasnovic. Rheology and morphology of poly(vinyl acetate) plus calcite films. *Polymer Engineering and Science*, 36(8):1134–1139, 1996.

[72] V. Kovacevic, S. Lucic, and Z. Cerovecki. Influence of filler surface pre-treatment on the mechanical properties of composites. *International Journal of Adhesion and Adhesives*, 17(3):239–245, 1997.

[73] V. Pasanovic-Zujo, R. K. Gupta, and S. N. Bhattacharya. Effect of vinyl acetate content and silicate loading on EVA nanocomposites under shear and extensional flow. *Rheologica Acta*, 43(2):99–108, 2004.

[74] H. Tanaka and J. L. White. Experimental Investigations of Shear and Elongational Flow Properties of Polystyrene Melts Reinforced with Calcium-Carbonate, Titanium-Dioxide, and Carbon-Black. *Polymer Engineering and Science*, 20(14):949–956, 1980.

[75] Y. X. Zhou and P. K. Mallick. Effects of temperature and strain rate on the tensile behavior of unfilled and talc-filled polypropylene. Part I: Experiments. *Polymer Engineering and Science*, 42(12):2449–2460, 2002.

[76] Charles M. Hansen. *Hansen Solubility Parameters: A User's Handbook*. CRC Press, New York, 1999.

[77] J. Hildebrand and R. L. Scott. *The Solubility of Nonelectrolytes*. Reinhold, New York, 3rd edition, 1950.

[78] G. Delmas, D. Patterson, and T. Somcynsky. Thermodynamics of Polyisobutylene-n-Alkane Systems. *Journal of Polymer Science*, 57:79–98, 1962.

[79] J. Biros, L. Zeman, and D. Patterson. Prediction of Chi Parameter by the Solubility Parameter and Corresponding States Theories. *Macromolecules*, 4(1):30–35, 1971.

[80] R. F. Blanks and J. M. Prausnitz. Thermodynamics of Polymer Solubility in Polar and Nonpolar Systems. *Industrial & Engineering Chemistry Fundamentals*, 3(1):1–8, 1964.

[81] J. Brandrup, E. H. Immergut, and E. A. Grulke, editors. *Polymer Handbook*. John Wiley & Sons, Inc., New York, 4th edition, 1999.

[82] *Vinnapas® Solid Resins Product Overview*. Wacker Polymer Systems GmbH & Co. KG, 84489 Burghausen, Germany, 2008.

[83] A. Roos and C. Creton. Effect of the Presence of Diblock Copolymer on the Nonlinear Elastic and Viscoelastic Properties of Elastomeric Triblock Copolymers. *Macromolecules*, 38:7807–7818, 2005.

[84] A. L. Flory, D. A. Brass, and K. R. Shull. Deformation and Adhesive Contact of Elastomeric Membranes. *Journal of Polymer Science: Part B: Polymer Physics*, 45:3361–3374, 2007.

[85] L. R. G. Treloar. Strains in an inflated rubber sheet and the mechanism of bursting. *Transactions of the Institution of the Rubber Industry*, 19:201–212, 1944.

[86] B. J. Dobraszczyk. Development of a new dough inflation system to evaluate doughs. *Cereal Foods World*, 42:516–519, 1997.

[87] Y. Li, J. A. Nemes, and A. A. Derdouri. Membrane inflation of polymeric materials: Experiments and finite element simulations. *Polymer Engineering and Science*, 41(8): 1399–1412, 2001.

[88] N. Reuge, F. M. Schmidt, Y. Le Maoult, M. Rachik, and F. Abbe. Elastomer biaxial characterization using bubble inflation technique. I: Experimental investigations. *Polymer Engineering and Science*, 41(3):522–531, 2001.

[89] M. Rachik, F. Schmidt, N. Reuge, Y. Le Maoult, and F. Abbe. Elastomer biaxial characterization using bubble inflation technique. II: Numerical investigation of some constitutive models. *Polymer Engineering and Science*, 41(3):532–541, 2001.

[90] M. N. Charalambides, L. Wanigasooriya, and J. G. Williams. Biaxial deformation of dough using the bubble inflation technique. II. Numerical modelling. *Rheologica Acta*, 41(6):541–548, 2002.

[91] M. N. Charalambides, L. Wanigasooriya, J. G. Williams, and S. Chakrabarti. Biaxial deformation of dough using the bubble inflation technique. I. Experimental. *Rheologica Acta*, 41(6):532–540, 2002.

[92] P. A. O'Connell and G. B. McKenna. Rheological Measurements of the Thermoviscoelastic Response of Ultrathin Polymer Films. *Science*, 307:1760–1763, 2005.

[93] P. A. O'Connell and G. B. McKenna. Dramatic stiffening of ultrathin polymer films in the rubbery regime. *European Physical Journal E*, 20(2):143–150, 2006.

[94] G. W. H. Hohne, W. F. Hemminger, and H. J. Flammersheim. *Differential Scanning Calorimetry*. Springer, Berlin; New York, 2nd edition, 2003.

[95] Y. L. Fang, P. J. Carreau, and P. G. Lafleur. Rheological effects of polyethylenes in film blowing. *Polymer Engineering and Science*, 43(7):1391–1406, 2003.

[96] Y. L. Fang, P. J. Carreau, P. G. Lafleur, and S. Ymmel. Properties of mLLDPE/LDPE blends in film blowing. *Polymer Engineering and Science*, 45(3):343–353, 2005.

[97] J. J. Lu and H. J. Sue. Morphology and mechanical properties of blown films of a low-density polyethylene/linear low-density polyethylene blend. *Journal of Polymer Science Part B-Polymer Physics*, 40(6):507–518, 2002.

[98] J. C. Pirkle and R. D. Braatz. Dynamic modeling of blown-film extrusion. *Polymer Engineering and Science*, 43(2):398–418, 2003.

[99] J. M. G. Cowie. *Polymers: Chemistry and Physics of Modern Materials*. Nelson Thornes Ltd., United Kingdom, 2nd edition, 1991.

[100] P. C. Painter and M. M. Coleman. *Fundamentals of Polymer Science: An Introductory Text - Second Edition*. Technomic Publishing Co., Inc., Lancaster, PA, 1997.

[101] K. L. Williams. Bridging the Modulus Gap Between LLDPE and HDPE. *Journal of Plastic Film and Sheeting*, 17:321–331, 2001.

[102] Leonard Cribbs. High Molecular Weight Film Resins with Increased Stiffness. *Journal of Plastic Film and Sheeting*, 17(4):291–305, 2001.

[103] P. C. Shannon, R. Kumar, P. P. Shirodkar, F. D. Ehrman, M. B. Davis, K. W. Trapp, and D. Li. Polyethylene Films, 2006.

[104] Subraman R. Cherukuri. Gum base, chewing gum containing same and method, October 5 1982.

[105] Wayne J. Puglia, Gary S. Kehoe, and Warren Clark. Reduced-Shrink Bubble Gum, Mar. 15, 1984 1984.

[106] Subraman R. Cherukuri and Gul Mansukhani. Polyvinylacetate Bubble Gum Base Composition, Jan. 26, 1988 1986.

[107] N. Saunders and A. P. Miodownik. *(CALPHAD) Calculation of Phase Diagrams: A Comprehensive Guide*. Pergamon, New York City, NY, 1997.

[108] O. Redlich and A. T. Kister. Algebraic Representation of Thermodynamic Properties and the Classification of Solutions. *Industrial and Engineering Chemistry*, 40(2):345–348, 1948.

[109] Helen Whelton. *Saliva and Oral Health: An essential overview for the health professional*. Introduction: the anatomy and physiology of salivary glands. Dennis Barber Limited, London, UK, 3rd edition, 2004.

[110] Code of Federal Regulations - Title 21; Chapter I; Part 172; Section 172.615: Chewing Gum Base, 2006.

[111] M. Mooney. A Theory of Large Elastic Deformation. *Journal of Applied Physics*, 11(9): 582–592, 1940.

[112] R. S. Rivlin. Large Elastic Deformations of Isotropic Materials. IV. Further Developments of the General Theory. *Philosophical Transactions of the Royal Society of London, Series A*, 241(835):379–397, 1948.

[113] I. M. Ward and D. W. Hadley. *An Introduction to the Mechanical Properties of Solid Polymers*. Wiley, Chichester, UK, 1993.

[114] R. A. L. Jones and R. W. Richards. *Polymers at Surfaces and Interfaces*. Cambridge University Press, Cambridge, 1999.

[115] J. D. Ferry. *Viscoelastic Properties of Polymers*. Wiley, New York, 3rd edition, 1980.

[116] G. Holden, E. T. Bishop, and N. R. Legge. Thermoplastic elastomers. *Journal of Polymer Science, Part C: Polymer Symposia*, 26:37–57, 1969.

[117] Mike Greenberg. Personal communication, 2007. Past internal reports showed significantly less monomer than existed before base processing.

[118] A. E. Nesterov, Y. S. Lipatov, V. V. Horichko, and T. D. Ignatova. Effect of filler on kinetics and energy of activation of phase separation in poly(methyl methacrylate) poly(vinyl acetate) blend. *Macromolecular Chemistry and Physics*, 199(11):2609–2612, 1998.

[119] A. E. Nesterov, Y. S. Lipatov, and T. D. Ignatova. Effect of an interface with solid on the component distribution in separated phases of binary polymer mixtures. *European Polymer Journal*, 37(2):281–285, 2001.

[120] J. Stewart. *Calculus: Early Transcendentals*. Brooks/Cole Publishing Co., Pacific Grove, CA, 4th edition, 1999.

[121] M. Harrison and B. P. Hills. Effects of air flow-rate on flavour release from liquid emulsions in the mouth. *International Journal of Food Science and Technology*, 32:1–9, 1997.

[122] National Instruments. LabView, release 7.0. http://www.ni.com, 2004.

[123] Inc. Stat-Ease. DesignExpert, release 7.1.5. http://www.statease.com, 2008.

[124] N. Aubee, P. Lam, and S. Marshall. A New Family of sHDPE Polymers for Enhanced Moisture Barrier Performance. *Journal of Plastic Film and Sheeting*, 22:315–330, 2006.

[125] T. H. Kwalk. Polyethylene Blend Compositions, 2007.

[126] H. Higuchi, S. Fujikawa, M. Sato, and K. Koyama. Thickness Uniformity of HDPE Blown Film: Relation to Rheological Properties and Density. *Polymer Engineering and Science*, 44(5):965–972.

[127] C. H. Fisher. Solubility Parameters of Oil and Fat Chemicals. *Journal of American Oil Chemist's Society*, 78:215–216, 2001.

[128] C. M. Hansen. Polymer additives and solubility parameters. *Progress in Organic Coatings*, 51:109–112, 2004.

[129] W. Zeng, Y. Du, Y. Xue, and H. L. Frisch. *Physical Properties of Polymers: Chapter 16: Solubility Parameters*. Springer, New York, 2007.

APPENDIX A

Solubility Parameter Calculation

Table A.1 provides thermodynamic values for specific molecular group contributions. These group contributions are assembled in accordance with the chemical structure of a molecule to calculate its corresponding Hansen Solubility Parameters (HSP) via Equations 2.14-2.16. Calculated HSP values are shown in Table A.2 for the compounds whose $\chi_{1,2}$ parameters were calculated in Chapter 2. Experimental Hildebrand solubility parameters, δ, are calculated with 5% of their experimentally determined values using group contributions therefore suggesting the theoretical predictions to be sufficiently accurate for the prediction of gum base interactions.

Table A.1. Hansen Solubility Parameter Molecular Group Contributions

Structure Component	$Fd_i(J^{(1/2)}cm^{(3/2)}/mol)$	$Fp_i(J^{(1/2)}cm^{(3/2)}/mol)$	$Eh_i(J/mol)$
$-CH_3$	420	0	0
$=CH_2-$	270	0	0
$-CH-$	80	0	0
$-C-$	-70	0	0
$-O-$	100	400	3,000
$-C=0$	290	770	2,000
$-COO-$	390	490	7,000
$-COH$	470	800	4,500
$-OH$	210	500	20,000
$-benzene$	1,430	110	0
$-benzene(o,m,p)$	1,270	110	0

Table A.2. Comparison of calculated to experimental Hansen Solubility Parameters.

Gum Component	δ_d $(MPa)^{1/2}$	δ_p $(MPa)^{1/2}$	δ_h $(MPa)^{1/2}$	δ_{calc}	δ_{exp}^a
Vanillin	17.2	7.2	13.8	23.2	25.5
Ethyl Isobutyrate	14.8	3.6	7.2	16.9	16.7
Water	16.6	18.8	16.7	30.1	-
n-Butyl n-Butyrate	15.9	3.0	6.6	17.4	-
Benzyl Alcohol	18.5	2.5	13.9	23.3	23.8
Triacetin	16.2	0	8.9	18.5	21
PVAc	16.0	6.8	9.8	20.0	23.1
PIB	15.6	0	0	15.6	15.5

The references for these experimental values are [127–129].

APPENDIX B

Dynamic Moduli Comparison of Pure PVAcs Having Differing Molecular Weight Distributions

Dynamic shear moduli and complex viscosity master curves are shown in Figure B.1 A-C. The 50 kgmol PVAc examined in Figure B.1A shows an indistinctive G', G" crossover which is indicative of it having a broad / polydisperse molecular weight distribution. Polydispersity is shown to increase when blending 380 kg/mol PVAc into 50 kg/mol PVAc as depicted by the further smearing of the G', G" crossover region in Figure B.1B. Overall, a shift in the G', G" crossover (blue arrows) towards lower angular frequencies (ω) with increasing average molecular weight (A.) $\rightarrow$ C.)) is apparent. Such a shift is indicative of the appearance of an entanglement plateau (red arrows) at higher angular frequencies for higher molecular weight polymer systems like the one for 380 kg/mol PVAc shown in Figure B.1C. Increased entanglement in the shear regime, as evidenced by the shifting crossover and appearance of the plateau, is indirect evidence for similar increases in the extensional flow of such systems (presented in Chapter 4). Therefore, this data is presented as an indirect evidence in support of the proof-of-principle and performance objective achievements to flow behaviors demonstrated for the pure bimodal PVAc polymeric system. Additionally, this supports the idea that entanglements were designed into the biaxial extensional flow behavior of prototype gums and are the reason for improved bubble performance.
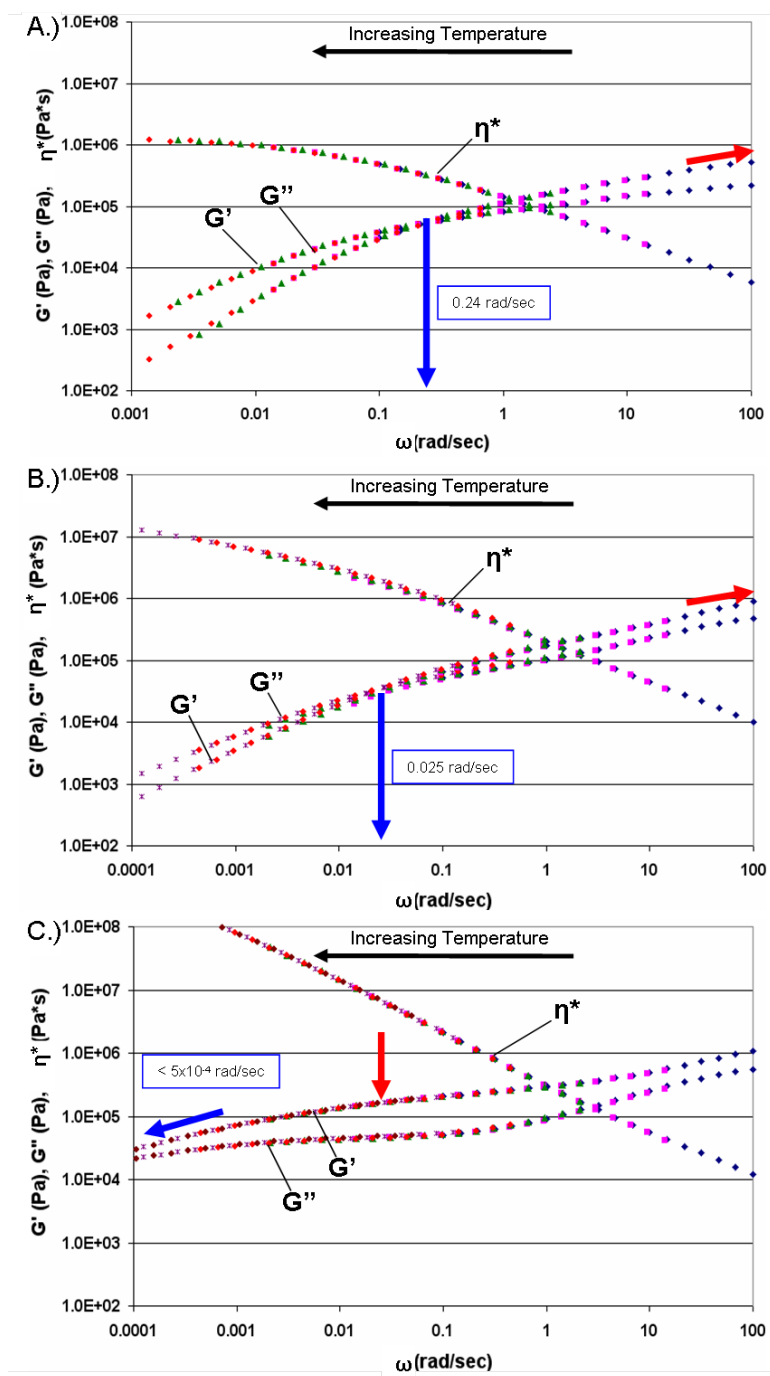
Figure B.1. Dynamic moduli master curves at a T_{ref} = 70 °C for pure PVAc having molecular weights of A.) 50 kg/mol, B.) 20/80 50/380 kg/mol blend, and C.) 380 kg/mol.

APPENDIX C

Poly(vinyl acetate - vinyl laurate) Chew Viscosity Model Parameters

Poly(vinyl acetate - vinyl laurate) (poly-(VAVL)) chew viscosity model parameters are outlined in this appendix. There utility was demonstrated in Chapter 5 in accordance with Redlich-Kister solution modeling of complex viscosity (Equations 5.2 - 5.7)). Model endpoints are shown in Table C.1 while interstitial and substitutional binary interaction parameters are displayed in Tables C.2 and C.3, respectively. These parameters were used for the constraint of the third generation poly-(VAVL) (P3-VAVL) prototype's chew viscosity as demonstrated in section 5.3.2. This prototype's extensional flow properties were studied in Chapter 6.

Table C.1. Endpoints ($\eta_{i,j}^{*o}$, Pa*sec) for Redlich-Kister solution modeling of complex viscosity.

PVAc MW (kg/mol)	j		
i	Tr	Ta	Va
50	-459	2,493	1856
VAVL	-7,926	1,588	591

Table C.2. Interstitial binary interaction parameters ($L_{i:j_1,j_2}^{v*}$, Pa*sec) for modeling complex viscosity with Redlich-Kister polynomials.

Binary Order $\rightarrow$	k = 0			k = 1		
$i \backslash j_1, j_2$	Ta,Tr	Va,Tr	Ta,Va	Ta,Tr	Va,Tr	Ta,Va
50	-5,468	1,198	-1,870	0	-10,384	3,814
VAVL	1,138	13,856	-1,260	2,484	-7,434	-1,545

Table C.3. Substitutional binary interaction parameters ($L^{v*}_{i_1,i_2:j}$), Pa*sec) for modeling complex viscosity with Redlich-Kister polynomials.

Binary Order →	k = 0			k = 1		
$i_1, i_2 \backslash j$	Tr	Ta	Va	Tr	Ta	Va
50 , VAVL	1,423	-7,158	-826	-554	0	0